

Design of Robotic Quadruped Legs

by

Jacob Elijah McKenzie

Submitted to the Department of Mechanical Engineering
in partial fulfillment of the requirements for the degree of

Master of Science

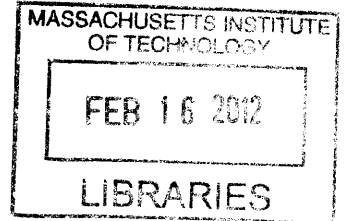
at the

MASSACHUSETTS INSTITUTE OF TECHNOLOGY

February 2012

© Massachusetts Institute of Technology 2012. All rights reserved.

ARCHIVES



Author
Department of Mechanical Engineering
January 20, 2012

Certified by
Sangbae Kim
Esther and Harold E. Edgerton Assistant Professor of Mechanical Engineering
Thesis Supervisor

Accepted by
David E. Hardt
Ralph E. and Eloise F. Cross Professor of Mechanical Engineering
Chairman, Department Committee on Graduate Theses

Design of Robotic Quadruped Legs

by

Jacob Elijah McKenzie

Submitted to the Department of Mechanical Engineering
on January 20, 2012, in partial fulfillment of the
requirements for the degree of
Master of Science

Abstract

Prized for their performance on prepared surfaces, wheeled vehicles are often limited in mobility by rough and unstructured terrain. Conversely, systems that rely on legs have shown promising rough terrain performance but only a modest ability to achieve high speeds over flat terrain. The goal of this thesis is to develop four robotic legs that are capable of robust dynamic running over flat terrain. Demonstration of this ability is necessary to improve the viability of robotic legs as a propulsion system. Achieving true dynamic running presents many challenges, and the first step in prevailing over the difficulties this task presents is the development of a sound mechanical system. The leg designs presented here are based on the development of four design principles from both biological systems, dynamic simulations and previous research. These principles suggest that a leg design should: minimize passive mechanical impedance, minimize mass and inertia, maximize actuator strength and develop a balance between leg kinematics and robot use. To bring these principles into reality several unique design features were introduced including a doubly concentric actuator layout, synthetic fiber tendons to reduce bending loads in the legs, polymer leg links and the use of electric motors to their thermal limit. To accompany these technical features simulation-based design tools were developed that provide an intuitive insight into how altering design parameters of the leg may affect locomotion performance. The key feature of these tools is that they plot the forces that the leg is capable of imparting on the body for a given set of dynamic conditions. Single and multiple leg testing has shown that the legs perform well under dynamic loading and that they are capable producing vertical ground reaction forces larger than 800 N and horizontal forces larger than 150 N. Many of the design principles, features and tools developed may be used with a large variety of leg structures and actuation systems.

Thesis Supervisor: Sangbae Kim

Title: Esther and Harold E. Edgerton Assistant Professor of Mechanical Engineering

Acknowledgments

This research is supported by the Defense Advanced Research Projects Agency (DARPA) as part of the Maximum Mobility and Manipulation (M3) project. I would like to acknowledge the members of the Biomimetic Robotics Lab, and thank them for their support.

FOR ENJOY

Contents

1	Introduction	15
1.1	Motivation	15
1.2	Background: Running in Biology	18
1.2.1	Gaits	19
1.2.2	Leg Structure	22
1.2.3	Leg Dynamics	25
1.2.4	Force Generation	27
1.3	Background: Dynamic Performance	30
2	Design Principles	31
2.1	Operational Phases	31
2.1.1	Impact	33
2.1.2	Stance	35
2.1.3	Swing	39
2.2	Performance Limits	41
2.3	Design Criteria	44
3	Leg Design	47
3.1	Design Space	47
3.2	Conceptual Framework	48
3.3	Detailed Design	56
3.3.1	Front Leg	57
3.3.2	Rear Leg	67

4	Modeling and Performance Estimation	71
4.1	Actuator Modeling	71
4.2	Single Leg Dynamics	74
4.2.1	Mathematical Model	74
4.2.2	Stance Phase Simulation	82
4.2.3	Protraction	87
5	Design Tools	91
5.1	Assessing Leg Capability with Force Maps	91
5.2	Force Map Stride Planning	95
5.2.1	Selecting a Stride Primitive	97
5.2.2	Calculating the Force Production Envelope	98
5.2.3	Selecting Touchdown Configuration	101
5.2.4	Calculating Torque Profiles	102
6	Testing and Design Iteration	105
6.1	Design Proof	105
6.2	Single Leg Testing	106
6.3	Multi Leg Testing	107
7	Summary/Conclusions	109
7.1	Design considerations	109
7.2	Unique Features	110
7.3	Design tools	111
A	Engineering Drawings	113
B	Matlab Code Listing	137

List of Figures

1-1	Conceptual model of quadrupedal robot	16
1-2	Workspace of wheel versus leg	18
1-3	Support phase diagrams for biped gaits	19
1-4	Footfall event diagrams for biped gaits	19
1-5	Definitions of stride related variables	20
1-6	Common quadrupedal gaits	21
1-7	Support phase diagram of the rotary gallop	21
1-8	Support phase diagram of the transverse gallop	22
1-9	The plantigrade, digitigrade, and unguligrade legs	23
1-10	Skeletal structure of the wolf	24
1-11	Position of the shoulder throughout a stride	26
1-12	Ground reaction forces of a galloping dog	28
2-1	Decoupling of body reaction forces	33
2-2	Model of leg extension and compression during impact	35
2-3	Series compliance method of reducing impact impedance	35
2-4	Two dimensional, one legged hopping model	37
2-5	Effect of horizontal disturbance force (F_{dbx}) on one leg hopper	39
2-6	Effect of vertical disturbance force (F_{dby}) on one leg hopper	39
2-7	Effect of mass disturbance (m_d) on one leg hopper	40
2-8	Effect of horizontal velocity disturbance (\dot{x}_d) on one leg hopper	40
3-1	Prismatic, articulated, and redundantly articulated topologies	49
3-2	Motion of the prismatic leg	49

3-3	Motion of the articulated leg	51
3-4	Configuration gearing of the elbow	51
3-5	Motion of the redundantly articulated leg	52
3-6	Configuration possibilities with redundant leg	52
3-7	Selected leg topology	53
3-8	Simple leg design, shoulder high inertia	55
3-9	Doubly concentric leg design, low shoulder inertia	55
3-10	Link bending load during stance	56
3-11	Bending loads are reduced by a static tendon	56
3-12	Front leg, front view	57
3-13	Front leg, rear view	57
3-14	Allied Motion HT05001 motor	60
3-15	Shoulder unit of front leg (front view)	61
3-16	Shoulder unit of front leg (rear view)	61
3-17	Shoulder actuation	62
3-18	Elbow actuation	62
3-19	Schematic representation of gearbox	63
3-20	Gear weight reduction	63
3-21	Planet carrier and planets assembled	64
3-22	Closeup photo of the assembled gearbox	64
3-23	Bearing placement in front leg	65
3-24	Ad/abduction mount on the shoulder unit	65
3-25	Assembled front leg links	66
3-26	Foam composite leg	66
3-27	Front leg Kevlar tendon	66
3-28	Rear leg, front view	67
3-29	Rear leg, rear view	67
3-30	Gear reduction of the hip motor	69
3-31	Motion of the knee motor	69
3-32	Bearing placement in the rear leg	69

4-1	Anticipated motor current in a fast gallop	72
4-2	Winding temperature under 300 W load	73
4-3	Thermal model of motor	73
4-4	Kinematics of a two link serial chain	75
4-5	Revolute and prismatic joints in screw theory	76
4-6	n -link kinematic chain	77
4-7	Definition of geometry for two link serial chain	82
4-8	Stance phase program layout	83
4-9	Accessible body forces in a specific configuration	83
4-10	Available body forces at $y = 35$ cm	85
4-11	Available body forces at $y = 40$ cm	85
4-12	Available body forces at $y = 45$ cm	85
4-13	Available body forces at $y = 50$ cm	85
4-14	Available body forces at $v_x = 2$ m \cdot s ⁻¹	86
4-15	Available body forces at $v_x = 5$ m \cdot s ⁻¹	86
4-16	Available body forces at $v_x = 10$ m \cdot s ⁻¹	86
4-17	Available body forces at $v_x = 15$ m \cdot s ⁻¹	86
4-18	Three link leg for protraction analysis	87
4-19	Protraction optimization results for shoulder torque	88
4-20	Protraction optimization results for knee torque	88
4-21	Leg motion during protraction	89
5-1	Approximate hip (dashed) and shoulder (solid) trajectories for a running cheetah	93
5-2	Workspace of the front leg with fixed foot	94
5-3	Force production envelope for $\dot{x} = 2$ m \cdot s ⁻¹	94
5-4	Weighted force production envelope for $\dot{x} = 2$ m \cdot s ⁻¹	95
5-5	Acceptable touchdown configurations	96
5-6	Acceptable touchdown configurations as a function of speed	96
5-7	Straight versus curved shoulder profile	98

5-8	State dependent force envelope	99
5-9	The bounds of the SDFE	99
6-1	Single leg testing slide	106
6-2	Video of single leg testing	107
6-3	Single leg test data	107
6-4	Jumping of four legged robot	108

List of Tables

3.1	Weight budget for quadruped robot	48
3.2	Front leg design specifications	57
3.3	Motor parameters for custom wound HT05001	60
3.4	Rear leg design specifications	67
4.1	Leg parameters used in dynamic model	84

Chapter 1

Introduction

The research presented in this thesis documents the development of the front and rear legs of a quadrupedal robot designed for high speed, dynamic locomotion (cf. Figure 1-1). Target speeds over nominally flat natural terrain are $50 \text{ km} \cdot \text{h}^{-1}$ by 2014. Attaining such speeds requires substantial research in the areas of mechanical design, actuation systems, control theory and manufacturing. The work presented within addresses these four areas and suggests a unique, low mechanical impedance, leg design. The structure of the leg is based on four design principles developed from analysis of biological systems and dynamic modeling. A detailed design, covering the topics of leg geometry, actuator selection and component level design, is presented alongside the development of simulation design tools, intended to quantify the effects of design modifications in a manner that provides insight into the performance of the locomotive system.

1.1 Motivation

Wheeled vehicles provide many practical advantages, and over time a highly refined set of design tools and processes have been developed to aid their implementation. However, one disadvantage inherent to the wheel itself, its inability to cope with uneven terrain, severely limits the reach of all wheeled platforms [64]. To avoid this disadvantage the terrain is often engineered, cleared of obstacles and surfaced, giving it a structure that complements the wheel's strengths. Unfortunately, nature and the human environment rarely exhibit this



Figure 1-1: Conceptual model of quadrupedal robot showing four legs, compliant spine and tail.

type of structural uniformity, limiting the reach of vehicles of a given size to a small portion of their surroundings. Increasing the mobility of robotic platforms requires a new approach, a fundamental change in the way the ground is used to generate locomotive forces. The option explored in this thesis is the use of four robotic legs. This research is part of the Maximum Mobility and Manipulation (M3) program initiated by the Defense Advanced Research Projects Agency (DARPA).

Several features of wheeled vehicles have led to their widespread adoption. First and foremost among these is the simplicity of their fundamental structure. A four wheeled vehicle of sound construction is statically stable and is thus capable of supporting itself and remaining stationary on level ground. If a driving torque is applied to a laterally opposed pair of wheels the resulting motions can be simply expressed, particularly at low speeds under quasi-static conditions [52]. Under more extreme conditions the equations of vehicle dynamics grow in complexity, however, a range of dynamic models of varying fidelity allow the designer to select a model that suits the demands of the application. Another admirable pair of features are the exceptionally high locomotive efficiencies possible on prepared surfaces and the excellent maneuverability that is possible with careful design. Advances in tire construction, suspension systems and aerodynamics allow some vehicles to maneuver with lateral accelerations larger than three times the acceleration of gravity [11].

A key characteristic of the environments that are prepared for wheeled vehicles is that no abrupt terrain irregularities approach the wheel diameter [64]. If such an obstacle is

encountered the vehicle must be directed along an alternative route. This decision is likely to increase the total transit time from origin to destination, or in the worst case, the inability of the vehicle to traverse the obstacle may make the destination unreachable.

Increasing the mobility of wheeled platforms over unstructured terrain can be approached in two ways: increasing wheel size or increasing the capacity of the wheel to deflect from its nominal position, such a change is said to increase the *workspace* of the wheel. The first option, enlarging the wheel, necessitates the proportional enlargement of the wheel well in order to accommodate the largest anticipated wheel displacement. This may substantially, and perhaps unacceptably, increase the overall size and mass of the vehicle, detracting from its performance in other areas. The alternative approach, increasing the workspace of the wheel, increases the ability of the system to handle terrain irregularities to as much as three wheel diameters [56]. However, this ability often comes at the expense of increasing kinematic complexity and reducing dynamic performance.

With a legged system a step change in height is approached in a fundamentally different way. The restrictions that a continuous path of contact imposes are removed, and therefore the point of contact is no longer required to climb the side of a step change in height. Consequently the foot may be made small, resulting in an increase in the available workspace (cf. Figure 1-2). Thus for a given external dimension the legged system tends to exhibit a superior ability to maneuver on stepped terrain. To illustrate this difference, suppose that an objective lies on the far side of a fallen square column that is 75 cm high. Most humans could simply step on to and then off of the column with relative ease, making the most of the large workspace our legs provide. However, even the most capable off-road vehicles would have difficulty traversing this obstacle and reaching the objective. In the human environment this type of terrain irregularity is exceedingly common.

The large workspace of legs can also be used to limit, or eliminate, steady state orientation errors of the body. This is generally not possible with wheeled vehicles that implement passive suspensions. Furthermore, because foot placement locations may be selected discretely during the traversal of uneven terrain, locations may be chosen to minimize the pitch, roll and height dynamics of the body. This foot placement approach reduces the apparent ruggedness of the terrain.

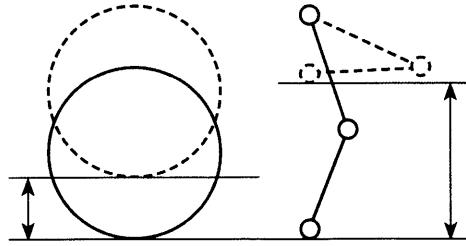


Figure 1-2: The workspace of a wheeled system and legged system of similar size are shown in a nominal configuration (solid lines) and in a maximally deflected vertical position (dashed lines).

The capability of legged systems to traverse rough terrain is continually being advanced by researchers [50]. However, before a legged robot can become a truly viable alternative to a wheeled system, it must demonstrate comparable ability on relatively flat, structured terrain as well. This is the focus of the present research. Once speed on level terrain has been improved, the origin to destination transit time over mixed terrain may begin to favor legged systems. Demonstration of this ability, and the development of the design methods and tools that enable it, are intended to prompt wider adoption and improve the mobility of robotic platforms.

1.2 Background: Running in Biology

Mixed, unstructured, terrain is abundant in the natural world, and one need look no further than the animals that occupy it to witness the potential capabilities of legged systems to perform admirably across its many terrain types. High speed locomotion across relatively even terrain typically occurs in the form of running. The precise definition of running is somewhat nebulous, however it is typically defined as the locomotion pattern of a legged system that contains an aerial phase, during which none of the limbs are in contact with the ground for some (generally short) period of time [6]. Many footfall patterns or *gaits* can be found in nature that align with this definition. However, the operational range of many legged robots confines them to gaits with quasi-static stability conditions, precluding the execution of true running gaits. Moving legged robots into the realm of dynamic running requires the development of a thorough understanding of the measures required to maintain robustness, maneuverability and speed.

1.2.1 Gaits

A gait is a particular temporal sequence of foot contact events that are repeated during the steady locomotion of a legged system. Walking, running and hopping are all examples of bipedal gaits (cf. Figure 1-3 and 1-4). In a human walking gait, support is transferred from the right to the left foot with a short period of double stance, during this time both feet are in contact with the ground [2]. For a running gait however, this overlap does not exist; instead a period of flight, commonly referred to as the aerial phase, takes its place. During hopping, the contact events of both feet fully overlap, followed by an aerial phase. The use of a particular gait has far reaching implications on the contact forces and the dynamics of the body and legs [42], and it is common for a variety of gaits to be used over the speed range of a given species.

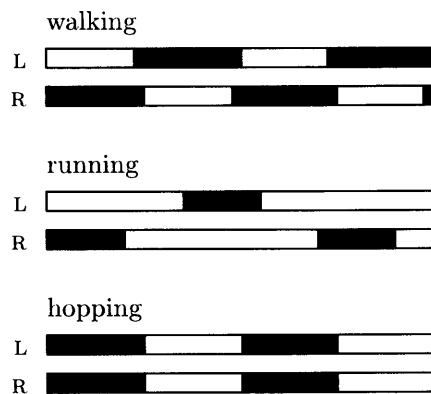


Figure 1-3: Support phase diagrams for three biped gaits. Shaded areas indicate when each foot is in contact with the ground as time progresses from left to right.

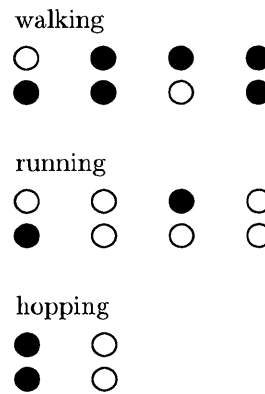


Figure 1-4: Footfall event diagrams for three biped gaits. Shaded circles indicate that a foot is in contact with the ground. When a contact or liftoff event occurs a new pair of circles are plotted to the right until the sequence repeats.

A *stride* is the shortest repeating footfall pattern, a single execution of a gait. The stride is repeated with a *stride frequency*, f (cf. Figure 1-5). The *stride length*, λ , is the distance covered in a single stride and thus the average forward velocity may be expressed as $\dot{x} = \lambda f$. The duty factor for a single leg, β , can be defined as the ratio of the leg's contact duration to the total stride duration, $1/f$. The combined duty factor, B , is the ratio of time during which any leg is in contact to the stride duration.

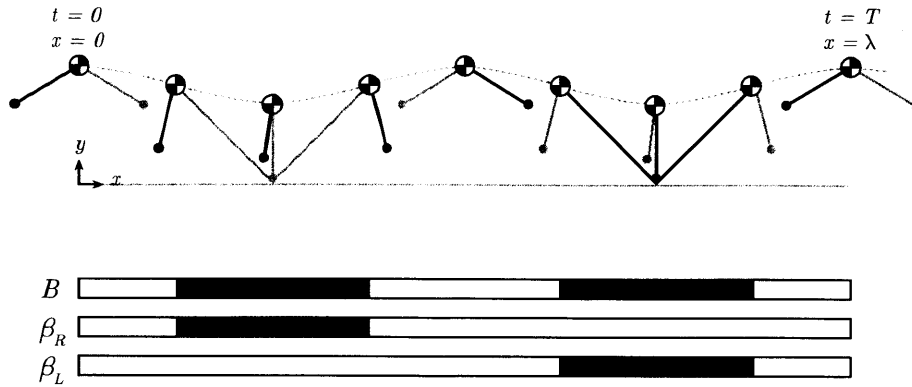


Figure 1-5: Definition of stride related variables using a two legged model with a point mass body.

In nature, quadrupeds exhibit many different types of gaits (cf. Figure 1-6) [1]. Two ubiquitous high speed gaits are the transverse and rotary gallops. The rotary gallop is exceedingly common in digitigrade carnivores such as cats and dogs. This type of gallop is characterized by a footfall pattern in which the next limb to make contact is the closest limb in either a clockwise or a counter clockwise direction (cf. Figure 1-6 and 1-7). This is to say that if the front right foot is in contact and the animal is using a clockwise rotary gallop the next foot to touch down will be the rear right. Between each footfall is an aerial phase. The aerial phase is generally short or nonexistent between laterally opposed limbs and may be very long between the front and rear limb pairs, depending on speed and species. The rotary gallop is used by both greyhounds and cheetahs at their maximum speeds [18].

The rotary gallop executed by cheetahs has several unique characteristics at maximum speed (close to $100 \text{ km} \cdot \text{h}^{-1}$) [55]. First, the combined duty factor, B , is very small, and because there are no concurrent contact events, $B = \sum \beta$. Second, the stride length is very long ($\lambda \doteq 7 \text{ m}$) and the stride frequency is quite fast ($f \doteq 2.6 \text{ Hz}$) at $72 \text{ km} \cdot \text{h}^{-1}$ [18]. In comparison, a horse, which has much longer legs, completes strides of lesser length at a slower rate.

One major difference between the manner in which cheetahs and horses run is that horses employ a different gait. The transverse gallop of a horse is used to achieve speeds close to $60 \text{ km} \cdot \text{h}^{-1}$ [55]. For an animal that is approximately nine times heavier than a

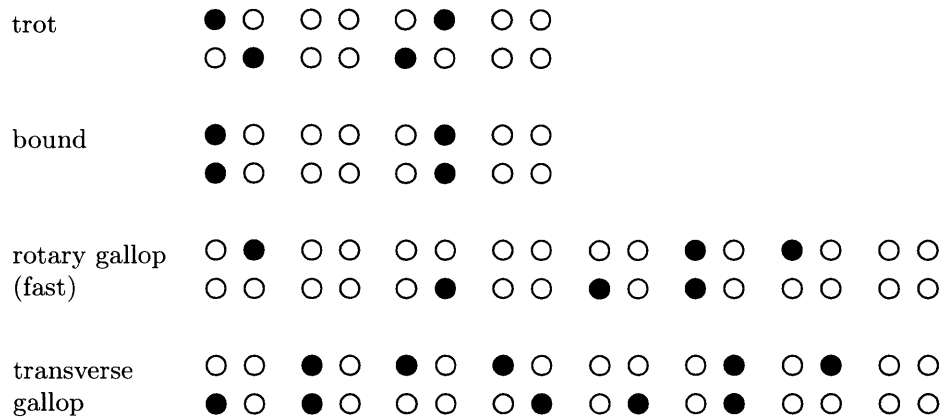


Figure 1-6: Four common quadrupedal gaits are the trot, bound, rotary gallop and transverse gallop, here they are shown using footfall phasing diagrams. Each group of four dots represents one contact state.

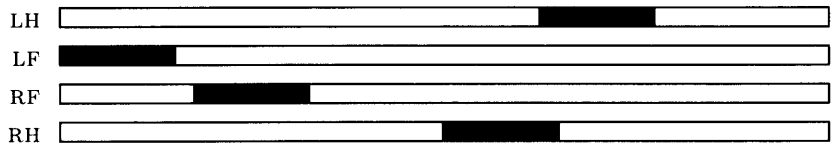


Figure 1-7: Support phase diagram for the rotary gallop of the cheetah based on data from [18].

cheetah this is quite a substantial speed. The transverse gallop may be either right or left leading (cf. Figure 1-8). It is worth noting that horses also differ substantially in leg structure from cats and dogs, which is a topic that will be discussed shortly [63].

In selecting a target gait for a legged robot, consideration must be given to the quantity and quality of available data and to the applicability of the gait to the desired locomotion task. For the task of running quickly the rotary gallop is somewhat common in nature but this does not imply that it will be the most effective gait when implemented with a robotic platform. The principles of legged locomotion, together with the principles of specific gaits, must be combined to drive the design and development of the system as a whole. The leg design and truly the entire robot design must be balanced enough to perform under maximum speed running conditions as well as the conditions of other gaits that may be used throughout the speed range.

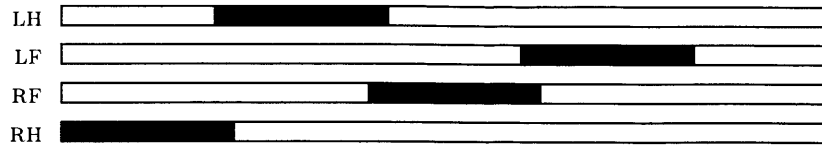


Figure 1-8: Support phase diagram for the transverse gallop of the horse based on data from [18].

1.2.2 Leg Structure

Leg musculoskeletal structure varies widely in both geometry and kinematics throughout the animal kingdom, and when combined with a compatible gait these two elements form the principle mechanism of legged locomotion. Leg structure and maximum speed have been shown to correlate with total animal mass, leg structure and many other factors [36]. And although the precise interaction between load bearing skeletal members is often complex, joint behavior can be approximated by the substitution of revolute and spherical kinematic joints under most circumstances [67]. This simplification is essential to the development of legged robots.

Three classes of leg structure are common throughout the natural world, they are: *plantigrade*, *digitigrade* and *unguligrade* (cf. Figure 1-9). These structures differ in the elements used to support the body during ground contact. The most familiar of these structures is plantigrade, the class used by humans. In a plantigrade leg the tarsals, at the heel of the foot, lie flat on the ground when standing. Proceeding proximally, the tarsals join the tibia and fibula of the lower leg followed by the femur of the upper leg. Distally, the tarsals join the metatarsals of the mid-foot, followed by the phalanges, the small bones of the toes.

A digitigrade leg structure is one in which the digits (toes) are used as the primary support structure for ground contact. This structure is common among fast and nimble hunters such as dogs and wolves, cats, birds and dinosaurs. In comparison to the plantigrade structure of humans, the foot (composed of the tarsals, metatarsals and phalanges) is much longer, and the weight during standing is borne by the equivalent of the human forefoot. The unguligrade structure takes this a degree further, bearing the full weight on the tips of the toes, which are often hoofed to support this immense load.

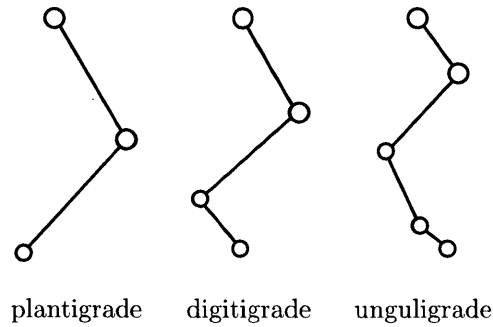


Figure 1-9: Plantigrade, digitigrade and unguligrade hind legs shown omitting members of the skeletal system that are in contact with the ground while standing.

By examining the leg structure of the wolf in detail, some of the key structural features of the digitigrade leg become clear (cf. Figure 1-10). Starting at the pelvis, which is connected to the femur and continuing to the more distal bones of the rear leg. The tibia and fibula meet the femur at the knee, the tibia being the largest of the two. At the human equivalent of the ankle the tibia and fibula meet the tarsals. The substantial protrusion to the rear of the foot is the calcaneum, a tendon attachment point that plays a central role in muscle gearing [48]. Continuing distally, the majority of the foot length is covered by the metatarsals. These long and narrow bones each connect to one of the phalanges. At the end of each toe is a claw. Cheetah claws, unlike those of most cats, are not retractable, with the exception of the first digital claw of the front paws.

The rear leg is somewhat different than the front when they are compared directly. The first obvious difference is the inversion of the upper limb structure. Specifically, the knee and elbow articulate in opposite directions. It has been postulated that this arrangement enhances the pitch stability of the body when compared to the three other possible configurations [32]. Again starting at the body of the wolf the first skeletal element of interest is the scapula. This large, flat bone is an attachment point for many muscles in the upper limb and provides some freedom of positioning and orienting the shoulder joint. The first bone of the front leg is the humerus, which connects to the radius and ulna at the elbow. Interestingly, the radius and ulna are far more comparable in size than the tibia and fibula. Both of these bones are connected to the carpals in the upper foot. Metacarpals make up the majority of the foot's length, and finally the phalanges and claws constitute the contacting elements of the foot.

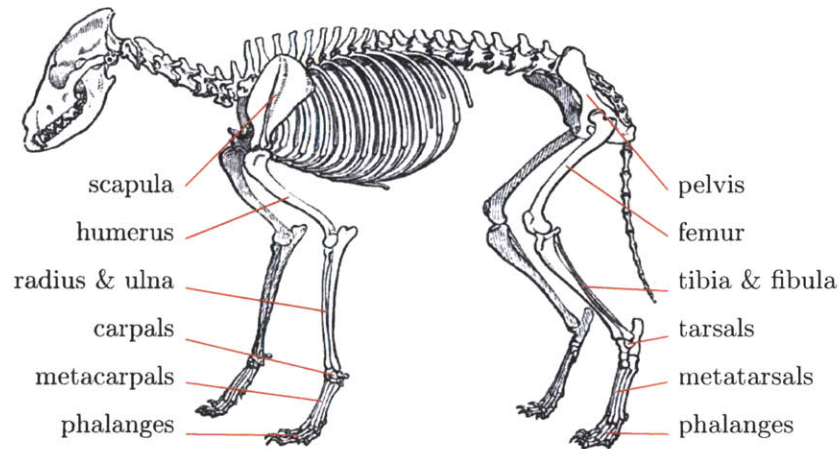


Figure 1-10: Labeled skeletal structure of the wolf showing the characteristics of front and rear digitigrade legs, adapted from [37].

The muscular system of the cheetah is of indisputable importance to the cheetah's impressive running speed. A cursory examination of feline species reveals relatively few fundamental skeletal differences, but the lean muscular build of the cheetah makes its appearance unique. Muscles, as with any actuator, perform best when they are implemented in a way that complements their strengths and minimizes their flaws. The muscle composition of cheetahs tends to favor fast twitch muscle fibers [66] and the connections between the muscle fibers and bone are located to meet the demands of both speed and force [48]. For example, the placement of the teres major, which links the scapula to the humerus and is active during stance, connects to the humerus at a location substantially further from the shoulder than in the greyhound [22]. This *muscle gearing* increases the mechanical advantage of the muscle about the shoulder and decreases the maximum joint rotational velocity, due to the fundamental limits of muscle contraction velocity [47]. In addition to muscle geometry the use of tendons to transmit motive forces produced by proximal muscles to distal joints represents an admirable structural strategy. This approach reduces the amount of muscle mass located far from the body, thus minimizing the leg inertia that would accompany such a mass distribution.

The structure of the foot, as the sole medium through which all locomotive forces are exerted, also plays a vital role in leg function. The majority of the load bearing of digitigrade feet is accomplished by the plantar. This soft fibrous tissue has highly nonlinear vertical stiff-

ness, high shear stiffness and exhibits a substantial amount of damping [10]. The location of the plantar is just aft and below the interface between the phalanges and the metacarpals or metatarsals. This implies that under standing conditions, a moment is produced about the phalange-metacarpus (or phalange-metatarsus) joint that forces the phalange tips and claws into the ground.

In addition to the joints of the legs, the spine also plays a substantial role in locomotion [4, 18]. Flexion of the spine allows the rear limbs to contact the ground ahead of the position in which they would land with a fixed length body. This appreciably lengthens the stride and increases the overall contact duration of the legs. The spine may also aid pitch correction and enhance the force generating capabilities of the legs by functioning as an additional redundant joint with very powerful actuation.

1.2.3 Leg Dynamics

The dynamics of quadruped legs have been studied by many biologists [57] and roboticists [53, 49]. Several key features of the rotary gallop and its implementation by digitigrade quadrupeds can be understood by close examination of the joint angle trajectories. Joint angles are typically measured by placing reflective markers on the surface of the skin at the approximate location of underlying joint. By recording the locations of these markers with high-speed photography, the approximate joint angles can be extracted with minimal obstruction of the natural gait [9].

Joint angle trajectories have a period of $1/f$, the stride duration, and are repeated during steady locomotion. In high speed gaits such as the rotary gallop the single leg duty factor is low ($\beta < 1/4$); this implies that the limb is not touching the ground for the vast majority of the stride. The contact interaction of each leg lasts for only β/f seconds. In this time the body travels forward approximately $\lambda\beta$ meters while the foot remains stationary on the ground. The changes in leg configuration that support this relative motion are captured in the joint angle trajectories.

During the steady rotary gallop of a dog, at the instant the leading front foot contacts the ground the limb is extended in a forward position, knee slightly bent and foot fully extended. Upon contact the foot angle, then the knee angle close, and the shoulder begins

to move forward over the foot. Near mid stance (when the shoulder is directly above the foot) the knee reaches its maximal flexion. As the stride progresses the knee extends to maintain ground contact and to provide propulsive forces. Continuing the stride, the knee begins to approach its maximum extension; flexion of the ankle also reaches a maximum, and as the load is reduced on the foot the ankle angle opens rapidly.

The shoulder position over the course of the stance phase typically follows a U shaped, relatively level, trajectory while each foot is in contact with the ground (cf. Figure 1-11) [18]. A profile of this type is common in most legged systems during running gaits, including those of humans [44]. A typical approach used to model this type of response is the spring loaded inverted pendulum (SLIP) model, in which a point mass rests atop a massless springy leg [41].

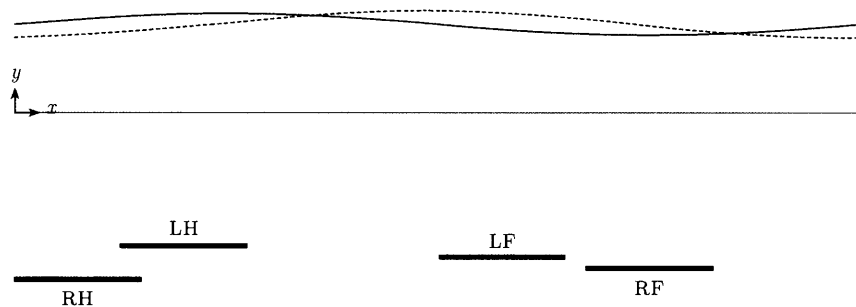


Figure 1-11: The position of the shoulder (solid) and hip (dashed) throughout a single stride of the cheetah executing a rotary gallop. Trajectories are drawn to scale above the ground at $y = 0$ based on data from [18].

After a limb has completed the ground contact phase it must be repositioned to prepare for the next ground contact at a distance λ from the present foot location. The forward movement of a limb (*protraction*) is often followed by a short dwell time and a rearward movement of the foot, just prior to ground contact (*retraction*). The joint angle trajectories during protraction show that it is common for the leg to be collapsed prior to rotation of the hip or shoulder [9]. This decreases the inertia of the leg and allows the entire protraction event to be completed more quickly. The degree of collapse depends on the relative masses and inertias of the leg links, and generally differs from species to species and animal to animal [14]. Dynamic simulations, presented in later chapters, show that the aggressive forward

swing of the leg may be stopped with relatively little effort on the part of the actuators by allowing the natural dynamics of the limb to extend the elbow, and thereby increase the inertia and slow the shoulder.

Because the limbs of many animals cannot be considered massless in comparison to the body one must also consider the forces and torques produced by protraction and retraction and their influence on the dynamics of the body. Clearly, unless the limb is extremely massive (as it is in an elephant for example) these forces will be small in comparison to the forces encountered during stance. Nonetheless, a well timed protraction may serve to neutralize any pitch disturbances before they cause large changes in pitch angle.

1.2.4 Force Generation

During the support phase of a gallop, forces generated between the foot and ground are transmitted to the body by the limb (cf. Figure 1-12). The contact event begins with a decelerating impact that generates forces opposing both the vertical (falling) and horizontal (running) velocity of the body [62]. After this impact has settled, and the leg has reached a suitable configuration, the limb begins to provide propulsive forces, typically near mid-stance, where the shoulder is directly above the foot. This propulsive force must be of sufficient magnitude to overcome the deceleration imparted by the earlier impact and any drag forces in order to maintain steady state. Additionally, the vertical forces must provide sufficient impulse to counteract the pull of gravity over the entire stride. As the shoulder continues to move forward both normal and propulsive forces decrease smoothly, with the final propulsive effort being exerted by rotation onto the phalanges and extension of the foot.

Formulation of the required locomotive forces in an impulse framework provides some insight into the scaling of contact loads with varying stride parameters. Over the entire stride, gravity imparts a downward pull with a total impulse of $-mg/f$, where m is the total mass, g is the gravitational acceleration and f is the stride frequency. This impulse must be balanced by the vertical contact forces, which are exerted over B/f seconds. This implies that the average contact force is

$$\bar{F}_y = \frac{mg}{B}. \quad (1.1)$$

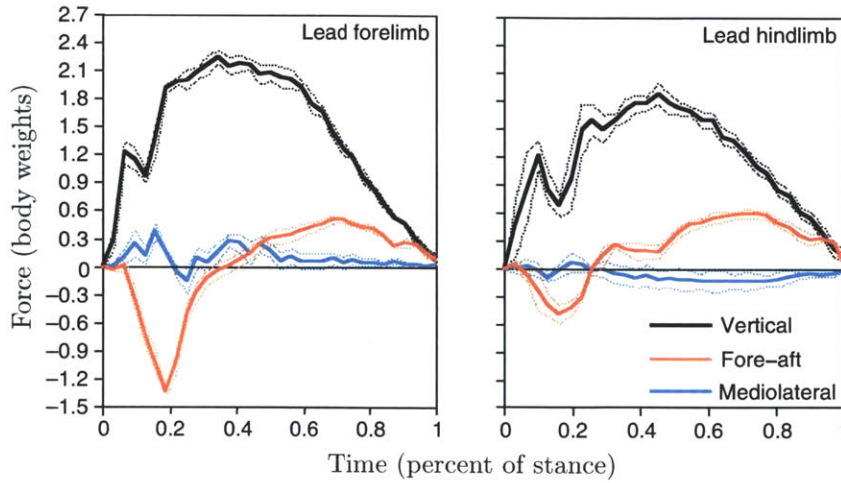


Figure 1-12: Ground reaction forces of a dog executing a rotary gallop. Adapted with permission from *The Journal of Experimental Biology* [62].

In the rotary gallop, $B \doteq \sum \beta$. Thus as the combined duty factor is decreased, average vertical loads at the foot increase. If only aerodynamic drag is considered, the net propulsive force may be similarly calculated as

$$\overline{F}_x = \frac{\frac{1}{2}\rho v_x^2 C_D A}{B}, \quad (1.2)$$

where C_D is the drag coefficient, A is the frontal area and ρ is the density of air.

The first phase of the ground reaction force profile is impact. During this time the foot strikes the ground with some nonzero velocity. Relative compliances of the ground and leg may cause the contact forces to oscillate briefly. This phase of the force profile terminates when the foot firmly comes to rest on ground, which is often somewhat difficult to precisely determine. The character of the forces generated during this time depend heavily on leg morphology. The effective mass of the robot as seen from the foot, sometimes referred to as the unsprung mass, is of particular importance [33], as are the stiffness and damping characteristics of the footpad [10] and the configuration of the leg [20]. In humans, modulation of these impact forces by varying touchdown configuration is easy to experience. Compare the initial impact of landing after a vertical jump with feet flat and legs straight, to the impact that results when the knees are bent about ten degrees. Clearly not only does

the impact influence the initial forces that are generated, but it also influences the forces required throughout the remainder of the stride to produce the desired dynamic response (in this case bringing the body to rest). This likely occurs because altering the impact conditions changes both the configuration and the net impulses imparted at the conclusion of the impact.

As the previous experiment has shown, the impact of the foot provides a set of exit conditions which then require precise muscle control to bring the stride to a successful conclusion. This is the second phase of stance, often called support. The support phase is characterized by active control of the leg musculature to impart the desired forces on the body using the foot-ground interaction. During running, the derivative of the fore-aft force generally changes from negative to positive as the impact ends and shortly afterwards the leg begins to generate forces in the forward direction at the foot [62]. In leg structures with joint redundancy, such as the digitigrade structure, some discretion is required in distributing torques amongst the joints in order to ensure that the joints remain near their optimal operating orientations.

As the stride nears completion the knee joint approaches its maximum extension, and several changes occur to maintain ground contact and to lengthen the stride. These changes occur during the end of the support phase. The ankle begins to rotate away from the body and increase the total length from the point of contact to the hip. This recruits the effort of the lower limb muscles [4]. Both the vertical and horizontal forces begin to decay, the vertical often more quickly than the horizontal. Ultimately, the phalanges lose contact with the ground and rotate caudally as the limb enters its protraction phase.

The front and rear legs of quadrupeds appear to perform somewhat distinct tasks. The front legs tend to exhibit more stabilizing and decelerating forces while the rear limbs provide similar or larger propulsive effort with lower vertical loads [62]. Clues to this specialization can be seen in the relative length of the aerial phases that follow the front and hind stances in a rotary gallop [18] and in the differences in force profiles [62]. The action of the spine may also contribute to this asymmetry. Higher vertical forces are experienced by the front legs than the rear which may be due to the location of the center of gravity (CG). For quadrupeds the CG is generally forward of the geometrical center between the hips and shoulders [30].

1.3 Background: Dynamic Performance

In searching for insight into the next steps required to advance the development and capabilities of legged robotic platforms perhaps something can be learned from the early history of motor vehicles. Early horseless carriages (ca. 1895) performed all of the same basic tasks as modern vehicles, if they are considered under quasi-static operating conditions. The vehicles turn to either side, move forward, stop and provide seating for the occupants. Over the following thirty years the development of the automobile proceeded at a tremendous pace, and a close examination of all of the changes made over this period show one overriding principle. Each change is intended to enhance the transient (or dynamic) performance of the vehicle [43]. Since the road is not perfectly flat, better suspension systems were developed, which maintained more uniform loading on the tires, enhancing tractive forces. Wider pneumatic tires also improved traction, and thus the capacity for acceleration. More powerful engines make use of the tires' enhanced grip on the road. A wheeled vehicle is an inherently dynamic device, and therefore the metrics used to measure the impact of a specific change must also be dynamic in nature.

For autos the engine horsepower is one such metric, as is the frequency response of the suspension. Both of these metrics include the vital temporal element that provides clues towards the effect changes in these metrics have under dynamic conditions. Currently, no such tools exist for the designer of a legged robot. This makes it difficult to develop a clear understanding of how design changes will impact the rather complicated dynamics of legged locomotion. My hope is that developing such tools, or merely pointing out the urgent need for them, will result in better design of dynamic robotic systems. Several such tools are proposed in Chapter 5.

Chapter 2

Design Principles

The ultimate goal of any leg is to harness interactions with the terrain to efficiently and robustly generate the locomotive forces demanded by the application. In other words, the leg must possess the ability to drive the body to a specific dynamic state based on the available sensor data and control algorithms. The first objective of the analysis presented within this chapter is to identify characteristics of the physical system that enhance the ability of the leg to reach the desired dynamic state, particularly in the presence of uncertainties in sensed or modeled parameters. This is approached through a detailed analysis of the three distinct phases of a stride (impact, stance and swing) and the unique characteristics that they each suggest. Once these desirable characteristics are identified, an effort can be made to expand the range of attainable dynamic states by discerning the factors that limit dynamic performance. Following the development of these robustness and performance imparting characteristics, a set of simple and balanced leg design criteria are proposed.

2.1 Operational Phases

The dynamic behavior of an actuated mechanical system can be expressed in many ways. The approach taken here is to quantify the dynamic characteristics of the leg in terms of differences in *mechanical impedance* [45]. The mechanical impedance relates the dynamic behavior of the leg endpoints (one at the body and one at the foot) to the forces that develop between them. Because the leg, under the influence of the leg controller, may be equiva-

lently represented by a virtual mechanical system [19], issues of physical hardware design and control may be considered concurrently. Following the analysis of the impact, stance and swing phases, the total impedance is strategically decomposed to yield insight into mechanical design considerations, the control system, and how these two vital elements interact to achieve robust locomotion.

In the general case of a foot contacting the ground, the body will experience three independent reaction components (two forces and a moment) at the point where it joins the leg. However, under the simplifying assumption that the foot-terrain interaction supports negligible moments about the point of contact, only two of these reaction components due to the contact loading remain independent. The force component along the leg and the moment at the body are taken as the independent components, leaving the force perpendicular to the leg dependent (cf. Figure 2-1). For the purpose of this qualitative impedance analysis it is assumed that these two independent components may be decoupled, into two one dimensional dynamic systems; one representing the extension and contraction of the leg and another, rotationally analogous system, representing the fore and aft rotation of the leg about the shoulder.

For each system the total mechanical impedance Z_t is composed of two elements, the passive (physical) impedance Z_p , and the active (virtual) impedance Z_a [31]. The passive impedance represents the physical reality of the manipulator. It is, in a sense, an expression of the dynamic character of the leg. The active impedance on the other hand is due purely to effort applied by the actuators, and it allows the manipulator to mimic the impedance characteristics of alternative physical systems. However, because the active impedance is the result of actuator, sensor and control system involvement, it inherits the limitations of each of these systems. The two most substantial factors to consider in the establishment of locomotion design principles are *control loop time* and *actuator saturation*. Each of these factors limit the degree to which the desired active impedance can be achieved, thereby limiting the total impedance to

$$Z_t = Z_p + \delta_c Z_a \quad (2.1)$$

$$\delta_c = \hat{\delta}_c(Z_a, \omega), \quad (2.2)$$

where δ_c is the degree of capability, a coefficient with values ranging from zero to one, and ω is the angular frequency of the input motion. As the limits of the controller and actuator are approached, δ_c decreases substantially from an ideal value of one, and the total impedance begins to inherit the character of the passive impedance alone [31]. Thus, for the very high frequency regime it is difficult to create the impression that the leg is anything other than the physical system. This motivates the analysis of the first phase of contact, impact.

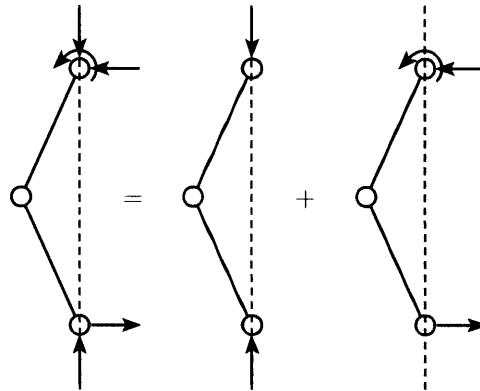


Figure 2-1: Decoupling of body reaction forces into two one dimensional systems.

2.1.1 Impact

During each stride, the leg transitions from the swing phase to the stance phase by undergoing an impact of the foot [62, 33]. This impact may be the intentional result of swing leg retraction [27], or the unintentional result of premature leg actuation, perhaps due to sensing errors. In either case, it is difficult to precisely match the velocity of the foot to the relative velocity of the ground during dynamic locomotion, and thus an impact must be considered unavoidable. Two considerations guide the impedance selection process during this phase. First, the forces generated during the collision should not be directly transmitted to the body. This demand stems from the desire to possess full knowledge of the forces exerted on the body at all times. If forces are allowed to be transmitted, then their magnitude cannot be predicted and predictions of the body state immediately following the impact will be inaccurate. The second demand is that contact forces, specifically the magnitude of the

impulsive load on the foot, should be small. This is purely a practical consideration, aimed at reducing the structural demands on the leg hardware.

To determine the impedance that achieves such characteristics consider the simplified one dimensional impedance model that represents the compression and extension of the leg (cf. Figure 2-2). During impact, an inherently high frequency event, the velocity of the foot changes suddenly. Throughout this event the body is assumed to remain, for all practical purposes, stationary. Applying (2.1) to this physical system and analyzing the high frequency domain indicates that in order to achieve the design targets the following relation must hold:

$$\lim_{\omega \rightarrow \infty} Z_t(j\omega) = 0. \quad (2.3)$$

In words, the total leg impedance in the high frequency regime should be as low as possible. Now, following from the discussion of (2.1) and (2.2), the total impedance during high frequency motion will be predominantly due to the passive impedance of the leg (Z_p). This implies that in order to limit the transmission of impact loads to the body, measures must be taken in the design of the physical system to reduce as much as practical the passive leg impedance. Two methods of realizing this goal are reduction of mass, damping and stiffness of the entire leg or the selective addition of a redundant, low impedance, degree of freedom (cf. Figure 2-3). Implementation of the second approach is complicated by the high force transmission demands of stance, which would cause large motions in a low impedance element, such as a soft spring. A compromised solution is to employ a nonlinear compliance at the foot. Such a nonlinear compliance would initially be soft, requiring little effort to deflect, and would stiffen as loading on the foot increases, perhaps becoming effectively rigid as it comes to bear the entire body weight. This approach has the distinct advantage of selectively reducing the impedance during impact beyond the level that may be possible for the remainder of the leg. However, the addition of a passive redundant joints generally complicates control.

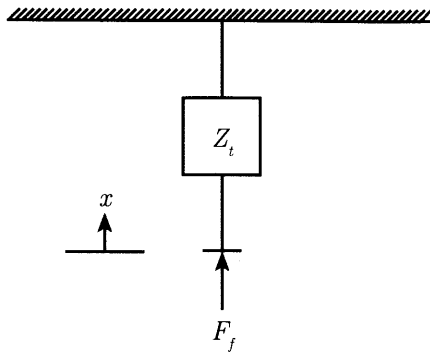


Figure 2-2: Model of leg extension and compression during impact. The body is effectively immobile and the foot experiences a step change in velocity

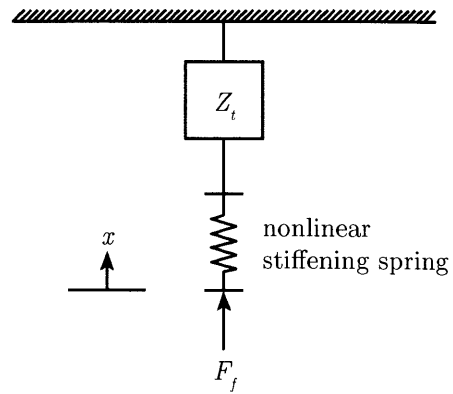


Figure 2-3: A method of reducing impact impedance is the introduction of a nonlinear spring in series with the leg.

2.1.2 Stance

The stance phase is undeniably the most crucial period of leg operation and therefore must be considered thoroughly. During this period the leg has access to a medium (the terrain) that allows it to apply a limited range of forces at the foot. The foot-terrain interaction of the most consequence to locomotion is the development of forces within the plane of the ground. Although this interaction is generally quite complex, and an area of ongoing research [8, 24], the Coulomb Friction model provides sufficient depth to develop a design strategy for relatively rigid surfaces. The task of the leg is to use this interaction to precisely control the dynamic state of the body at the end of stance. Two extreme approaches to achieving this goal are to either attempt to control the trajectory of the body through space or to attempt to control the forces applied to the body. Both of these methods are special cases of impedance control [20], and each will produce fundamentally different responses when subjected to common disturbances. The ideal leg impedance must be well balanced and capable of mitigating the destabilizing effects of a wide array of disturbance types. However, it is beyond the scope of this document to identify the specific impedance characteristics that result in robust locomotion, instead the aim is only to characterize the demands on the physical system.

The selection of a suitable impedance relies heavily on a sound mathematical formulation of the fundamental locomotive goals. During steady running the task of the controller is to direct the evolution of a stride such that the same stride may be repeated indefinitely to move forward across the terrain. However, the presence of disturbances complicates the practicability of this ideal behavior. The apex state of the body captures the stride to stride variations that lie at the center of this issue clearly and concisely. If the controller output for a nominal stride is used in the presence of disturbances, then the apex state following the stride will most probably differ from the initial apex state. As these differences aggregate, the propensity towards failure grows. In this case, the control framework lacks the necessary flexibility to respond to disturbances in a manner that maintains the elements essential to steady locomotion. Assuming for a moment that the legs are massless, and therefore that their precise position and motion has no bearing on the position or orientation of the body at apex, the values that may differ from stride to stride are:

- dT — difference in stride period
- dx — difference in body horizontal position
- dy — difference in body vertical position
- $d\phi$ — difference in body pitch angle
- $d\dot{x}$ — difference in body horizontal velocity
- $d\dot{\phi}$ — difference in body pitch rate

Of these the first two errors (dT and dx) vanish if the following stride is undisturbed. The final four errors, on the other hand, will likely be preserved or amplified, even if the following stride is undisturbed. This suggests that a reasonable approach to enhancing the robustness of stance is to direct the effects of disturbances to either changes in stride period or horizontal position.

The aptitude of the leg in dispensing with each disturbance type lies wholly in the magnitude and character of the leg impedance. To identify the influence of impedance character

(spring, damper, etc.) on stride to stride disturbance transmission a simplified two dimensional model is employed. This model is similar to the spring loaded inverted pendulum (SLIP) model, but it employs a leg of general mechanical impedance. The model consists of a single massless leg supporting a point mass at its proximal end (cf. Figure 2-4). The goal of such a system being to move forward over the terrain with minimal stride to stride variation in the apex state. Clearly this model provides no means of directly assessing the transmission of pitch errors. However, this shortcoming is of little practical significance for quadrupeds because pitch may be interpreted as vertical position differences between the front and rear leg pairs. Furthermore the goal of this model is not to develop a precise control algorithm; simply to understand how impedance relates to the qualitative behavior of the body during stance. The disturbance types considered are:

- F_{dbx} — disturbance force on body in x direction
- F_{dby} — disturbance force on body in y direction
- \dot{x}_d — disturbance in x velocity
- m_d — disturbance body mass

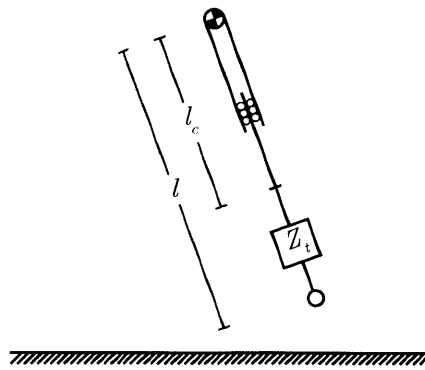


Figure 2-4: Two dimensional, one legged hopping model of locomotion with a leg of general impedance Z_t in series with a prismatic actuator.

A fixed body mass ($m = 20kg$) and single component impedance (either spring or damper) is used to achieve the desired apex state. However, several constraints on the stance

forces must be imposed to arrive at a realistic behavior. The first of these is that the foot forces must start and end at zero and be continuous. This ensures that the leg is not subjected to any impulsive loading during stance. Second, the foot must only exert compressive forces on the ground, otherwise the leg will lift off, signaling the end of the stance phase. The forces for the spring and damper legs are given by

$$F_s = -k(l - l_c) \quad (2.4)$$

$$F_d = -b(\dot{l} - \dot{l}_c), \quad (2.5)$$

where k and b are the apparent stiffness and damping ratio of the leg, l is the leg length and l_c is the commanded actuator length. To achieve the desired response with a spring leg constant values of l_c and k may be commanded. However, for a damper leg \dot{l}_c must be varied with time for a fixed b . The commanded velocity (\dot{l}_c) is chosen to provide the same force profile as the spring for a nominal stride. The leg touches down with an angle of 30° to the vertical. The initial apex height is 1 m and the forward velocity is $3 \text{ m} \cdot \text{s}^{-1}$.

Simulating the motion of the system from one apex to the next, the effect of the four disturbance types was analyzed. The spring leg suffered less from disturbances to the horizontal and vertical force on the body (cf. Figure 2-5 and 2-6). Forces in the negative x direction tended to result in higher apex states while forces in the negative y direction tended to lower the apex. When a disturbance mass is introduced to the body the damper leg yields less variation in apex height (cf. Figure 2-7). This is primarily due to the velocity command of the damper possessing a fixed frequency. This tends to reduce foot forces late in stance, which in turn reduces variations in contact duration. On the other hand, increasing body mass decreases the natural frequency of the spring-mass system, tending to increase the duration of stance. Horizontal velocity disturbances had less of an effect on the spring leg, this is possibly due to the fact that as forward velocity increases the fixed \dot{l}_c command of the damper leg becomes less synchronized with the angular orientation of the leg on the ground (cf. Figure 2-8). These results hint at the complexity of precise impedance selection and indicate that an ideal impedance may combine the features of various pure impedance types. Furthermore, the precise magnitude of the impedance must vary with forward speed

in order to meet the changing demands of total impulse and stride duration.

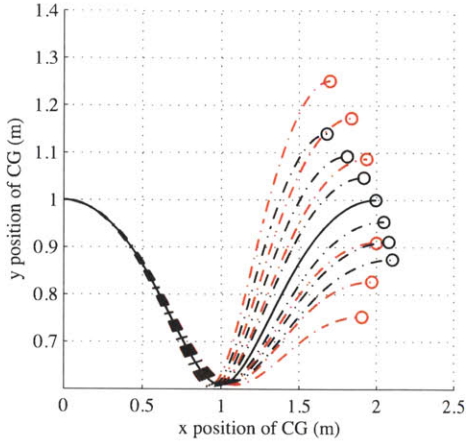


Figure 2-5: Effect of horizontal disturbance force (F_{dbx}) on one leg hopper with spring-like leg impedance (black) and damper-like impedance (red).

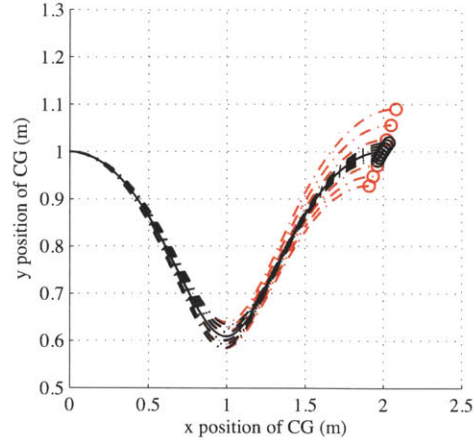


Figure 2-6: Effect of vertical disturbance force (F_{dby}) on one leg hopper with spring-like leg impedance (black) and damper-like impedance (red).

This analysis identifies two desirable features of the mechanical system. First, because the leg impedance is expected to change throughout the speed range, the majority of the impedance during stance must be due to the contribution of the actuator in the form of Z_a . Second, to maximize the range of impedances that may be achieved the actuator must be made powerful.

2.1.3 Swing

Forces during the swing phase, unlike impact and stance, are governed purely by the inertial characteristics of the mechanical system. Depending on the application, these swing phase reaction forces may provide a desirable degree of control over body behavior, particularly in the pitch control of bipeds [29]. However, large swing forces also tend to slow protraction and increase the dynamic coupling between the body and legs. The lack of contact during this period suggests that there is no specific impedance goal to speak of, simply the notion that the inertial characteristics, together with a protraction trajectory, result in the generation of a restricted range of reaction forces. Consequently, the relative benefits and drawbacks of altering the mass and inertia of the leg must be thoroughly explored.

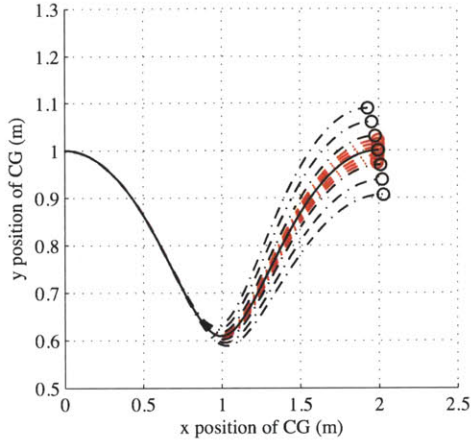


Figure 2-7: Effect of mass disturbance (m_d) on one leg hopper with spring-like leg impedance (black) and damper-like impedance (red).

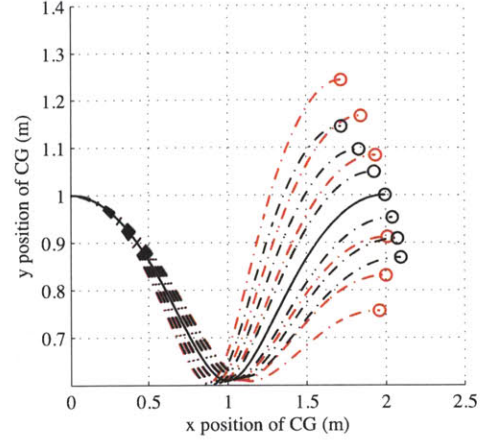


Figure 2-8: Effect of horizontal velocity disturbance (\dot{x}_d) on one leg hopper with spring-like leg impedance (black) and damper-like impedance (red).

If the leg inertia is increased it becomes possible to apply larger forces to the body during the swing phase. This may help to correct small errors in body orientation during flight. However, the nature of the forces that may be applied is not arbitrary, and to a large extent depends on the mechanical configuration of the leg [60, 46]. The initial and terminal leg locations during the swing phase are generally fixed, requiring the leg to be moved from a posterior to an anterior position. This leaves only the temporal evolution of the protraction free to be altered, severely restricting the character of the body motions that may be generated. The mechanism behind the ability to alter body orientation during swing is the development of stronger dynamic coupling between the leg and the body. From the perspective of controller design such coupling is undesirable, and a source of substantial complication because the controller is forced to consider both the leg and the body as a single mechanical entity. On the other hand, decreasing the inertia will result in consistently lower body forces and a reduction in the body to leg dynamic coupling, facilitating the separation of leg and body dynamics.

In the case of quadrupeds the need for swing phase reaction forces is uncertain. The availability of leg pairs fore and aft of the center of gravity allow pitch adjustments to be made by altering the relative magnitudes of stance forces. Furthermore, the inherent complication such coupling introduces into the control system diminishes its attractiveness, particularly

because the dynamic coupling will continue to exist during stance, forcing the actuators to support larger dynamic loads. Given the intrinsic complexity of developing a dynamic robot the appeal of decoupling the leg from the body is too great to merit sacrificing for the relatively limited control authority available during protraction, particularly when an alternative method (such as a tail) may be introduced instead. Dynamic decoupling is a feature that will come to lie at the center of the overall control strategy, and thus it is considered essential to reduce the leg mass and inertia to the greatest possible extent.

$$m_{leg} \ll m_{body} \quad (2.6)$$

$$I_{leg} \ll I_{body} \quad (2.7)$$

2.2 Performance Limits

As the locomotive goal of this robot is to achieve the highest possible speed, particular attention must be paid to the factors that define the upper limits of performance. In biological systems the force-velocity and force-length characteristics of the muscle groups employed during gait execution form the core of the system that tends to limit running speed [25]. These characteristics are the biological equivalent of the *actuator dynamics* that limit the response of robotic systems. The shape of the force-velocity and force-length curves for skeletal muscle have a tremendous impact on gait, leg structure (kinematics) and muscle distribution [65]. Together these components produce the performance that is recognized in the natural world, but independently they hold little value. Their strength comes not from any single element, but from the system as a whole. The challenge of achieving high performance in legged robotics is to develop a unified system around a fundamentally different actuator.

Leg kinematics and the accompanying musculature work in concert to generate the desired locomotive forces. The leg structure guides muscle distribution and the limits of muscles guide leg structure. This interplay between actuation, kinematics and the dynamics that they ultimately produce, must be realized for effective high-speed locomotion. If this harmony is not achieved, an individual element of the system, instead of the system as a whole, would define the performance limit. The element that most commonly shoulders

the burden of an unbalanced design is the actuator.

The principle consequence of limits on actuation forces is a reduction in the ability to provide the propulsive forces required to maintain speed. At the maximum speed the net propulsive impulse over a stride is equivalent to the impulse due to drag. Drag is often made up of several components, such as joint friction, soil work and aerodynamic forces, which will vary in magnitude depending on, among other factors, the speed and the gait. At high speeds, aerodynamic drag may become a dominant component, along with the leg-motive friction that results from the movement of the motors, bearings and joints. Although it is not possible to completely eliminate either of these factors, they may be reduced to increase maximum running speed.

Another form of friction has enormous implications on the performance limit: the frictional interaction between the foot and the ground. Foot-terrain friction is the medium through which all propulsive forces are exerted, and as such, performance is maximized when the limits on friction forces are high. To attain the large friction forces required for fast running it is often necessary to exert large vertical forces (normal loading). This requirement places additional demand on the actuators. A high friction coefficient between the foot and the ground can ease this type of secondary loading, but even if the Coulomb friction coefficient (μ) is one a unit increase in horizontal force requires that the total force be increased by $\sqrt{2}$. One method of circumventing this troublesome interaction is the use of claws to mechanically grip the surface.

The weight of any dynamic system is of the utmost importance. Whether it is an automobile, aircraft or a piece of sporting equipment the overwhelming trend is that when high dynamic performance is desired, weight must be kept to a minimum while power is pushed to the maximum [43, 38, 15]. The cause of this trend is as simple as Newton's second law. If it is possible to reduce the weight of a system without compromising its ability to generate forces, then the system will be capable of achieving higher accelerations or better "dynamic performance". The practical difficulty in applying this rationale stems from the fact that it is not always possible to reduce the mass and maintain the same force generating capability. If mass as well as force are reduced simultaneously, at what ratio does the performance begin to decrease, and at what force level is the performance compromised?

In the automotive industry the ratio of force generation to mass is typically supplied as the power-to-weight ratio, and if dynamic performance is to be increased, this value should be made as large as possible. However, in order to determine the optimal power level, and thereby the precise weight, additional information on the operating conditions is required. Assume for example that the design intent is to drive as fast as possible in a straight line. Taking two identical cars with the same power-to-weight ratio, but one with ten times the power and weight and accelerating them to their maximum speeds, several key differences become apparent. Initially, the cars accelerate at a similar rate. However, the less powerful car, slowed by aerodynamic drag, attains a lower maximum speed than the more powerful car. This difference occurs because at the performance limit the power of the car is not absorbed by the acceleration of its mass but by aerodynamic drag and rolling resistance. If the same cars are compared in a dynamic performance test, such as maximum speed through a slalom, often the lighter car will perform better due to nonlinearities in tire and suspension behavior [43].

In a legged system the maximum speed behavior is a combination of these two extremes. The actuator forces must counter any aerodynamic drag and produce fore and aft accelerations of the legs. Thus not only must actuator power be high, the leg masses and inertias must be very low, in order to limit the effort required to produce their reciprocation. This ensures that work done throughout a stride goes into producing useful forces at the shoulder as opposed to accelerating and decelerating the leg.

The limb and body must also adhere to strict structural limits. In biology the cost of exceeding the loading limits on bone, muscle or tissue is injury or death. In robotic systems, exceeding the structural limits will result in yielding or catastrophic failure. In either case these are situations to be avoided. Robotic systems have a material advantage in their ability to implement features of various chemical composition such as metals, plastics and composites. However, nature has a structural advantage in its ability to shape a limited selection of materials with nano-scale precision [3]. The union of material and structure must be tailored to perform under the anticipated loading conditions. Stated differently, if the material is not bone, then it need not retain the physical structure of a bone to retain its function. This structural constraint often defines the lowest possible degree of weight reduction.

2.3 Design Criteria

The analysis of the previous two sections highlights several of the key issues that limit the effectiveness of a leg design. The reduction of this information into a set of simple design criteria aids its introduction to the design process. The following four criteria are proposed, with the intention of instilling a leg design with a balance of robustness and performance. To achieve this the leg must exhibit:

- Low passive mechanical impedance
- Low mass and inertia
- Strong actuation
- Harmony between kinematics and use

The necessity for low passive mechanical impedance originates from the demands of impact and stance. During impact, a large impedance amplifies small errors in the foot velocity with respect to the ground into large body forces. These forces alter the state of the body unpredictably, which makes the pre-impact planning of a stride impractical. Due to the dynamic complexity of a running system it is computationally difficult to re-plan the stride post-impact. This difficulty is avoided if the passive impedance is decreased, insulating the body from rapid motions of the foot. Although the impedance must be increased during stance this may be accomplished actively owing to the substantially longer duration of stance relative to impact.

Mass and inertia of the leg affect the behavior of the system throughout all areas of leg operation. But their influence is most clearly visible during protraction and in defining the limits of dynamic performance. During the swing phase the leg is dynamically coupled to the body and the degree to which motions of the leg influence motions of the body increases with increasing mass and inertia. However, unless swing phase reaction forces are absolutely essential to the application, these coupling reactions serve only to complicate control. Furthermore, reduction of the leg mass and inertia increases the maximum acceleration and deceleration of the leg for fixed maximum actuator loads.

Strong actuation increases the range of realizable leg impedances and provides ample effort to counter inescapable losses such as aerodynamic drag. This type of loss, along with the losses inherent in the active acceleration and deceleration of the leg, ultimately come to limit the maximum running speed. However, strong actuation alone is not an indicator of success. The actuator merely sets the foundation for the remainder of the system to build upon.

Balance between the form of the leg and its use ensures that every element of the system operates to its full potential. The kinematics, dynamics, actuator and gait are heavily interdependent. No individual element stands on its own. Thus when one component changes, the remaining elements must be reevaluated and refined iteratively. Direct imitation of specific aspects of a biological system in robotics disregards the fundamental differences between the two. Embracing these differences allows a design solution to develop organically instead of forcing elements together that were not intended to fit.

Chapter 3

Leg Design

This chapter begins by delineating the design space, specifying particular targets for weight, size and speed. Next, a conceptual framework is developed for the leg design, establishing the ideas and design direction that enable the design goals to be met. After this framework is put in place the detailed mechanical design is presented for both front and rear legs.

3.1 Design Space

The intent of this research project is to develop a quadrupedal robot capable of true dynamic running in three dimensions with a maximum speed greater than $13 \text{ m} \cdot \text{s}^{-1}$ or $50 \text{ km} \cdot \text{h}^{-1}$. This speed is well above the highest observed speed for legged robots ($6 \text{ m} \cdot \text{s}^{-1}$) which was established in 1984 by Raibert et al. [51]. The robot is to complete this task standalone, without tethers, electrical or hydraulic assistance over nominally flat, natural terrain, such as a grass or dirt field. The ability to maneuver within the human environment, in a manner similar to a dog or large cat, stands as a long term goal that imposes specific constraints on size, shape and weight.

As a starting point, a fully extended leg length of approximately 50 cm and total weight of 35 kg was defined. These values, particularly the leg length, are design parameters that are flexible and are intended merely to guide the design of the robot to an appropriate size. The aggressively minimized weight budget of 35 kg permits 3.5 kg for each front leg and 3.75 kg for each of the rear legs (cf. Table 3.1), these values include both actuation and the

Component	Weight (kg)
Front leg (ea.)	3.50
Rear leg (ea.)	3.75
Ad/abduction	1.25
Body structure	5.25
Computation	3.50
Batteries	10.50
Total	35

Table 3.1: Weight budget for the quadrupedal robot.

mechanical structure. The loose confines of the design space allow many possible directions to be explored, each with its own set of advantages and disadvantages. The section that follows details the identification a suitable design direction and set of design ideas that form the basis for the detailed final design.

3.2 Conceptual Framework

The goals of this project can undoubtedly be approached in many different ways. Among the highest level decisions to be made is the selection of a suitable *leg topology*. A leg topology is the physical arrangement of the degrees of freedom that make locomotion possible. This definition of leg kinematics has a powerful effect on gait generation, force production, and how force production at the foot and body vary with increasing speed. Three leg topologies suitable for dynamic running are the prismatic, articulated and redundantly articulated configurations (cf. Figure 3-1).

Possibly the simplest workable leg design combines a single prismatic leg link with a rotational joint at the hip (cf. Figure 3-2). This topology was applied with impressive results by Raibert et al. in the 1980s, and a robot of this type still holds the speed record for legged robots. Several leg lengthening actuator options are available to the designer of such a system. Specifically hydraulic actuators, linear motors, rack and pinion and lead-screw initially appear suitable for the task. In comparison to the forces required to lengthen the legs, the torques required at the body pivot are rather small [33].

This type of leg exhibits several extremely convenient dynamic characteristics that sim-

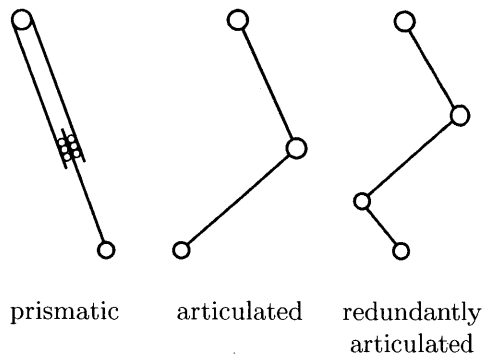


Figure 3-1: Prismatic, articulated and redundantly articulated leg topologies. Revolute joints are indicated by circles and prismatic joints by rollers.

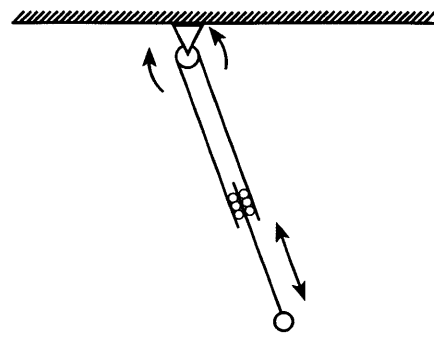


Figure 3-2: The prismatic leg consists of a revolute joint at the body and a prismatic joint within the leg.

plify controller implementation. During stance, if the hip joint is left free and the leg assumed to be massless the ground reaction force vector points along the leg from the foot to the hip and has a magnitude that is directly controlled by the leg length actuator force. In this type of gait the leg is capable of producing propulsive forces after reaching midstance. The simplicity of this decomposition, in which only hip angle and actuator force determine the force exerted on the body, is very attractive from the perspective of control.

The use of a linear hydraulic actuator for the generation of leg lengthening forces was also pioneered by Raibert [51]. This actuator selection has several practical advantages. First, the actuator is relatively lightweight and high force, particularly if the hydraulic compressor and accumulator are not located on the robot. Furthermore, the mass that exists in the leg functions as both the actuator and leg structure. When the passive impedance of hydraulic actuator is modulated by the addition of a serially located pneumatic spring, the high speed and high thrust characteristics of hydraulics allow the leg to support a quick, powerful and stable stance phase. If the pneumatic spring were omitted from this design, the relatively small passive compliance of the hydraulic actuator would result in a large passive impedance. Because of this, impact forces would be very high unless the velocity of the foot, relative to the ground, could be precisely controlled. These impact forces and the resulting fluctuations in body forces, would likely make the robot difficult to control. The combina-

tion of speed and force afforded by hydraulic actuation is difficult to obtain at similar mass levels for alternative prismatic actuators.

A principle disadvantage of implementing a topology of this sort, utilizing hydraulic actuators, is the fundamental inability of the actuator to cope with increasing leg extension speeds and the larger forces that accompany them. The force production capabilities of hydraulic actuation are very good, particularly at high loads and intermediate speeds. However, as speed increases fluid losses increase. This imposes a relatively strict limit on maximum running speed which, although high, may be challenged by a leg topology that offers greater actuation flexibility over the speed range. Another disadvantage of hydraulic actuation is the difficulty of executing precise control, particularly when high reservoir pressures are used at low speeds [23]. In addition, the actuation of more than one leg may unpredictably change the forces generated by a given control input if the legs use a common hydraulic accumulator.

An alternative to the strictly prismatic leg is the articulated leg. That is, a leg with a single rotational joint used to control leg length, similar in function to the knee or elbow of a quadruped (cf. Figure 3-3). This topology alters the actuator requirements from a combination of rotary and prismatic elements to two rotary elements, yet retains the same two planar degrees of freedom as the prismatic leg. If the shoulder is left free this limb produces forces in precisely the same manner as the prismatic leg. However, use of the rotational knee joint as a leg lengthening mechanism has some key implications for the force generation capability of the actuator. For a constant actuator torque at the knee the force generated between the shoulder and foot depends on the knee moment arm (cf. Figure 3-4). This *configuration dependent gearing* of the leg lengthening actuator is a key feature of any articulated leg design. Clearly, configuration gearing complicates the calculation of body forces because the force now also depends on the knee angle. If the leg links are given finite mass, the hip and knee degrees of freedom will interact non-trivially according to the passive dynamics of a double pendulum. These dynamics complicate control strategies and somewhat cloud the formation of an intuitive understanding of high speed locomotion.

The advantages of an articulated topology over the simpler prismatic layout lie within the configuration dependent gearing and increased workspace. If the limb is nearly straight,

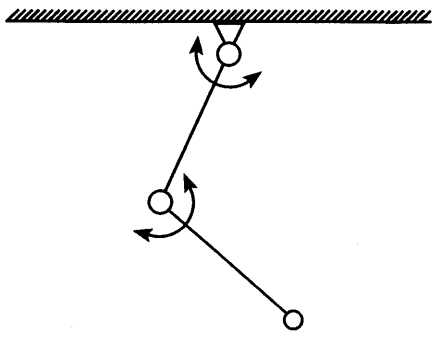


Figure 3-3: The articulated leg consists of two revolute joints, one at the body and another between the body and foot.

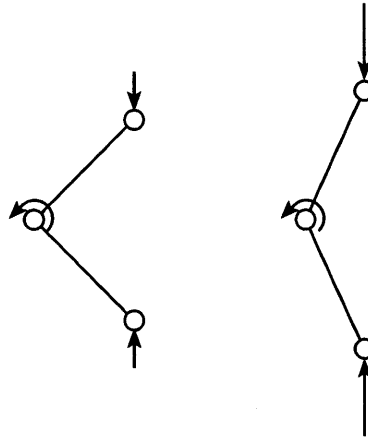


Figure 3-4: The force between the body and foot for a fixed elbow torque depends on the amount that the elbow is bent.

a relatively weak actuator can produce substantial extension forces. Under heavy loading it is possible to alter the gait in order to operate the leg near this singularity. Thus variations on a fundamental gait may be employed to alter the region in which the actuator operates. In humans, a common example of such a change is the adoption of a straight-leg gait with shorter steps while carrying heavy loads [39]. As the leg is bent further, the maximum extension force decreases, but extension or compression speed is increased. Thus the configuration dependent gearing aids in the production of both high load and high speed behavior, even if such characteristics are not inherent to the actuator.

An extension of the articulated topology is the redundantly articulated leg, a leg possessing more than one degree of freedom between the contacting foot link and the body (cf. Figure 3-5). Often redundantly articulated legs assume topologies that are geometrically similar to the digitigrade or unguligrade legs observed in biology. A digitigrade structure possesses two intermediate rotational joints, while an unguligrade possesses three. The draw of introducing additional degrees of freedom lies in developing the ability to augment the configuration dependent gearing, and thereby increase the performance of the leg as a system. For a given distance between the foot and the shoulder many leg configurations are possible, unlike the case a simple articulated leg (cf. Figure 3-6). This additional freedom can be used to design a stride trajectory that places the leg in configurations that dynamically

match the force and speed requirements at each instant in time. The additional joints also allow the passive impedance to be altered during impact and throughout the stride. Unfortunately this increase in leg ability comes at the expense of additional actuators. And increasing number of actuators substantially increases controller complexity, sensing requirements and structural demands, particularly if actuators are located far from the body. The addition of actuators make it difficult to directly compare the performance of a redundant leg to either of the simple legs.

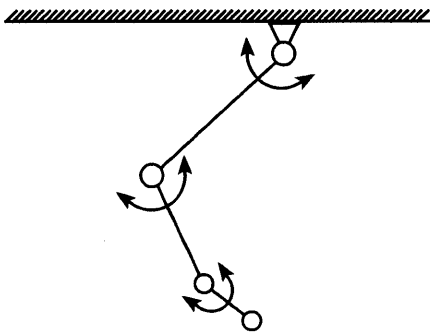


Figure 3-5: The redundantly articulated leg consists of three or more revolute joints.

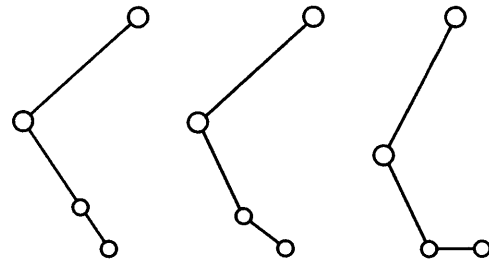


Figure 3-6: Three possible joint configurations with the same leg length (from shoulder to foot). Freedom to modify configuration may aid in maintaining joints near optimal operating conditions or alter the passive impedance.

Of these topologies the articulated leg was selected, as it appears to present the greatest balance between complexity and ability. The use of prismatic legs, particularly those actuated by hydraulics, showed relatively few prospects for the substantial performance improvement required to meet the design goals. An articulated leg on the other hand has a dynamic and kinematic richness that, if harnessed effectively, may provide just that. The two actuation technologies considered for this task were hydraulic actuators and electric motors. The high force and high speed capabilities of a hydraulic system initially appeared attractive, however the development a lightweight self-contained system, complete with accumulator, hydraulic fluid, compressor and compressor fuel (batteries or liquid fuel) was anticipated to present substantial difficulties. This factor, combined with the relative diffi-

culty of controlling actuator impedance motivate the use of electric motors over hydraulic actuators. Thus the overall leg topology consists of an articulated leg driven by battery powered electric motors. A compliant, redundant foot link is used to reduce passive impedance during impact (cf. Figure 3-7).

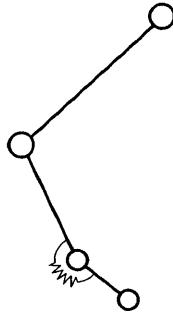


Figure 3-7: The leg topology selected is a articulated leg with one passive redundant joint that is intended to reduce impact impedance.

In pursuit of attaining the highest possible performance from a given motor one of three common failure modes must be approached [61]. The first, and most belabored of these is electrical failure, caused by the breakdown of the winding insulation. In low life motors this is typically attributed to exceeding the thermal limits of the winding insulation. As time over the thermal limit is increased, motor life decreases dramatically [7]. Thus to preserve the integrity of the motor, limits on the core temperature of the windings must be enforced. Next is the issue of magnetic failure. A magnetic failure is only possible in permanent magnet motors and will occur when the magnetic field induced by the stator is strong enough to demagnetize the permanent magnets. This generally occurs when loads and/or magnet temperatures are high [28]. The final failure mode is mechanical failure of the motor structure. Many application dependent factors may cause a mechanical failure, however, bearing failure is quite common, particularly when bearings are worn or the load rating is exceeded.

In the majority of DC motor applications input voltages are commanded to lie on or under a constant voltage curve [35]. The slope of this curve is the motor torque constant, which is generally assumed to be invariant of voltage. Such an implementation is safe, but leaves a substantial amount of the actuator's true capabilities unutilized, particularly the

short duration, high-power pulses that make up much of the loading in running systems. A redefinition of the motor limits to reflect the thermal, magnetic and structural failure modes tends to impose strict limits only on motor current. Thus, removing the artificial limit on voltage effectively increases the potential operating range to include much larger unloaded speeds. In the high load regime the thermal limit of a given motor can be visualized by the construction of a plot of time required to reach the thermal limit (from a reference temperature) versus motor current commonly referred to as a thermal limit curve. The torques that these currents induce are available at any speed, less friction or drag losses, provided sufficient voltage is available from the supply. Logistically, use of the thermal limit approach allows the designer to balance the proportions of relatively light batteries with often heavy and large actuators.

Under short duration, high torque, loading the majority of the thermal energy dissipated goes into increasing the temperature of the motor windings. This implies that one method of increasing the short duration performance of the motor is to increase its thermal mass. Equivalently, if provided with two seemingly identical motors one would expect the motor with higher thermal mass to perform better under impulsive loading conditions. The thermal mass of a given motor, which is largely due to the volume of the windings, can be increased by ensuring good thermal contact between the windings, stator and housing, or by placing heat sinks directly onto the exposed motor windings. Active methods of temperature management, such as water cooling or evaporative cooling, may also increase the high load performance at the expense of additional mass and complexity.

The functional, yet slightly naïve, approach to integrating actuation and leg kinematics is to place actuators at each joint, such that the actuator and joint axes coincide (cf. Figure 3-8). This approach conveniently compartmentalizes leg design and has been shown to work admirably under low speed, statically stable, conditions [26, 17]. However, for dynamic locomotion this compartmentalization presents several difficulties. Primary among these is that the placement of actuators far from the body has a tremendous impact on leg inertia, increasing it to the point that maximum swing frequency may become severely limited. A compartmentalized leg also goes against the ideal of developing the leg as a coherent system, capable of reacting sensibly to external influences. If the leg is heavily segregated,

with unrelated control loops driving each joint, it becomes difficult to ensure that the system-wide goal of body state control is not lost.

To address these issues, a new type of leg design was developed in which actuators for the shoulder and elbow both lie concentric with the shoulder joint (cf. Figure 3-9). This arrangement has the unique advantages of reducing the contribution of the elbow actuator to leg inertia about the hip and modularizing the actuation unit. Actuator torque is transmitted to the distal joint by a rigid tendon which is placed such that the presence of contact loads at the foot put the tendon in tension. The precise leg geometry, based in part on dynamic simulation results and kinematic constraints, is left flexible by actuator collocation because the leg members themselves retain a minimal number of precision interfaces. This simplicity of interface allows many different leg geometries and configurations to be explored and greatly simplifies system maintenance.

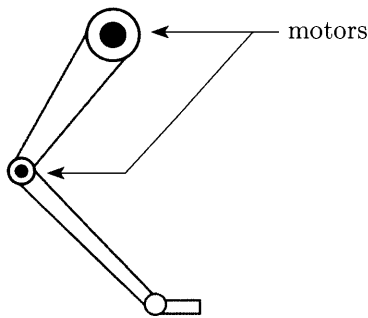


Figure 3-8: Simple leg design with the actuators at the joints. High shoulder inertia due to remote actuator mass limits swing speeds and increases shoulder actuator loads.

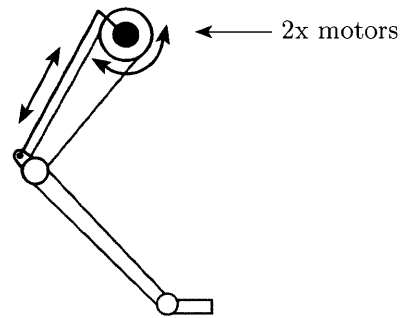


Figure 3-9: Doubly concentric actuator layout reduces shoulder inertia. Elbow is actuated by a four bar linkage with one bar being the humerus and another an extension of the radius behind the elbow.

Throughout much of the stride the leg links are under a combined state of compression and bending (cf. Figure 3-10). In order to reduce the structural demands on the leg links, and thereby open up the possibility of reducing leg weight, supplementary tendons are introduced. These tendons are intended to take a portion of the bending load, thereby reducing the moment loading on the leg link, in a manner similar to the guy lines of an articulated crane (cf. Figure 3-11). Such a design enables the use of a wide range of leg link materials, particularly plastics and composites.

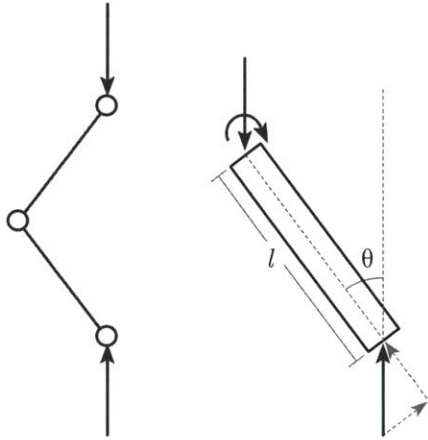


Figure 3-10: Left is a typical loading situation on a front leg during mid stance. This results in loading on the radius shown to the right.

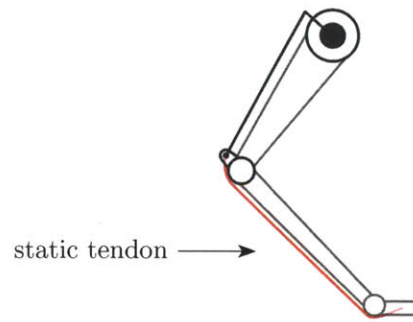


Figure 3-11: Bending loads in the radius are reduced by adding a lightweight Kevlar tendon from the foot to the tricep.

The final consideration in developing the ideas behind a detailed design is the need for abduction and adduction (henceforth referred to as ad/ab). This is the rotation of the leg out of the sagittal plane either toward or away from the body. This degree of freedom is accommodated by the inclusion of an additional rotational joint at the shoulder. The joint is parallel to the spine (perpendicular to the shoulder joint) and located on the medial side of the actuator unit.

3.3 Detailed Design

The following section develops the conceptual framework into tangible front and rear robotic legs. The unique features specifically discussed are the:

- Concentric actuator layout
- Use of motors to thermal limit
- Use of composites in leg fabrication
- Use of tendons to reduce structural loads

3.3.1 Front Leg

The design of the front leg falls within the weight budget and is rated to transmit peak compressive or extensive forces of up to 1000 N, equivalent to roughly three times the body weight (cf. Table 3.2). It has two active joints, the shoulder and the elbow, and a passive ankle (cf. Figure 3-12 and 3-13)



Figure 3-12: Front view of right front leg.



Figure 3-13: Rear view of right front leg.

Specification	Value
Max. load	1000 N
Shoulder torque (peak)	23 N · m
Knee torque (peak)	134 N · m
Shoulder range of motion	150°
Knee range of motion	107°
Max. leg length	480 mm
Min. leg length	238 mm
Weight	3.25 kg

Table 3.2: Front leg design specifications

Actuator Selection

The selection of a suitable electric motor begins with the unique demands of locomotion. Analysis of biological data and dynamic simulation highlights several trends which enable

qualitative comparison of the shoulder and elbow actuation demands. In running gaits, including the rotary gallop, the ground reaction force vector on the front feet generally points from the foot to the shoulder, rotating slightly fore and aft of the shoulder throughout the stride [62]. This suggests that for a lightweight leg, shoulder torque is relatively small in comparison to the force along the leg (from foot to shoulder). Elbow torque may be estimated by measuring the moment arm of the ground reaction force [5]. This moment arm is generally several times larger than the moment arm of the contact load at the shoulder. This trend implies that a stronger elbow actuator may be placed in series after a weaker shoulder actuator without jeopardizing the dynamic performance. Although the actuators are in series mechanically, they are effectively decoupled by joint placement and the dynamics of locomotion. Using these approximations the desired elbow joint torque of $120 \text{ N} \cdot \text{m}$ and shoulder torque of $20 \text{ N} \cdot \text{m}$ were established.

A review of available actuators indicated that these peak torques lied beyond the reach of lightweight direct drive motors and thus some gear reduction (of ratio N) was required for the elbow. Rotor inertia, when driven from the output through a gearbox scales with N^2 , thus in order to limit the contribution of the motor to the passive leg impedance the lowest possible gear ratio was employed. A low gear reduction also promotes the use of the passive system dynamics during locomotion tasks. The direct drive torque motor type suits the demands of locomotion because it provides large peak torques and possesses a large thermal mass. The large thermal mass increases the high load, low duration performance.

The two major classes of permanent magnet DC electric motors considered were brushed and brushless. A brushed motor uses several graphite brushes pressed into contact with a commutator. This commutator rotates with the rotor and directs currents to the proper windings based on rotor orientation. The principle advantage of this motor type is its simplicity of operation. A constant voltage applied to the brushes will result in rotor rotation and varying this voltage will alter rotation speed. The downside of this simple interface is twofold. First, the brushes wear, are susceptible to arcing at high currents and increase friction. Second, less control over the motor torque is available because the timing advance or switching point of the windings is fixed. A brushless motor, as the name implies, has no brushes and instead exposes the connections to each stator winding. These wires must be

driven in the correct manner by an external motor driver. The driver must sense the rotor position and apply the input current to the appropriate windings. The advantage of this arrangement is flexibility and reliability. Because there are no brushes to wear, maintenance is reduced, and the driver provides precise control over the distribution and timing of winding currents, enabling precise torque control. For this application, the precision and flexibility of a brushless motor design was preferred.

The weight of a motor was also a key consideration in actuator selection. The peak torque density or specific peak torque is a measure of the maximum available torque per unit mass of the actuator, it is typically highest for permanent magnet motors [13]. This quantity is important in legged robot design, because the actuators typically compose up to forty percent of robot mass [16]. Thus a 10 percent increase in actuator mass will likely result in robot that is more than 20 percent heavier. This additional mass must be matched by additional force production capabilities. Often it is not possible to achieve the additional force required for equivalent performance, therefore it is of the utmost importance to select the lightest actuators capable of generating the design torque. The scaling of torque density with typical motor parameters, such as diameter, is somewhat complicated due to the wide range of motor topologies and construction methods. However, large gap diameter motors generally provide more torque with a similar torque density to smaller motors, the cost that accompanies this increase in diameter is an increase in rotor inertia.

In pursuing the maximum torque density every additional component of the actuator design must be justified. A component that is often overlooked is the motor housing. Direct drive motors are commonly sold in framed or frameless configurations. A framed motor is an enclosed system with bearings between the rotor and stator while a frameless motor is provided as simply the bare rotor and stator. Designing around a frameless motor allows the motor housing to act as a stressed structural component. This is a design method that is paralleled in the world of motor sport, in which it is common to mount suspension components directly to the engine block or gearbox [58]. This reduces total mass and often increases strength.

Combining all of these diverse requirements a custom wound version of the Allied Motion HT05001 frameless motor was selected (cf. Figure 3-14). This motor has a suitable

Property	Value
Peak torque (demagnetization)	23.2 N · m
Peak current (at peak torque)	69.5 A
Torque sensitivity	0.334 N · m · A ⁻¹
Terminal resistance	0.791 Ω
Number of poles	12
Number of teeth	45
Phase connection	wye
Stator outside diameter	127.0 mm
Length over coil	40.3 mm
Rotor inside diameter	63.5 mm
Weight (rotor + stator)	1.23 kg
Rotor inertia	2.2 × 10 ⁻⁴ kg · m ²

Table 3.3: Motor parameters for custom wound HT05001 torque motor.

size, shape, weight, and with custom winding is capable of peak torques larger than 23 N · m (cf. Table 3.3). This peak torque makes the design goal of 120 N · m possible with a gear reduction of less than 6:1.



Figure 3-14: Allied Motion HT05001 torque motor, peak torque: 23.2 N · m, shown here with components of the front leg.

Shoulder Unit

The shoulder unit forms the enclosure for the actuators, gearboxes and encoders of each leg and provides a structural mounting interface to the body (cf. Figure 3-15 and 3-16). The unit rests atop the humerus and actuates the radius via a steel linkage (the tricep). Functionally, the shoulder may be decomposed into two sections, the first of these resides on the medial half of the enclosure and actuates the shoulder joint (cf. Figure 3-17). This is accomplished by connecting the rotor of the shoulder motor to both the humerus and the stator of the elbow motor. The second section lies on the lateral half of the unit and actuates the tricep, which is attached to the output of the gearbox (cf. Figure 3-18). Because the stator of the elbow motor is driven with the motion of the shoulder, immobilization of this actuator results in no rotation of the elbow joint.



Figure 3-15: The shoulder unit of the front leg encloses both actuators, gearboxes and sensors.

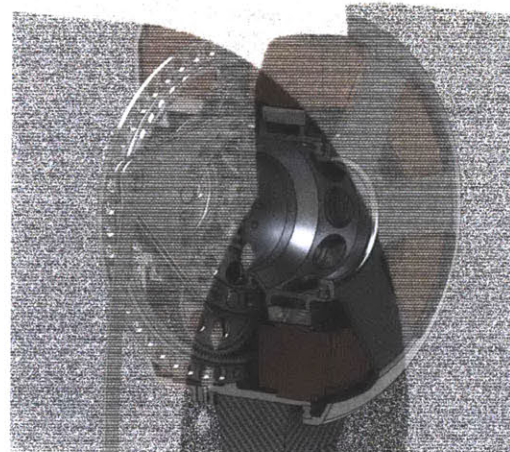


Figure 3-16: Partial section view of the shoulder unit of the front leg viewed from behind, the steel tendon actuates the elbow joint.

The elbow motor stage is accompanied by a planetary gear reduction. A planetary gearbox, incorporated into the housing, was selected for its favorable strength, weight, size and shape. The gearbox has a minimal impact on the overall dimensions of the shoulder unit, increasing the width by approximately 1 cm. The gears, owing to their large teeth, have a high maximum load and the planetary structure allows the motor to be driven from the output with only a small increase in passive impedance. Some gear reduction technologies,

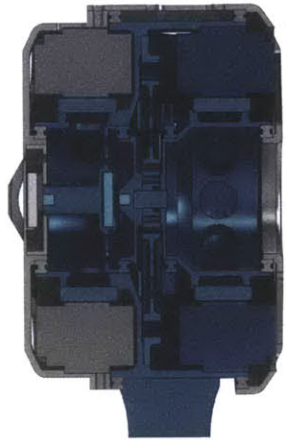


Figure 3-17: The shoulder motor rotates both the humerus and the stator of the elbow motor. Components that move when the shoulder motor is actuated are highlighted in blue.

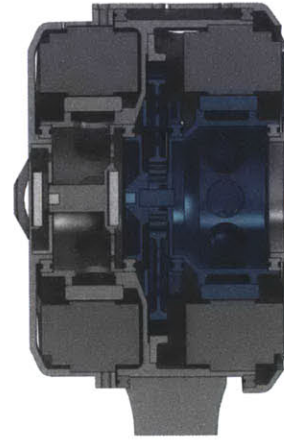


Figure 3-18: The elbow motor actuates the tricep, a steel linkage that is connected to a protrusion of the radius behind the elbow joint. Components that move when the elbow motor is actuated are highlighted in blue.

particularly harmonic drive, do not have this capability and thus are unsuitable for the low passive impedance demands of this project.

Gear sizing was approached from two perspectives, first the gears must be able to withstand the rather extreme loading of $120 \text{ N} \cdot \text{m}$ without excessive backlash and second, they must be suitably sized to minimize the total volume of the shoulder unit. Based on these considerations a gearbox with a tooth pitch of 48 teeth-per-inch (TPI) and ratio of 5.8:1 was designed (cf. Figure 3-19). The sun gear functions as the gearbox input with 40 teeth and is orbited by four planet gears each with 76 teeth. These planets mesh with a fixed internal ring gear with 192 teeth. The dimensions of the gearbox, exclusive of the planet carrier are 120.6 mm outside diameter by 6.6 mm axial length. Gear weight was substantially reduced by the removal of excess material (cf. Figure 3-20). This results in weight savings of approximately 50%, reducing the total weight from 562 g to 280 g and a reducing the reflected inertia of the gearbox from $1.8 \times 10^{-4} \text{ kg} \cdot \text{m}^2$ to $1.5 \times 10^{-4} \text{ kg} \cdot \text{m}^2$ (cf. Figure 3-21 and 3-22).

A critical element in ensuring the proper function of the gearbox and the shoulder unit as a whole is the bearings. Large diameter, thin cross section, ball bearings of angular and four point contact type are employed to support the rotors and gear hardware (cf. Figure 3-23).

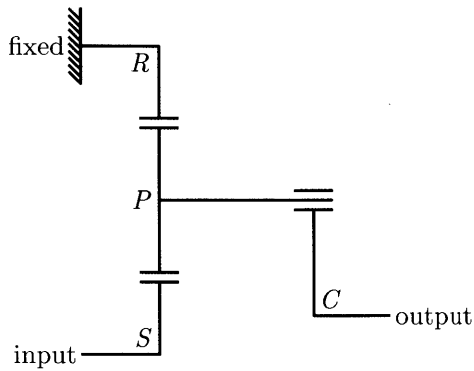


Figure 3-19: Schematic representation of the planetary gearbox design.

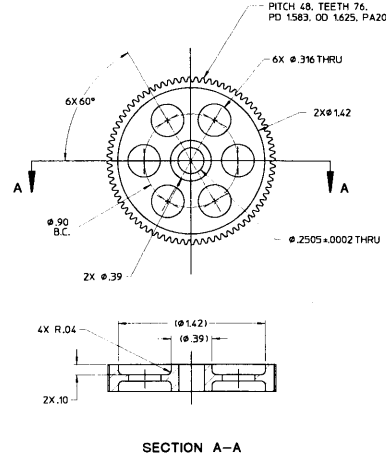


Figure 3-20: Portion of engineering drawing for low weight planet gear. The planets, along with the sun, ring and planet carrier were lightened extensively. Drawing dimensions are in inches.

Use of these bearings frees the internal cavity of the actuator unit for sensing and spreads loads over a larger number of ball bearings. The path of loading through the shoulder unit was designed to bypass the rotor-stator interface and utilizes the stators as reinforcing structural elements. Loads are transferred from the humerus to the two large bearings, these bearings are mounted directly to the outer housing.

The volume within the rotor of each motor is used for angular position sensing. Each motor is equipped with a RLS RMB20 absolute angular position encoder. The use of slip rings to transmit sensor information from the moving elbow encoder to the body is avoided by the clock spring winding of the encoder wiring. The RMB20 encoder was selected for its low mass and inertia, small size and unique mounting requirements. Unlike similar optical encoders the RMB20 magnetic encoder has a small diameter and the sensor is mounted on the axis of rotation.

Provisions for the introduction of abduction and adduction take the form of two bearing mounts on the posterior and anterior faces of the shoulder unit (cf. Figure 3-24). Together with a pull rod mount on the top surface of the shoulder unit. This degree of freedom is actuated by a Dynamixel EX-106+ servomotor.



Figure 3-21: Assembled view of the planet carrier and planet gears.

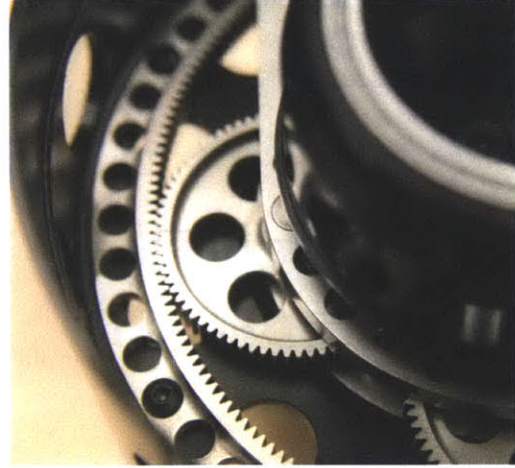


Figure 3-22: Closeup photo of the gearbox as assembled in the front leg.

Leg and Foot

The design of the front leg and foot is left flexible by the remote location of the actuators and associated precision structures. The remaining function of the leg is merely to transmit forces generated by ground contact to the body. Characteristics identified as desirable in a leg design are ease of manufacture, strength, durability and lightness. These design objectives were accomplished by employing manufacturing techniques and materials uncommon in legged robotics. Each leg link contains two distinct structures, a polyester foam core and a polyester resin shell forming a geometrically flexible structure that resembles a foam filled box beam (cf. Figure 3-25 and 3-26). Use of plastics in the place of more common leg materials such as aluminum or titanium allows legs to be manufactured quickly, cheaply and easily, with design iteration time approaching 24 h. This extremely short iteration time allows adaptive refinement of the leg geometry to an extent that is impractical with the standard three week turnaround of contracted machining.

The leg links are manufactured by machining two molds from Delrin stock. The molds are machined on a three axis computer numerical control (CNC) vertical milling station using basic tooling and techniques. The Delrin molds machine easily and release the cast polyester parts well. The first mold is machined slightly undersized of the final external link dimensions to form the foam core, varying in deviation by 1.5 mm to 3.0 mm depending on

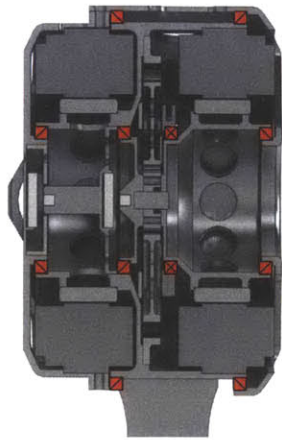


Figure 3-23: Placement and orientation of the bearings in front leg.



Figure 3-24: Ad/abduction mount on the shoulder unit permits rotation about an axis parallel to the spine shown here as a red line.

the anticipated loading in a particular region of the leg link. The second mold is machined at the nominal external dimensions. The foam core is cast first and transferred to the second mold after curing, where the shell material is cast around the core insert. The shell mold is filled in a vacuum chamber and cured at the elevated pressure of approximately 420 kPa gauge to inhibit the formation of voids.

The introduction of a Kevlar tendon and passive foot reduce the bending load on the radius by converting a portion of the load moment to tension of the tendon and compression in the leg link (cf. Figure 3-27). The tendon is a length of Kevlar webbing, anchored at one end to the tricep using a ladder lock mechanism while the other end is embedded into the foot. A compressive load on the foot, such as that due to ground contact, places the tendon in tension and reduces the peak stress within the radius. The foot itself is a simple link, with a silicone rubber pad. The foot reduces the passive impedance of the leg during impact and provides the anchor necessary for the use of a tendon.



Figure 3-25: Front leg links assembled to the housing.

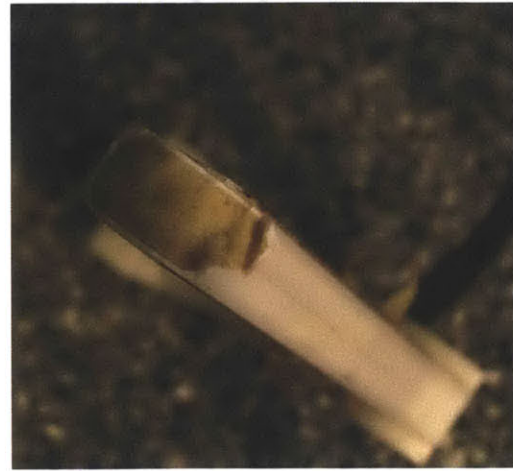


Figure 3-26: Internal structure of a foam composite leg link that was broken during single leg testing. The yellow material is the lightweight foam core and the white material is the plastic shell.



Figure 3-27: Kevlar tendon of the front leg, shown here during assembly of the foot pad. The tendon is connected to the tricep pin at the posterior end of the radius, from there it partially wraps the wrist joint and is embedded into the foot.

3.3.2 Rear Leg

The rear leg design inherits many features of the front leg but retains a degree of uniqueness. The most apparent of these differences is a three member leg structure instead of the simpler two element leg of the front (cf. Figure 3-28 and 3-29). This modification was introduced to increase the maximum leg length, while reducing the moment arm of the knee. The leg has the following specifications (cf. Table 3.4).



Figure 3-28: Front view of right rear leg.



Figure 3-29: Rear view of right rear leg.

Actuator Selection

The design loads of the rear leg, being very similar to those of the front leg, did not require a substantially different actuator. Thus the same HT05001 was used in the rear leg to drive

Specification	Value
Max. load	1250 N
Shoulder torque (peak)	134 N · m
Knee torque (peak)	134 N · m
Shoulder range of motion	150°
Knee range of motion	85°
Max. leg length	500 mm
Min. leg length	232 mm
Weight	3.60 kg

Table 3.4: Rear leg design specifications

both the hip and the knee. This facilitates a degree of modularity in the leg design and eliminates the expense of developing multiple custom motor windings. The use of the same motor also facilitates the reuse of many components from the shoulder unit of the front leg, decreasing per unit production costs.

Hip Unit

The most substantial difference between the shoulder unit of the front legs and the hip unit of the rear legs is the introduction of a gear reduction to the first motor stage (cf. Figure 3-30). This stage drives the hip in the rear leg. The addition of a gear reduction increases the capacity of the rear leg to produce propulsive forces that require moment loading of the hip. The difference in width between the shoulder units with one gear reduction (front legs) and two gear reductions (rear legs) is less than 1 cm.

Although much of the basic structure remains the same in the hip unit, the newly introduced gear reduction complicates the sensing system for knee motion (cf. Figure 3-31). Two small bearings were added to support the motion of a shaft that provides the encoder reference position to the knee position sensor. The knee sensor wiring can no longer be exposed to the medial face of the unit and instead must exit on the lateral face. Bearing placement in the rear leg is similar to the front with the exception that one bearing is modified from an angular contact to a four point contact to support possible moment loads (cf. Figure 3-32).

Leg and Foot

The fabrication methods developed for the front leg are also utilized in producing rear leg links. The major difference between the front and rear leg structures is the introduction of coupling between the metatarsal link and the femur. This presents itself in the form of a four bar linkage that constrains the angle of the metatarsal link to an orientation parallel with the femur. This modification was introduced to reduce the moment arm of the knee actuator while increasing the maximum leg length.

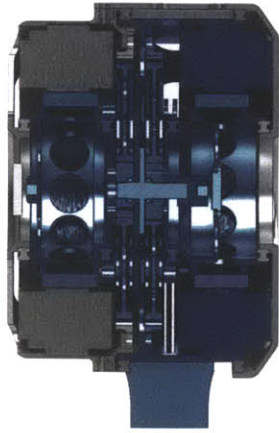


Figure 3-30: Gear reduction of the hip motor was introduced to increase hip torque of the rear leg. Elements that move when the hip motor is actuated are highlighted in blue.

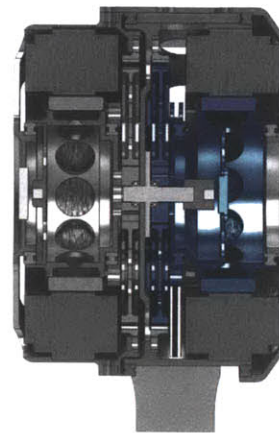


Figure 3-31: The knee motor actuates the knee through a steel tendon. Elements that move when the knee motor is actuated are highlighted in blue.

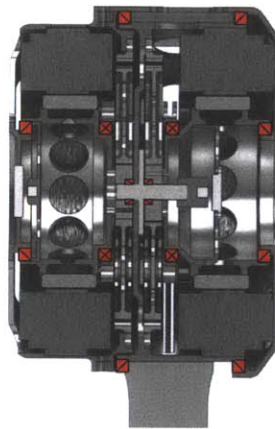


Figure 3-32: Bearing placement and orientation in the hip unit of the rear leg.

Chapter 4

Modeling and Performance

Estimation

4.1 Actuator Modeling

To understand the factors that contribute to motor heating, considered the most likely cause of actuator failure, a thermal model of the HT05001 was developed. Taking the thermal system as the volume containing motor windings heat is generated at the rate of $\dot{Q} = I^2 R$, as governed by Joule's First Law, where \dot{Q} is the thermal energy converted per unit time, I is the winding current and R is the winding resistance. This energy is either stored as a temperature increase of the motor windings or dissipated by conduction, convection or radiation. The thermal load is anticipated to be the greatest during high speed running, a task that is unlikely to continue for extended periods of time. Therefore, the thermal analysis of the HT05001 is focused on timescales on the order of minutes.

Motor loading conditions for a high speed rotary gallop are estimated based on footfall durations observed by Hildebrand for a cheetah running at approximately $72 \text{ km} \cdot \text{h}^{-1}$ [18]. Under these conditions each leg is in contact for 60 ms to 70 ms of a 390 ms stride. During contact the motor loading is assumed to resemble a half sine with a maximum value equal to the motor demagnetization current of 69.5 A (cf. Figure 4-1). This results in a root mean squared (RMS) motor current of 20.1 A over the entire stride and thus an average power dissipation of 318 W using the nominal winding resistance of 0.791Ω

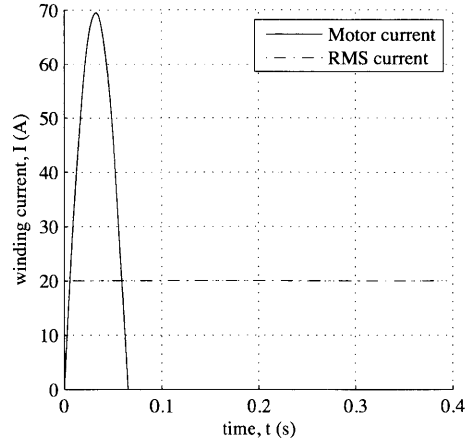


Figure 4-1: Anticipated motor current in a fast gallop.

To test the thermal characteristics of the windings under this type of loading the stator was placed upright on a thermally insulating surface in still air with an ambient temperature of 23.6 °C. The stator contains three windings connected in a wye configuration with an average terminal to terminal resistance of 0.791 Ω. One pair of terminals was connected to an Agilent 8757, 5.1 kW power supply, which was commanded to provide a constant power dissipation of 300 W. The current and voltage provided to the winding were simultaneously reported to LabView at 750 ms intervals. The winding temperature was determined by utilizing the well established relationship between the temperature and resistance of copper wire [12]. If the temperature coefficient of resistivity (α) is assumed to be constant over the temperature range of interest the relationship between winding temperature and resistance may be expressed as:

$$T = \frac{R - R_0}{\alpha R_0} + T_0 \quad (4.1)$$

where T and R are the instantaneous temperature and resistance of the winding and T_0 and R_0 are the temperature and resistance of the winding at a reference state, immediately prior to commencing the thermal test.

The 300 W test was run for 39 s resulting in an increase in temperature of 41.6 °C (cf. Figure 4-2). The maximum permissible winding temperature depends on the insulation class.

The F class winding insulation used in the HT05001 permits core temperatures up to 155 °C before motor life is compromised [61]. The character of the thermal response shows that despite the short timescales involved the effects of heat transfer from the windings is not negligible. Much of the heat transferred from the active winding is assumed to have been transferred by conduction to the inactive windings and the stator.

It was determined that a single time constant thermal model captures the thermal character of the motor to sufficient detail for short term operation. This model consists of a heat capacity (C) and a lumped dissipation factor (H) (cf. Figure 4-3). For such a system the governing differential equation and its solution are

$$C \frac{d\theta}{dt} = I^2 R - H\theta \quad (4.2)$$

$$\theta = \frac{I^2 R}{H} \left(1 - e^{-\frac{tH}{C}} \right), \quad (4.3)$$

where θ is the temperature rise above ambient ($T - T_0$). Fitting this model to the experimental data results in an estimated heat capacity of $170.7 \text{ J} \cdot \text{°C}^{-1}$ and a dissipation factor of $4.802 \text{ W} \cdot \text{°C}^{-1}$. Using the estimated dissipation of 318 W together with the empirical thermal model suggest that peak output running may be sustained for up to 5 min. This result represents an acceptable maximum effort stamina for an untethered machine.

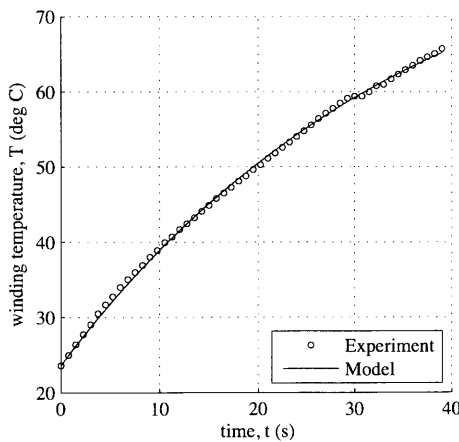


Figure 4-2: Experimental and model of winding temperature under constant 300 W thermal load.

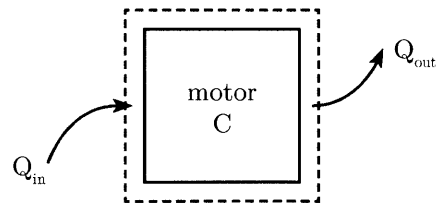


Figure 4-3: Thermal motor of the motor with heat generated by dissipation and rejected by conduction, convection and radiation.

4.2 Single Leg Dynamics

The first step in understanding the locomotion performance of a legged system is understanding how a single leg uses the ground to generate propulsive forces. This begins with the construction of a representative kinematic model. After a kinematic model of the leg is established, and thus the manner in which the leg may move is precisely defined, a system of leg dynamics is put in place to connect the forces and torques that are applied to the system with the motions that result. Once this dynamic framework is in place, what remains is exploration. In this analysis, studies of the effects of mean shoulder height, forward velocity and their relation to the force production capability of a front leg are presented. Following this, an analysis of leg return trajectories identifies characteristics typical of rapid protraction.

4.2.1 Mathematical Model

The kinematic model is based on the fundamental mechanical structure of the front leg and therefore contains only two components, the humerus and the radius (cf. Figure 4-4). The removal of the passive ankle joint eliminates joint redundancy and thereby simplifies both the kinematic and dynamic analysis. This simplification is not expected to alter the fundamental characteristics and responses of the leg during stance because the wrist reaches a state of maximum flexion shortly after impact and remains in this position until just before lift off. The effect of the foot on overall leg geometry is captured by incorporating it into the radius dimensions.

The system dynamics are obtained by the use of screw theory [59, 40]. Screw theory was selected because it facilitates the arbitrary extension of the dynamic solution to a general serial chain, composed of revolute and prismatic joints, and it provides the equations of motion in a format that is immediately compatible with numerical integration tools. The following text provides a brief introduction to the use of screw theory in two dimensions alongside the derivation of the dynamics of a general serial chain, the result of which is later used in the dynamic simulator. The notation and approach employed are based on the work of Zhao and Dai [68].

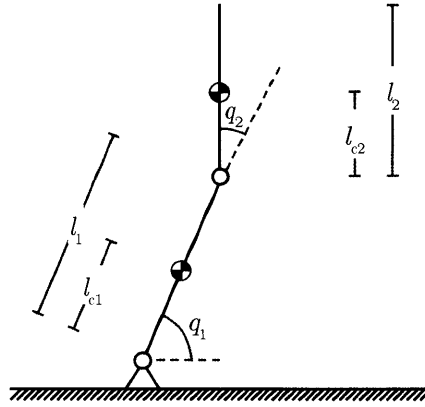


Figure 4-4: Kinematics of a two link serial chain.

The motion of a rigid body in two dimensions is expressed in screw theory as a *twist vector* (\mathbf{T}) with three components:

$$\mathbf{T} = \begin{bmatrix} \dot{x}_o & \dot{y}_o & \omega \end{bmatrix}^T \quad (4.4)$$

where \dot{x}_o and \dot{y}_o are the Cartesian velocity of an imaginary point within the body that is instantaneously coincident with the origin and ω is the angular velocity. The twist vector is related to the generalized coordinate (q) by a *unit twist*, written \mathcal{S} , such that:

$$\mathbf{T} = \mathcal{S}\dot{q} \quad (4.5)$$

where \dot{q} is the time derivative of the generalized coordinate. For a revolute joint located at the Cartesian coordinates (x_r, y_r) it may be shown that the unit twist is $\mathcal{S}_r = [y_r \ -x_r \ 1]^T$.

While the unit twist for a prismatic joint inclined at an angle ϕ from the horizontal is $\mathcal{S}_p = [\cos \phi \ \sin \phi \ 0]^T$ (cf. Figure 4-5).

To extend this analysis to a system of rigid bodies consider a serial chain composed of n links joined by revolute joints (cf. Figure 4-6). If the generalized coordinates are combined into a generalized coordinate vector such that $\mathbf{q} = [q_1 \ q_2 \ \dots \ q_n]^T$ the twist of link k may be

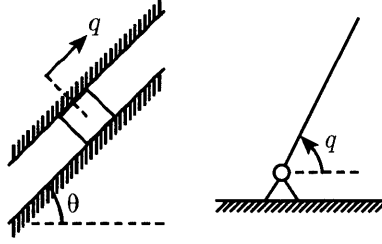


Figure 4-5: Revolute and prismatic joints in screw theory.

written as:

$$\mathbf{T}_k = \begin{bmatrix} \dot{x}_{ok} \\ \dot{y}_{ok} \\ \omega_k \end{bmatrix} = \begin{bmatrix} \mathcal{S}_1 & \mathcal{S}_2 & \dots & \mathcal{S}_n \end{bmatrix} \dot{\mathbf{q}} = \mathbf{J}\dot{\mathbf{q}} \quad (4.6)$$

where \mathbf{J} is a Jacobian matrix formed from the unit twists of each joint. This solution allows the twist of each link to be determined based on the unit twists and time derivative of generalized coordinates. However, because the twist provides the velocity of an imaginary point within the body that is coincident with the origin the usefulness of the result in this form is somewhat limited. To cast this result into a more intuitive form a coordinate transformation is used to transform the twist to the velocity of the center of mass of each link. Letting (x_{ck}, y_{ck}) be the Cartesian coordinates of the center of mass of link k the coordinate transformation matrix ($\mathbf{\Gamma}_k$) that converts the twist to a center of mass velocity (\mathbf{v}_k) is:

$$\mathbf{\Gamma}_k = \begin{bmatrix} 1 & 0 & -y_{ck} \\ 0 & 1 & x_{ck} \\ 0 & 0 & 1 \end{bmatrix} \quad (4.7)$$

and thus the center of mass velocity may be written directly as

$$\mathbf{v}_k = \mathbf{\Gamma}_k \mathbf{T}_k = \mathbf{\Gamma}_k \mathbf{J} \dot{\mathbf{q}}. \quad (4.8)$$

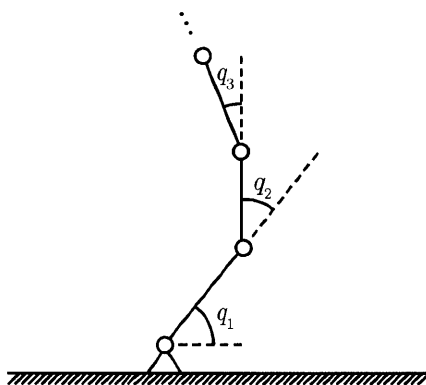


Figure 4-6: n -link kinematic chain.

At this point it is convenient to define the first order influence coefficient matrix for link k as

$$\mathbf{G}_k \equiv \mathbf{\Gamma}_k \mathbf{J}. \quad (4.9)$$

The first order influence coefficient matrix is an $n \times n$ matrix that relates the generalized coordinates to center of mass velocities such that

$$\mathbf{v}_k = \mathbf{G}_k \dot{\mathbf{q}}. \quad (4.10)$$

Differentiating \mathbf{v}_k to get the acceleration of link k

$$\mathbf{a}_k = \frac{d}{dt} \mathbf{v}_k = \frac{d}{dt} (\mathbf{G}_k \dot{\mathbf{q}}) = \mathbf{G}_k \ddot{\mathbf{q}} + \dot{\mathbf{G}}_k \dot{\mathbf{q}} \quad (4.11)$$

it becomes apparent that in order to find the acceleration of a link the time derivative of the first order influence coefficient matrix must be computed. Expanding the total derivative and converting the result to an equivalent matrix multiplication shows that the time

derivative may be separated into two components.

$$\dot{\mathbf{G}}_k = \frac{\partial \mathbf{G}_k}{\partial q_1} \frac{dq_1}{dt} + \frac{\partial \mathbf{G}_k}{\partial q_2} \frac{dq_2}{dt} + \dots + \frac{\partial \mathbf{G}_k}{\partial q_n} \frac{dq_n}{dt} \quad (4.12)$$

$$\dot{\mathbf{G}}_k = \begin{bmatrix} \dot{q}_1 & \dot{q}_2 & \dots & \dot{q}_n \end{bmatrix} \begin{bmatrix} \frac{\partial \mathbf{G}_k}{\partial q_1} \\ \frac{\partial \mathbf{G}_k}{\partial q_2} \\ \vdots \\ \frac{\partial \mathbf{G}_k}{\partial q_n} \end{bmatrix} = \dot{\mathbf{q}}^\top \mathbf{G}_k^* \quad (4.13)$$

The first component, $\dot{\mathbf{q}}^\top$, is the transpose of the generalized velocities and \mathbf{G}_k^* is a block matrix of the partial derivatives of \mathbf{G}_k with respect to the generalized coordinates. Defining column i of \mathbf{G}_k as the column vector \mathbf{g}_{ki} , the second order influence coefficient matrix (\mathbf{G}_k^*) may be equivalently defined as

$$\mathbf{G}_k^* \equiv \begin{bmatrix} \frac{\partial \mathbf{g}_{k1}}{\partial q_1} & \frac{\partial \mathbf{g}_{k2}}{\partial q_1} & \dots & \frac{\partial \mathbf{g}_{kn}}{\partial q_1} \\ \frac{\partial \mathbf{g}_{k1}}{\partial q_2} & \frac{\partial \mathbf{g}_{k2}}{\partial q_2} & \dots & \frac{\partial \mathbf{g}_{kn}}{\partial q_2} \\ \vdots & \vdots & \ddots & \vdots \\ \frac{\partial \mathbf{g}_{k1}}{\partial q_n} & \frac{\partial \mathbf{g}_{k2}}{\partial q_n} & \dots & \frac{\partial \mathbf{g}_{kn}}{\partial q_n} \end{bmatrix}. \quad (4.14)$$

Using this definition the acceleration of the center of gravity of link k may be expressed as

$$\mathbf{a}_k = \mathbf{G}_k \ddot{\mathbf{q}} + \dot{\mathbf{q}}^\top \mathbf{G}_k^* \dot{\mathbf{q}}. \quad (4.15)$$

Proceeding from this point using the Newton-Euler formulation of rigid body dynamics the inertial force of each link ($\mathbf{F}_k^r = [F_{xk}^r \ F_{yk}^r \ \tau_{ck}^r]^\top$) may be written in terms of the diagonal inertia matrix (\mathbf{N}_k) and the center of gravity acceleration as

$$\mathbf{F}_k^r = - \begin{bmatrix} m_k & 0 & 0 \\ 0 & m_k & 0 \\ 0 & 0 & I_k \end{bmatrix} \mathbf{a}_k = -\mathbf{N}_k \mathbf{a}_k \quad (4.16)$$

where m_k and I_k are the mass and inertia of link k about its center of mass. This inertial force on link k creates torques on the generalized coordinates equivalent to

$$\boldsymbol{\tau}_k^r = \begin{bmatrix} \tau_{k1}^r & \tau_{k2}^r & \cdots & \tau_{kn}^r \end{bmatrix} = \mathbf{G}_k^\top \mathbf{F}_k^r \quad (4.17)$$

where $\tau_{ki}^r = 0$ for links after k in the serial chain ($k + 1, k + 2, \dots, n$) by virtual work. Substituting \mathbf{F}_k^r from (4.16) and \mathbf{a}_k from (4.11) into (4.17) yields

$$\boldsymbol{\tau}_k^r = \mathbf{G}_k^\top \mathbf{F}_k^r = \mathbf{G}_k^\top (-\mathbf{N}_k \mathbf{a}_k) = -\mathbf{G}_k^\top \mathbf{N}_k (\mathbf{G}_k \ddot{\mathbf{q}} + \dot{\mathbf{G}}_k \dot{\mathbf{q}}) \quad (4.18)$$

$$\boldsymbol{\tau}_k^r = -(\mathbf{G}_k^\top \mathbf{N}_k \mathbf{G}_k \ddot{\mathbf{q}} + \mathbf{G}_k^\top \mathbf{N}_k \dot{\mathbf{G}}_k \dot{\mathbf{q}}). \quad (4.19)$$

This form of the equation is simplified by defining a conjugated form of the inertia matrix

$$\mathbf{M}_k \equiv \mathbf{G}_k^\top \mathbf{N}_k \mathbf{G}_k, \quad (4.20)$$

and using the definition of \mathbf{G}_k^* to rewrite the coefficient of the second term as

$$\mathbf{G}_k^\top \mathbf{N}_k \dot{\mathbf{G}}_k = \mathbf{G}_k^\top \mathbf{N}_k \frac{\partial \mathbf{G}_k}{\partial q_1} \frac{dq_1}{dt} + \mathbf{G}_k^\top \mathbf{N}_k \frac{\partial \mathbf{G}_k}{\partial q_2} \frac{dq_2}{dt} + \cdots + \mathbf{G}_k^\top \mathbf{N}_k \frac{\partial \mathbf{G}_k}{\partial q_n} \frac{dq_n}{dt} \quad (4.21)$$

$$= \begin{bmatrix} \dot{q}_1 & \dot{q}_2 & \cdots & \dot{q}_n \end{bmatrix} \begin{bmatrix} \mathbf{G}_k^\top \mathbf{N}_k \frac{\partial \mathbf{G}_k}{\partial q_1} \\ \mathbf{G}_k^\top \mathbf{N}_k \frac{\partial \mathbf{G}_k}{\partial q_2} \\ \vdots \\ \mathbf{G}_k^\top \mathbf{N}_k \frac{\partial \mathbf{G}_k}{\partial q_n} \end{bmatrix} \quad (4.22)$$

$$= \dot{\mathbf{q}}^\top \begin{bmatrix} \mathbf{G}_k^\top \mathbf{N}_k \frac{\partial \mathbf{g}_{k1}}{\partial q_1} & \mathbf{G}_k^\top \mathbf{N}_k \frac{\partial \mathbf{g}_{k2}}{\partial q_1} & \cdots & \mathbf{G}_k^\top \mathbf{N}_k \frac{\partial \mathbf{g}_{kn}}{\partial q_1} \\ \mathbf{G}_k^\top \mathbf{N}_k \frac{\partial \mathbf{g}_{k1}}{\partial q_2} & \mathbf{G}_k^\top \mathbf{N}_k \frac{\partial \mathbf{g}_{k2}}{\partial q_2} & \cdots & \mathbf{G}_k^\top \mathbf{N}_k \frac{\partial \mathbf{g}_{kn}}{\partial q_2} \\ \vdots & \vdots & \ddots & \vdots \\ \mathbf{G}_k^\top \mathbf{N}_k \frac{\partial \mathbf{g}_{k1}}{\partial q_n} & \mathbf{G}_k^\top \mathbf{N}_k \frac{\partial \mathbf{g}_{k2}}{\partial q_n} & \cdots & \mathbf{G}_k^\top \mathbf{N}_k \frac{\partial \mathbf{g}_{kn}}{\partial q_n} \end{bmatrix} \quad (4.23)$$

$$= \dot{\mathbf{q}}^\top ((\mathbf{G}_k^\top \mathbf{N}_k) \otimes \mathbf{G}_k^*) \quad (4.24)$$

where \otimes is used to denote the Kronecker product of two matrices. This equation may be

simplified further by defining

$$\mathbf{H}_k \equiv (\mathbf{G}_k^\top \mathbf{N}_k) \otimes \mathbf{G}_k^*. \quad (4.25)$$

Summing the inertial contributions of all links of the serial chain the total inertia torque vector is

$$\boldsymbol{\tau}^r = \sum_{k=1}^n \boldsymbol{\tau}_k^r = -(\mathbf{M}\ddot{\mathbf{q}} + \dot{\mathbf{q}}^\top \mathbf{H}\dot{\mathbf{q}}) \quad (4.26)$$

where

$$\mathbf{M} = \sum_{k=1}^n \mathbf{M}_k = \sum_{k=1}^n (\mathbf{G}_k^\top \mathbf{N}_k \mathbf{G}_k) \quad (4.27)$$

and

$$\mathbf{H} = \sum_{k=1}^n \mathbf{H}_k = \sum_{k=1}^n ((\mathbf{G}_k^\top \mathbf{N}_k) \otimes \mathbf{G}_k^*). \quad (4.28)$$

Expressing the dynamic model in equilibrium form the joint torques due to inertia must balance those due to gravity, external forces and actuators, thus

$$\boldsymbol{\tau}^r + \boldsymbol{\tau}^g + \boldsymbol{\tau}^e + \boldsymbol{\tau}^a = \mathbf{0}, \quad (4.29)$$

where $\boldsymbol{\tau}^g$ is the joint torques induced by gravity, $\boldsymbol{\tau}^e$ is the joint torques induced by external forces and $\boldsymbol{\tau}^a$ is the torques applied by joint actuators. Using the first order influence coefficient matrix the torques due to gravity and external forces may be expressed as

$$\boldsymbol{\tau}^g + \boldsymbol{\tau}^e = \sum_{k=1}^n (\mathbf{G}_k^\top (\mathbf{F}_k^g + \mathbf{F}_k^e)), \quad (4.30)$$

where \mathbf{F}_k^g is the force on the center of gravity of link k due to gravity and \mathbf{F}_k^e is the external forces and torques applied at the center of gravity of link k . For a system in which gravity acts in the negative y direction the force of gravity on link k is $\mathbf{F}_k^g = m_k \mathbf{g} = m_k [0 \ -g \ 0]^\top$, where g is the gravitational acceleration. Combining these torque terms the equations of motion for the serial chain may be written as

$$\mathbf{M}\ddot{\mathbf{q}} + \dot{\mathbf{q}}^\top \mathbf{H}\dot{\mathbf{q}} - \sum_{k=1}^n (\mathbf{G}_k^\top (\mathbf{F}_k^g + \mathbf{F}_k^e)) - \boldsymbol{\tau}^a = \mathbf{0}. \quad (4.31)$$

Or by taking the inverse of \mathbf{M} and arranging for $\ddot{\mathbf{q}}$ as

$$\ddot{\mathbf{q}} = \mathbf{M}^{-1} \left(\tau^a + \sum_{k=1}^n (\mathbf{G}_k^T (\mathbf{F}_k^g + \mathbf{F}_k^e)) - \dot{\mathbf{q}}^T \mathbf{H} \dot{\mathbf{q}} \right). \quad (4.32)$$

For the two link model used to study the contact phase of leg operation \mathbf{G}_1 and \mathbf{G}_2 may be assembled in the following fashion. First, in cases where $i \leq k$ the i th column of \mathbf{G}_k may be written as

$$\mathbf{g}_{ki} = \begin{bmatrix} y_{ri} - y_{ck} \\ -x_{ri} + x_{ck} \\ 1 \end{bmatrix}$$

where the position of the revolute joint for link i has the Cartesian position (x_{ri}, y_{ri}) . Then, for columns where $i > k$ the column vector is equivalent to the null vector, $\mathbf{g}_{ki} = \mathbf{0}$. Thus \mathbf{G}_1 and \mathbf{G}_2 for the given geometry (cf. Figure 4-7) are

$$\mathbf{G}_1 = \begin{bmatrix} y_{r1} - y_{c1} & 0 \\ -x_{r1} + x_{c1} & 0 \\ 1 & 0 \end{bmatrix} = \begin{bmatrix} -l_{c1} \sin q_1 & 0 \\ l_{c1} \cos q_1 & 0 \\ 1 & 0 \end{bmatrix} \quad (4.33)$$

$$\mathbf{G}_2 = \begin{bmatrix} y_{r1} - y_{c2} & y_{r2} - y_{c2} \\ -x_{r1} + x_{c2} & -x_{r2} + x_{c2} \\ 1 & 1 \end{bmatrix} \quad (4.34)$$

$$= \begin{bmatrix} -l_1 \sin q_1 - l_{c2} \sin(q_1 + q_2) & -l_{c2} \sin(q_1 + q_2) \\ l_1 \cos q_1 + l_{c2} \cos(q_1 + q_2) & l_{c2} \cos(q_1 + q_2) \\ 1 & 1 \end{bmatrix}. \quad (4.35)$$

These definitions of \mathbf{G}_k along with the inertia matrix of each link completely describe the serial chain. From them the additional chain parameters, \mathbf{M} and \mathbf{H} , may be calculated. If these parameters are combined with a configuration (\mathbf{q}), velocity ($\dot{\mathbf{q}}$) and loading, the acceleration of the generalized coordinates ($\ddot{\mathbf{q}}$) may be determined.

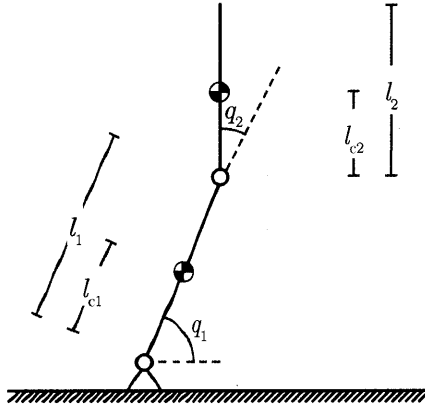


Figure 4-7: Definition of physical quantities for two link serial chain.

4.2.2 Stance Phase Simulation

The intent of the leg itself is to produce controllable forces on the body, that may be used for propulsion or maneuvering. Consequently, the intent of the single leg dynamic simulation is to determine the precise manner in which the leg must be employed to access its full capacity in this regard. Two variations in the character of a stride are studied: mean shoulder height and forward velocity. Each of these stride modifications alters the sense and magnitude of the body forces that may be generated throughout stance. Thus a thorough understanding of the stride is essential to achieving the highest force production.

The single leg dynamic simulation is implemented in MATLAB using objects. The parameters of each link in a serial chain are defined by creating n link objects, where n is the kinematic chain length. These links are then arranged into a single chain object. The chain object is passed to a preprocessor which derives the equations of motion by calculating the M , H , G_k and N_k matrices. After these matrices have been determined for a specific chain they are saved so that they need not be re-derived to perform dynamic calculations.

The structure of the dynamic simulation is unique in approach and somewhat resembles the moment method used in aerodynamics [34] and the Milliken moment method used in vehicle dynamics [43]. The shoulder trajectory and joint torques are specified as inputs and for each instant in time the resultant body force (F_{bx} , F_{by}) and ground reaction force (F_{gx} , F_{gy}) are calculated (cf. Figure 4-8). This approach allows the actuator torques to be

swept over their range while the leg is in a particular dynamic state, generating a region of accessible body forces at that instant (cf. Figure 4-9). The factors that directly limit these body forces are the maximum actuator torques and the limits of the contact interaction at the foot.

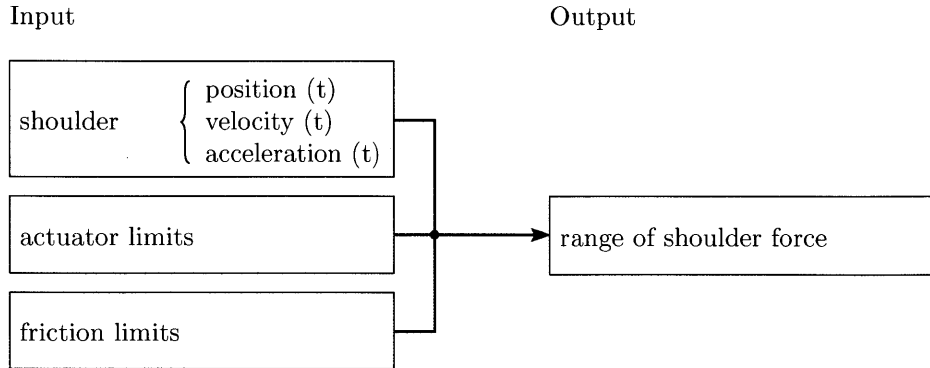


Figure 4-8: Program layout of the stance phase dynamic simulator.

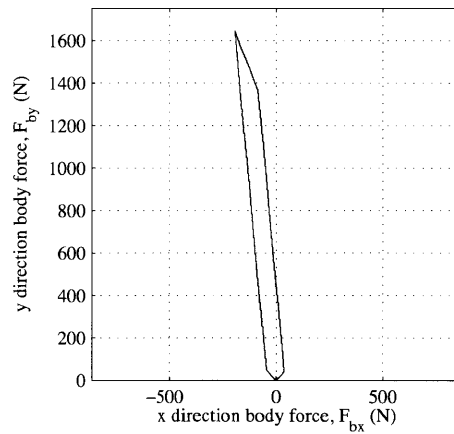


Figure 4-9: The range of accessible body forces in a specific configuration. Plotted in the F_{bx} - F_{by} plane.

In order to simplify the analysis and focus on the effect of shoulder height several simplifications to the shoulder trajectory are introduced. First, based on biological data, variation in shoulder height throughout the contact portion of a rotary gallop is small in comparison to changes in horizontal position [18]. Thus the shoulder trajectory is simplified to a

Property	Value
Humerus length	240 mm
Humerus mass	200 g
Humerus inertia	$9.7 \times 10^{-4} \text{ kg} \cdot \text{m}^2$
Shoulder drive inertia	$4.7 \times 10^{-3} \text{ kg} \cdot \text{m}^2$
Radius + foot length	320 mm
Radius + foot mass	180 g
Radius + foot inertia	$1.5 \times 10^{-3} \text{ kg} \cdot \text{m}^2$
Knee drive inertia	$9.9 \times 10^{-4} \text{ kg} \cdot \text{m}^2$

Table 4.1: Leg parameters used in dynamic model

straight horizontal line and the vertical velocity and acceleration of the shoulder are set to zero throughout. Furthermore the forward velocity of the shoulder does not vary substantially throughout stance, allowing the horizontal acceleration to be set to zero as well. Note that this horizontal trajectory *requires* rapid acceleration and deceleration of the elbow and shoulder joints even though the shoulder itself does not accelerate. The leg parameters used in the dynamic simulation are based on those of the physical hardware (cf. Table 4.1).

For a specified shoulder height the range of accessible horizontal positions of the shoulder is broken into fifty equally spaced configurations. The possible body forces for each of these configurations is computed and a contour plot in the F_{bx} - F_{by} plane is generated. The contours in this plot show the forces that the leg is capable of generating with contours of greater magnitude indicating that forces within this contour may be generated in a larger number of configurations.

The results of these simulations show that two characteristics of the forces available at the body change with shoulder height. First, a higher stride height reduces the range of angles through which the leg may sweep due to the limits of leg length. This causes the cone of available body forces to narrow as height increases (cf. Figure 4-10, 4-11, 4-12 and 4-13). Physically this implies that less deceleration and acceleration is possible. The second feature is related to the first in that if a higher shoulder height is selected the elbow is less bent throughout stance. This causes a increase in the forces that are generated along the leg direction (from the foot to the shoulder). A balanced stride height avoids excessive compression of the elbow to maximize forces along the leg and avoids over extension of the knee to

maximize the capacity of the leg to provide propulsive forces. For the simulated parameters a suitable stride height seems to be around 45 cm.

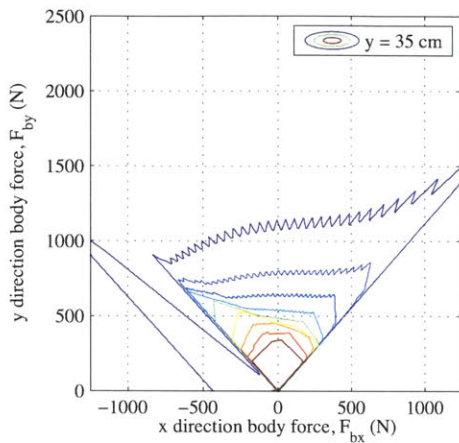


Figure 4-10: Possible body forces for strides with a shoulder height of $y = 35$ cm.

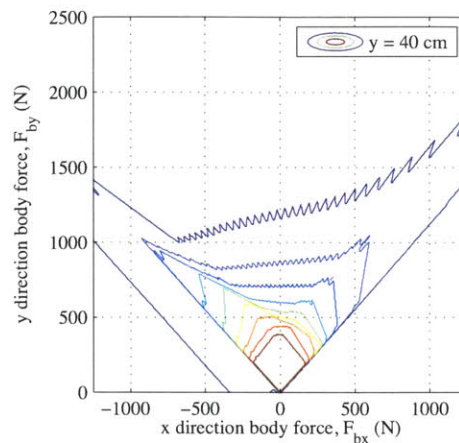


Figure 4-11: Possible body forces for strides with a shoulder height of $y = 40$ cm.

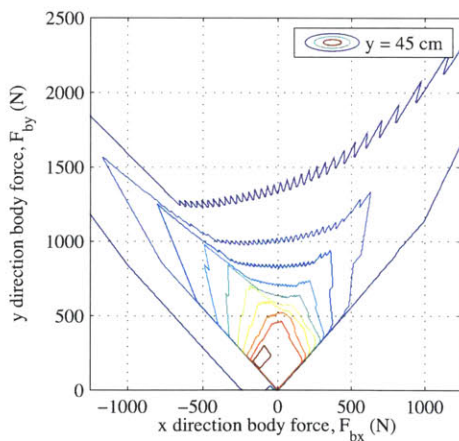


Figure 4-12: Possible body forces for strides with a shoulder height of $y = 45$ cm.

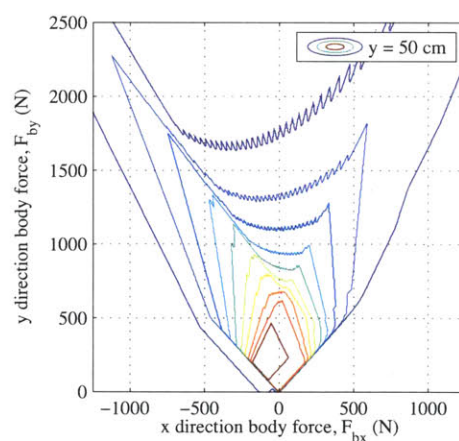


Figure 4-13: Possible body forces for strides with a shoulder height of $y = 50$ cm.

The forward velocity of the shoulder was then simulated for speeds of $2 \text{ m} \cdot \text{s}^{-1}$, $5 \text{ m} \cdot \text{s}^{-1}$, $10 \text{ m} \cdot \text{s}^{-1}$ and $15 \text{ m} \cdot \text{s}^{-1}$ at a shoulder height of 45 cm. The results of these simulations show that as speed is increased the body force production cone rotates about the origin away from the first quadrant and translates in the negative F_{bx} direction (cf. Figure 4-14, 4-15, 4-16 and 4-17). This implies that the capacity to produce propulsive forces is reduced. Furthermore

the boundary of the entire curve shrinks. This is due to the increasing amount of actuator torque that must be used to accelerate and decelerate the masses and inertias of the leg. The torque limits were set to the thermally limited torques for each joint, to achieve this the battery voltage must be high enough to overcome the back electromotive force (EMF) that would be present at this speed.

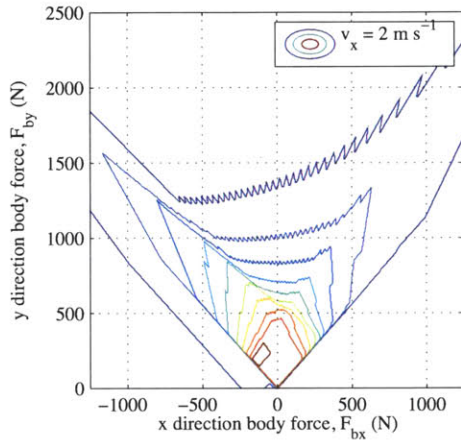


Figure 4-14: Possible body forces for strides with a forward velocity of $v_x = 2 \text{ m} \cdot \text{s}^{-1}$.

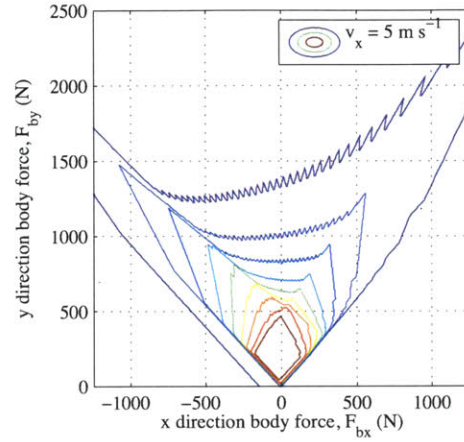


Figure 4-15: Possible body forces for strides with a forward velocity of $v_x = 5 \text{ m} \cdot \text{s}^{-1}$.

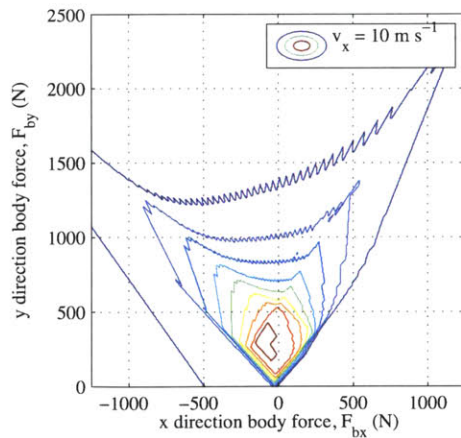


Figure 4-16: Possible body forces for strides with a forward velocity of $v_x = 10 \text{ m} \cdot \text{s}^{-1}$.

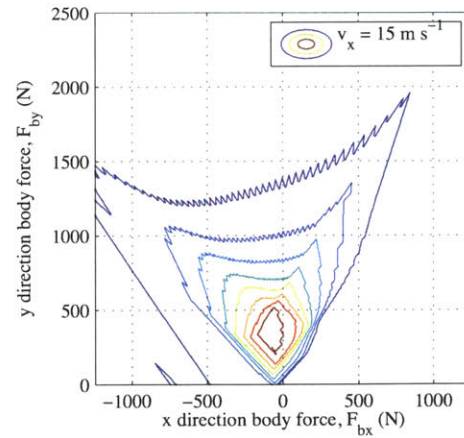


Figure 4-17: Possible body forces for strides with a forward velocity of $v_x = 15 \text{ m} \cdot \text{s}^{-1}$.

4.2.3 Protraction

Protraction is the movement of a limb from a rearward position to a forward position and is a required part of any gait. Depending on the leg and actuators, protraction may limit the maximum running speed. Thus it is essential to understand effective protraction strategies, specifically the joint trajectories and the torques that induce them. The framework for protraction simulation is somewhat different than the stance dynamic simulator and relies on different assumptions. In the protraction simulator the shoulder node is considered fixed (or at constant velocity) and the limb is protracted with no external loading at the foot (cf. Figure 4-18). This makes the simulation substantially faster and less complicated than the contact simulation. Shoulder reaction forces are calculated based on input shoulder and elbow torques but are assumed to have negligible effect on the motion of the body. The underlying equations of motion are identical to those derived for the stance simulation.

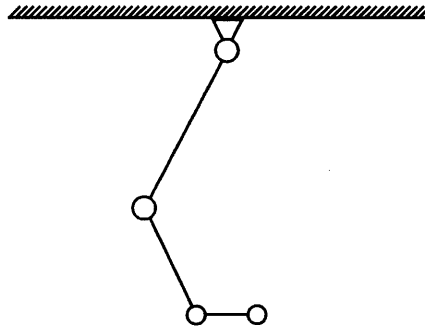


Figure 4-18: Three link leg with fixed shoulder node used to analyze protraction joint trajectories.

A optimization framework was built around this dynamic simulation to identify fast protraction torque profiles (and the joint angle profiles to which they correspond). This framework was implemented in MATLAB, and makes use of the `fmincon` function, a nonlinear optimization tool. The objective function was defined as $\text{obj} = t + w(\text{effort})$ where $w = 0.01$ is a weighting factor and effort is a measure of the actuator loading defined as

$$\text{effort} = \int_0^t \tau_k^2 + \tau_s^2 dt.$$

Thus the objective function depends on both time and actuator thermal load, as approximated by the total torque impulse. If a purely time optimized objective function was defined one would anticipate rail to rail actuator behavior. Because `fmincon` is a local optimization tool the optimizer was seeded randomly and the optimal results for many iterations were weighted and displayed simultaneously (cf. Figure 4-19 and 4-20).

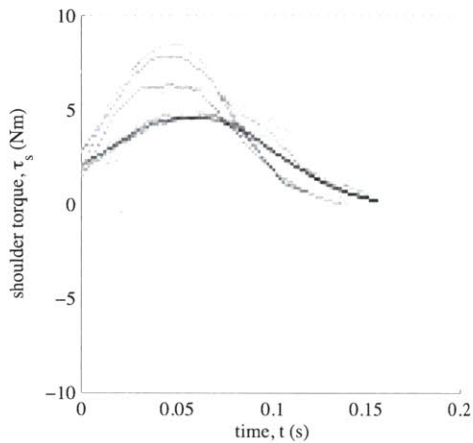


Figure 4-19: The shoulder torque that results from protraction optimization. The results of many randomly seeded optimizations are overlaid.

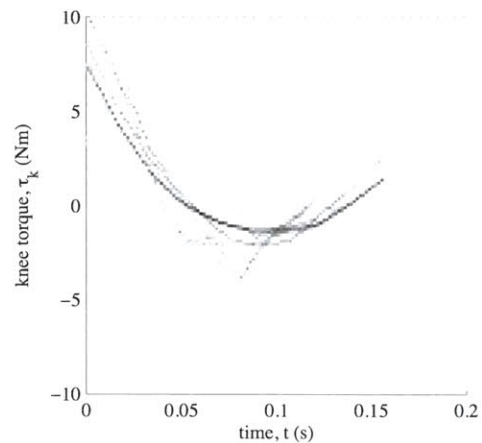


Figure 4-20: The knee torque that results from protraction optimization. The results of many randomly seeded optimizations are overlaid.

Typical joint angle profiles that result from this optimization have several interesting characteristics and bear a great resemblance to the trajectories observed in biological systems. First, for fast protraction the leg is collapsed before protraction begins (cf. Figure 4-21). This reduces the inertia as seen at the shoulder and allows the leg to protract more quickly within the actuator torque limits. A notable asymmetry is present in the torque profiles that is centered around the very small torques required to halt protraction of the limb in a forward position. This is a consequence of the natural dynamics of the kinematic chain. If the joints are allowed to run free the elbow extends, increasing the inertia and slowing rotation about the shoulder.

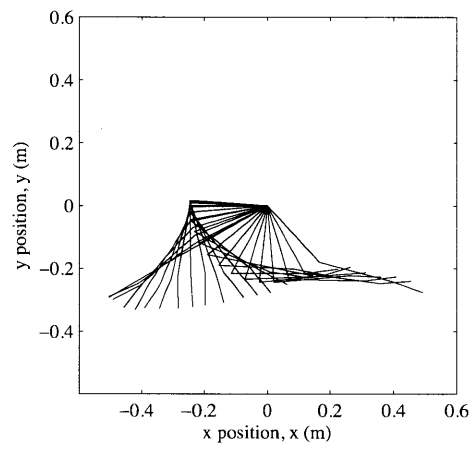


Figure 4-21: Movement of the leg through space when the protraction torques are commanded.

Chapter 5

Design Tools

5.1 Assessing Leg Capability with Force Maps

The force map is a design tool proposed to graphically illustrate how factors such as foot friction, actuator limits and leg geometry influence the shoulder force production capability of a particular leg design. It thus provides a quantitative metric for comparing and evaluating leg designs and building an intuitive understanding of how changes made to the leg alter the maximum forces that may be provided to the body.

Understanding the forces at the shoulder is a critical step in developing effective legged locomotion [54]. The body is often far more massive than the legs, particularly in systems designed for maneuverability and speed, and therefore the shoulder force becomes the vital coupling element between the propulsion system and the central hardware. In a familiar automotive system, the shoulder forces are analogous to the forces applied through the suspension to the chassis. In a car, interaction at this joint is typically rather straightforward, due to the decoupling of propulsive (tractive) forces and support (suspension) forces. However, in legged locomotion these two elements are inextricably linked.

Precise control of the forces generated at the shoulder allows the trajectory of the body through space to be prescribed. Abstracting the interface between the leg and the body allows the force production mechanism to be considered independently of the often complicated body dynamics. With a lightweight leg dynamic coupling between the body and the leg is weak and this separation of the locomotion task into low level (leg control) and high

level (body control) is possible. Separating the system in this way emphasizes the importance of achieving a specific net impulse over the course of a contact event.

During steady state locomotion the net vertical impulse on the body due to all legs must be equal and opposite to the impulse generated by the constant pull of gravity. Additionally, the net propulsive impulse must be equal to any impulse caused by drag over a full gait cycle. If these goals are not met the body will tend to change speed. Given these strict demands on net impulse over the stride it must be asked: what are the limits of shoulder force production? Certainly one of the limits is the configuration dependent static actuator limits (typically computed from the Jacobian). However, during dynamic locomotion these limits are altered by joint accelerations and the natural dynamics of the system. This effect is somewhat nonintuitive but it is perhaps the most significant interaction in defining the limits of ultimate running speed. As speed increases a larger increment of actuator torque is devoted to acceleration of leg links and therefore less torque is available for shoulder force production. Furthermore because maximum stride length is fixed by the leg geometry a higher forward velocity leaves less time for impulses to be generated, necessitating higher peak forces.

Another important limit to running speed is the contact interaction at the foot, specifically friction. If the standard Coulomb friction model is applied to the foot, it is clear that vertical loading must be increased in tandem with longitudinal loading to avoid sliding. This increased vertical force must be provided by the leg actuators. If the friction coefficient is less than one, increasing longitudinal forces at the foot requires not only the ability to apply these longitudinal forces but the ability to apply an increment in vertical force that is even larger than the desired change in longitudinal force.

To quantify the forces that may be produced by the leg the individual joint accelerations must first be identified, these depend heavily on the nature of the stride. Several trends seem to develop in the character of a running stride across various species and speeds. First, the shoulder trajectory relative to a fixed foot is generally a flat U shape (cf. Figure 5-1) [18]. This implies that shortly after touchdown the leg is primarily experiencing compression of the knee. Next, as the stride progresses, the dominant motion becomes rotation of the limb about the shoulder. After mid-stance the behavior of the leg changes once more to a knee

dominant posture, however in this case the knee is being extended. These three phases can be observed across many species and many gaits within an individual species. At high speed changes in the forward and vertical velocity of the shoulder are small in comparison to the average forward speed. The simplification employed when creating a force map is that the shoulder trajectory may be approximated as a horizontal line traversed at constant velocity. Thus the vertical and horizontal accelerations as well as the vertical velocity are zeroed. This condition, although simple, captures the majority of the joint accelerations induced by high speed running gaits.

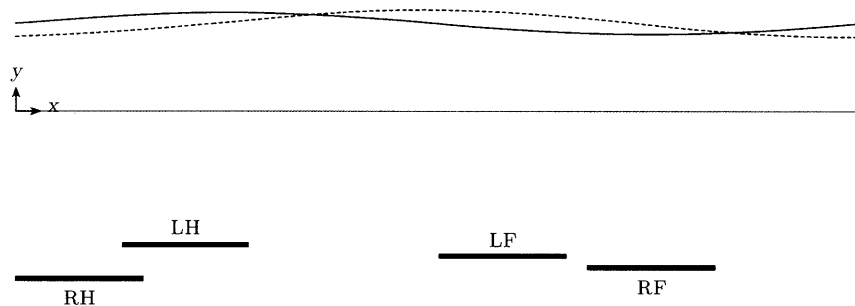


Figure 5-1: Approximate hip and shoulder trajectories for a running cheetah, adapted from data in [18].

The idea of a force map is to plot schematically the range of body forces (F_{bx} , F_{by}) that the leg is capable of generating at a specific forward velocity over the entire workspace. The workspace is generated by sweeping all possible joint angles with a fixed foot and mobile shoulder node (cf. Figure 5-2). The result of a force map is the velocity dependent *force production envelope*, or more simply the force envelope, which is the curve in the F_{bx} - F_{by} plane that encompasses all feasible body forces (cf. Figure 5-3). As the forward velocity, friction, actuator limits or leg geometry is modified the force production envelope changes size and shape.

Interpretation of the boundary of the force production envelope in terms of the body dynamics provides insight into the performance that can be expected when the leg is used during locomotion. For example the area enclosed by the curve to the right of the vertical line $F_{bx} = 0$ is populated by configurations and joint torques that result in propulsive forces being applied to the body. As this area decreases it becomes more difficult to

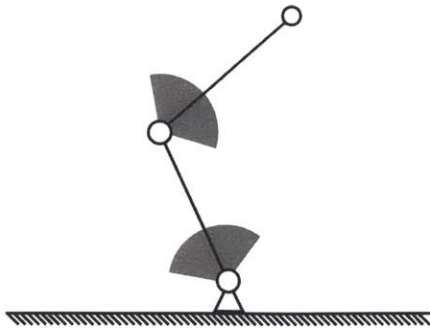


Figure 5-2: Workspace of the front leg with a fixed foot location.

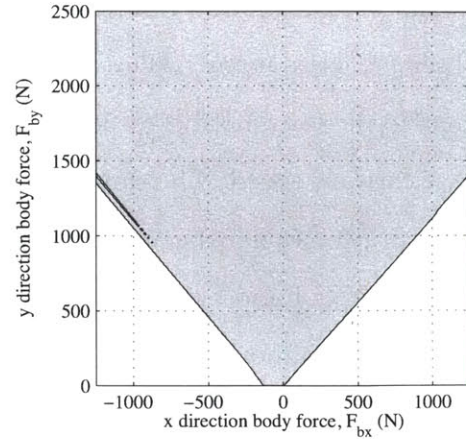


Figure 5-3: Force production envelope for a front leg with forward shoulder velocity $\dot{x} = 2 \text{ m} \cdot \text{s}^{-1}$

provide a substantial propulsive impulse, and thus it is more difficult to maintain speed. When this area vanishes altogether it becomes impossible to maintain the current velocity. This provides a rough estimate of the maximum running speed that is an overestimate because each stance phase is expected to contain periods of deceleration and acceleration even if the net propulsive impulse is zero. Similarly the limitations of vertical impulse generation may be estimated by taking the largest F_{by} intercept between the force envelope and $F_{bx} = 0$ and assuming that the leg generates a parabolic profile in vertical force and has a stance duration of t_s . This implies that the net vertical impulse is approximately given by
$$\Delta p = \int_0^{t_s} F_{by} dt \doteq \frac{2}{3} F_{by}|_{max} t_s.$$

The force map in the given form provides little context for how the forces are generated, and often the boundary is defined by operating near dynamic singularities. However, the force map may also be used to evaluate the relative ease or difficulty of obtaining a specific propulsive force by weighting each occurrence of a force during the sweep of the entire workspace for a given forward velocity (cf. Figure 5-4). This difficulty metric provides additional perspective into the ability of the leg to produce forces in multiple configurations. Flexibility in force production is useful in locomotion because it allows the control system to correct for disturbances or make sudden changes to the gait. If the leg is operating at its maximum potential for a given configuration it is difficult to apply the additional forces that may be necessary to correct for even the most minor disturbance, this decreases the

apparent performance of the device.

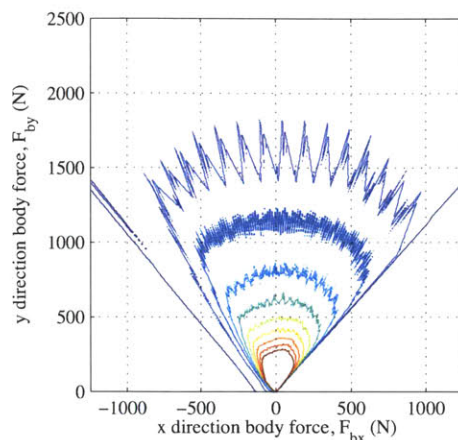


Figure 5-4: Weighted force production envelope for a front leg with forward shoulder velocity $\dot{x} = 2 \text{ m} \cdot \text{s}^{-1}$. As colors change from blue to red the number of configurations that allow forces within the contour to be generated increases.

It must be noted that the weighted force map provides no sense of continuity within a stride, and is therefore a first pass analysis tool that requires relatively little computational effort. This is to say that some of the forces that are theoretically possible may be difficult to achieve as part of a cohesive stride because they represent leg configurations that are separated by substantial differences in joint configuration. To remedy this deficiency and provide a more developed but intuitive way of understanding and constructing coherent strides the force map planning tool was developed.

5.2 Force Map Stride Planning

If the control of the body is approached by decoupling the leg from the body at the shoulder as proposed, the task of the body level controller is to generate a desired shoulder trajectory and a force profile that accompanies it. The job of the leg then is to match both of these requirements dynamically, most probably by implementing a type of impedance control [21]. Execution of this task is made more difficult by an additional decision that the leg level controller must make. Specifically, what configuration of the leg should be selected as the touchdown configuration (cf. Figure 5-5). This decision is difficult because the touchdown

configuration influences the subsequent evolution of the stride, and if the wrong configuration is selected the leg may not be capable of producing the desired forces. The inability of the leg to generate the desired shoulder forces may be brought about by several factors such as configuration or velocity dependence, exceeding the limits of friction at the foot or perhaps even lifting the foot off the ground.

Choosing an appropriate touchdown configuration also assures that adequate control authority remains to take up disturbances that may arise throughout the stride. As the locomotion speed increases the bounds of friction and the actuator limits move ever closer, closing the touchdown configuration window until ultimately the window is a single point and locomotion speed cannot be increased further (cf. Figure 5-6). If attaining high running speeds is the design goal this point, which depends on the shoulder trajectory and force profile, must be located with precision. However the target touchdown configuration may change throughout the speed range and also with changes in the desired force profile or shoulder trajectory.

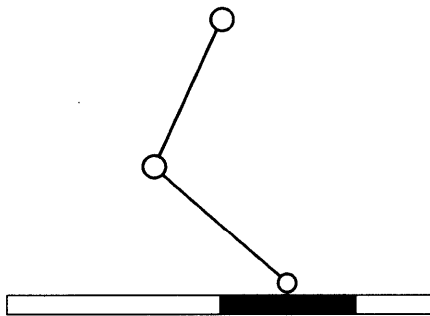


Figure 5-5: Acceptable touchdown configuration range, the foot may be placed within the shaded area.

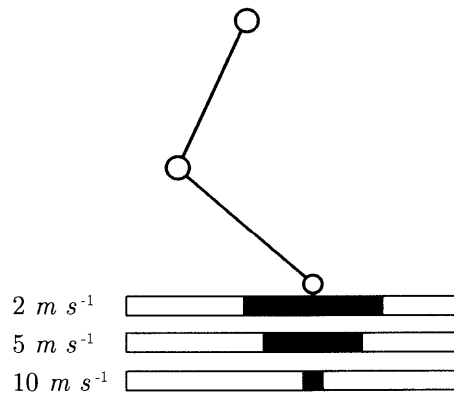


Figure 5-6: Schematic representation of how the range of acceptable touchdown configurations closes with increasing speed.

Variation of the ideal touchdown configurations with all of these parameters makes determining target configurations both difficult and essential. A brute force approach, in which the leg dynamics are solved directly, is difficult to implement due to the computational limits of embedded control hardware. Even if the shoulder trajectory and force profile are known,

there is still a large range of touchdown configurations, each of which must be simulated with the leg dynamics to develop the control torques. The friction interaction then must be evaluated at every instant throughout each of these strides to rule out trajectories that would cause the foot to slide. The following section addresses this problem in stride planning and develops an intuitive graphical method for evaluating the force production capabilities of a leg over a stride.

5.2.1 Selecting a Stride Primitive

The process of developing a stride planner begins with the selection of a representative shoulder trajectory through space. This trajectory often depends on gait and the characteristics and design of the body and leg. The model must capture the essence of the dynamic interaction between the leg and the body. Specifically this means that an identical force profile, if applied to the physical hardware must not produce a substantially different shoulder trajectory. The complexity of the model required to accomplish this varies with the leg and body design, in this case of a rotary gallop a straight line shoulder profile is a reasonable approximation. This is due to the fact that the majority of the joint accelerations arise from matching the shoulder forward velocity. The vertical velocity and changes in the horizontal velocity are small in comparison and thus contribute only a minor part to accelerations of the generalized coordinates.

One substantial advantage of selecting a straight line profile is that it makes it possible to decouple the selection of touchdown configuration from the remainder of the stride. That is to say that regardless of the precise touchdown configuration selected the shoulder remains on the same line through space. If the stride primitive were not linear different touchdown configurations would traverse different positions through space requiring a larger number of calculations (cf. Figure 5-7). However, a disadvantage of the straight line profile simplification is that it neglects the configuration dependence of the shoulder force that will exist with the additional compression of the leg that typically occurs in a real stride. This may lead the results to indicate that a stride is possible, when in actuality it falls just outside of the actuator capability.

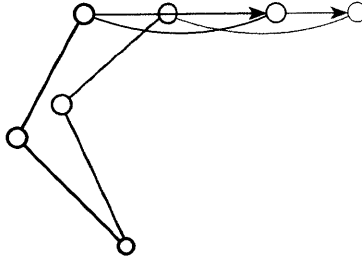


Figure 5-7: Straight as opposed to curved shoulder profiles permit the decoupling of touchdown configuration selection from stride torque calculation.

5.2.2 Calculating the Force Production Envelope

For a specific set of position, velocity and acceleration conditions of the shoulder it is possible to calculate the *state dependent force production envelope* or SDFE. This is the region of the F_{bx} - F_{by} plane that contains all body forces that the leg is capable of generating under the given conditions (cf. Figure 5-8). The limits of the forces that may be produced are defined by two factors, the actuator torque limits and the contact interaction at the foot. In the model that follows contact requires two conditions to be met. First, in order to ensure the foot remains fixed the forces at the foot must lie within the friction cone. Second, the vertical force at the foot must be in the positive direction, that is to say the foot may not pull on the ground.

All of these limitations are reflected in the characteristics of the SDFE and have physically significant, intuitive interpretations (cf. Figure 5-9). The lowest point on the F_y scale represents the shoulder force required to actuate the leg while maintaining zero contact force with the ground (\mathbf{F}_{zf}). For a well designed leg this force should always be near zero, meaning that only a small portion of the forces that occur at the shoulder are due to accelerations of the leg. If this body force is large, actuation of the leg will affect body dynamics, which will likely be undesirable. A massless leg will always place this point at the origin.

The cone that originates at \mathbf{F}_{zf} is the friction cone of the foot translated into shoulder force coordinates. If the friction coefficient (μ) is made larger the cone widens. For low

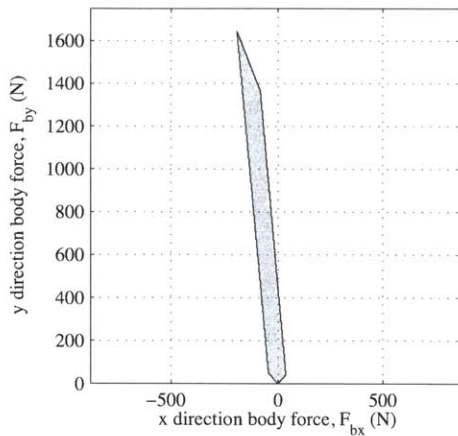


Figure 5-8: The state dependent force envelope shown here is the region of the F_{bx} - F_{by} plane that contains all possible body forces for a given leg state (position, velocity and acceleration).

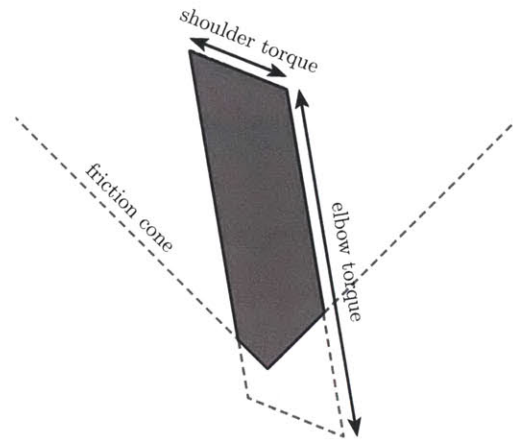


Figure 5-9: The bounds of the SDFE are formed by actuator limitations and the frictional interaction at the foot.

friction surfaces this cone may become quite narrow, possibly trimming all but one actuator bound. In such a situation the robot is said to be predominantly friction limited.

The final set of bounds is the parallelogram produced by symmetric actuator limits. This parallelogram is rarely rectangular, in such a case the actuators would completely decouple horizontal and vertical force production at the shoulder. Such a situation is the typical case for a wheeled vehicle, with the wheel torque producing a F_{bx} component and the suspension generating a F_{by} component. In the case of a legged system an increment in elbow torque will generally produce a force component along the vector from the foot to the shoulder. An increment in the shoulder torque on the other hand will produce a force at a configuration dependent angle to the leg direction.

Obtaining the points that parameterize the SDFE is not as complex as it initially appears, this is due largely to the fact that the conversion from joint torques to shoulder forces may be expressed as an affine transform. That is to say that for a single position, velocity and acceleration state the shoulder force is related to the actuator torques by a translation of the origin and a linear coordinate transformation. The physical interpretation of the origin translation is that it represents the actuator torque required to produce zero force at the shoulder (τ_{zs}) or conversely the force at the shoulder that produces the desired state with zero actuator torques (F_{za}).

To complete the remapping of the shoulder and knee torques ($\boldsymbol{\tau} = [\tau_k \ \tau_s]^\top$) to the body forces ($\mathbf{F}_b = [F_{bx} \ F_{by}]^\top$) four points in the F_{bx} - F_{by} plane must be identified. The first of these is \mathbf{F}_{zf} , the shoulder force that produces zero contact forces at the foot. When the leg is operating under the conditions imposed by \mathbf{F}_{zf} the actuators provide just enough torque to move the members of the leg such that the foot velocity matches precisely the ground velocity even though no contact loads are exchanged. Once this point is identified two lines may be drawn forming an upward opening friction cone. The slope of these lines are $\pm\mu^{-1}$, where μ is the friction coefficient. Body forces within the friction cone satisfy the contact conditions at the foot.

Next, two linearly independent actuator torque states must be selected in order to identify the coordinate transformation that, in conjunction with the origin shift given by \mathbf{F}_{za} , converts joint torques to body forces. The simplest selections are $\boldsymbol{\tau}_{10} = [1 \ 0]^\top$ and $\boldsymbol{\tau}_{01} = [0 \ 1]^\top$ these torques result in shoulder forces of $\mathbf{F}_{10} = [F_{10x} \ F_{10y}]^\top$ and $\mathbf{F}_{01} = [F_{01x} \ F_{01y}]^\top$ respectively. Using these values the affine transformation matrix may be defined as

$$\mathbf{T}_a = \begin{bmatrix} -F_{01x} + F_{zax} & -F_{10x} + F_{zax} & -F_{zsx} \\ -F_{01y} + F_{zay} & -F_{10y} + F_{zay} & -F_{zsy} \\ 0 & 0 & 1 \end{bmatrix} \quad (5.1)$$

where $\mathbf{F}_{za} = [F_{zax} \ F_{zay}]^\top$ is the shoulder force that produces the desired motion of the shoulder with zero actuator torques. Using this transformation matrix, body force may be calculated as

$$\begin{bmatrix} F_{bx} \\ F_{by} \\ 1 \end{bmatrix} = \mathbf{T}_a \begin{bmatrix} \tau_k \\ \tau_s \\ 1 \end{bmatrix}. \quad (5.2)$$

With the assistance of (5.2) construction of the actuator limit curves of the SDFE requires only matrix multiplication. After construction of the actuator parallelogram is complete the intersection of this area with the friction cone forms the total state dependent force envelope for the given conditions. Thus full parameterization of a single leg condition requires the

calculation of these points for torque transformation, one point for inertia compensation and the globally applicable knowledge of friction coefficient and the actuator limits. Tabulation of these four points over the workspace for a given forward velocity would then be sufficient to calculate the torque profile for an arbitrarily defined shoulder force and shoulder trajectory.

5.2.3 Selecting Touchdown Configuration

Calculation of the state dependent force envelope over the workspace can be used to rapidly determine a touchdown configuration that is capable of providing the desired forces to the body. This is done by evaluating whether or not the desired force remains within the SDFE throughout the stride. The mathematical formulation of this stride planning approach begins with the selection of a desired shoulder height by the body level controller. This leaves the horizontal positioning of the foot with respect to the body at the discretion of the leg level controller. For each possible location of the foot relative to the shoulder the controller calculates whether this position is capable of providing the initial force by evaluating whether the force falls within the SDFE of that position. After this initial calculation the set of acceptable touchdown configurations will be narrowed substantially. For each of these acceptable positions the shoulder trajectory relative displacement is added to the initial shoulder position and the evaluation of leg capability is performed again. If the leg is incapable of providing the force demanded, that trajectory is thrown out and the next time step is evaluated only for the remaining profiles. This approach quickly narrows the window of acceptable touchdown configurations.

As a way to visualize the results of these stride planning calculations the capability matrix (\mathbf{R}) is introduced. \mathbf{R} is a $p \times s$ matrix where p is the number of equally spaced positions on the horizontal line selected by the body level controller for which the SDFE has been calculated and s is the number of these positions required to match the desired stride length. Thus for a straight line trajectory each row represents a specific leg configuration and each column represents a given demanded force at that instant. For each case where the force falls within the SDFE a one is added to the corresponding position of \mathbf{R} , which initially zeroed. Thus to identify a feasible touchdown configuration a diagonal must be identified that contains all

ones. If many touchdown configurations are possible one method of identifying a desirable stride is by ranking the effort required on the part of the actuators. This can be done by defining

$$e = \frac{\tau_{s,max}^2 - \tau_s^2}{2\tau_{s,max}^2} + \frac{\tau_{k,max}^2 - \tau_k^2}{2\tau_{k,max}^2}$$

where $\tau_{s,max}$ and $\tau_{k,max}$ are the shoulder and knee maximum torques respectively. Thus for maximum effort $e = 0$ and for minimum effort $e = 1$. The diagonal of \mathbf{R} with the largest sum therefore represents the lowest thermal loading on the motor.

These calculations are capable of being performed in real time making their application on modestly powered embedded systems practicable. The majority of computational time will be spent evaluating whether or not a point in the $F_{bx}-F_{by}$ plane is within the capability envelope for a specific configuration. Luckily an algorithm can be developed for performing this calculation quickly. First the point must be transformed into torque coordinates, this requires six multiplications. Next the actuator limits can be checked. Because the limits are rectangular in torque space this is as simple as verifying that the point falls within the actuator limits. If the point is outside of these limits then there is no need to continue, the point is outside of the capability envelope. This eliminates the majority of points tested. If the point is within the torque limits ground contact can be tested by evaluating whether or not the point is above the zero foot force point. If this evaluation returns satisfactory results the friction criterion can be checked by ensuring that the inverse of the slope from \mathbf{F}_zf to the point in the $F_{bx}-F_{by}$ plane falls between $-\mu$ and μ . All of these calculations are relatively simple additive or multiplicative operations which can be computed rapidly.

5.2.4 Calculating Torque Profiles

Once trajectory planning has been completed the next step, calculating the torque profiles over the stride, has in-fact already been completed. This operation is the affine transform from the desired shoulder forces to actuator torques. If torque values were not saved during trajectory planning they may be recalculated for the selected touchdown configuration without considering that the torques may fall outside of the actuator limits. If computational resources permit, and additional accuracy is desired, the shoulder profile time step can be

refined and calculations performed once more to attain a smoother torque profile.

An alternative method of calculating the torques throughout the stride is available in systems with even larger computational power. The touchdown configuration, shoulder force and shoulder trajectory are all known, therefore the torques may be calculated from the inverse dynamics. This calculation is somewhat time consuming for embedded systems but provides absolute assurance that the commanded torques will provide the desired motions, with the provision that the dynamic model used is reasonably accurate. In this scenario the discretized profiles are used for stride planning while the inverse dynamics are used for precise actuator torque estimation.

Chapter 6

Testing and Design Iteration

Testing of the leg design is broken down into three phases. Design proofing, single leg testing, and multi leg testing. The first two of these phases were undertaken for the front leg design alone and the final phase entails simultaneous testing of all four legs. The testing program is ongoing and the control system is largely the work of Sang-ok Seok.

6.1 Design Proof

The first step in developing the leg further was testing the practicability of production methods, evaluating candidate materials and assessing the overall feasibility and performance of the platform. The design presented in Chapter 3 is the second iteration leg design. Sufficient changes were identified during the proof phase of the first iteration to warrant a partial redesign. Two major changes were introduced in this version. First, two large diameter split ring ball bearings were substituted for a Teflon impregnated bronze surface bearing. The friction torque introduced by the surface bearings, as well as the difficulty in achieving satisfactory alignment of the shoulder justified the additional expense of the ball bearings. Second, the abduction axis bearing mounts were introduced to the base of the shoulder and hip. These provisions were not considered on earlier designs. Many additional minor changes, such as reductions in motor width and the refinement of the sensor mounting interfaces were also introduced.

The design proofing of the second iteration front leg proceeded smoothly. Fit tolerances

were refined from experience with the first iteration fits making assembly relatively trouble free. Shoulder friction and alignment were improved substantially and the leg was deemed suitable for single leg testing.

6.2 Single Leg Testing

Single leg testing was executed to quantitatively assess the performance of the leg design before committing to the fabrication of multiple units. The apparatus developed to perform these tests is a unique variation on the standard linear slide (cf. Figure 6-1). The slide supports a body element, to which the front leg is attached. The body and leg are propelled to a velocity of approximately $2.5 \text{ m} \cdot \text{s}^{-1}$ by a falling weight. After maximum speed is reached the body falls from its supports until the leg impacts the ground and provides support forces. After the contact event the body is caught by rubber wheels. CG position, inertia, angular velocity and speed of the body are adjusted to mimic the behavior of an actual body during a rotary gallop.

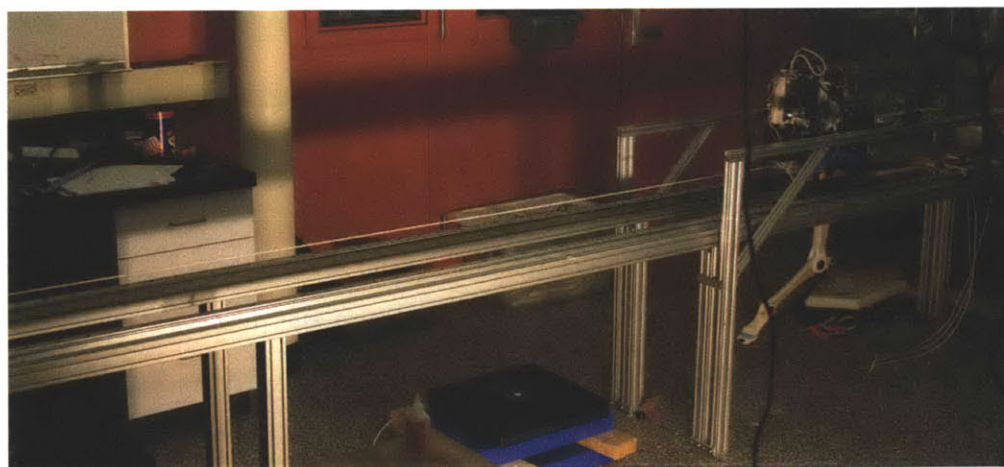


Figure 6-1: Single leg test apparatus consists of a linear slide with front leg attached to body emulator. The body and leg enter free fall before the leg touches down for a single contact event. Following contact the body is caught by two rubber wheels.

Initial testing of the front leg bears a remarkable resemblance to high speed footage of a running quadruped (cf. Figure 6-2 and 6-3). A 450 ms stance phase with peak vertical ground reaction forces of 550 N and peak propulsive force of 75 N was observed (cf. Figure

6-3). These results were obtained using a simple impedance controller. The front leg seemed to operate relatively close to the actuator limits of the shoulder so a third design iteration was proposed and is in development to add a gear reduction stage to the front leg, making it similar in form to the rear leg.



Figure 6-2: Still images from a high-speed video of single leg testing.

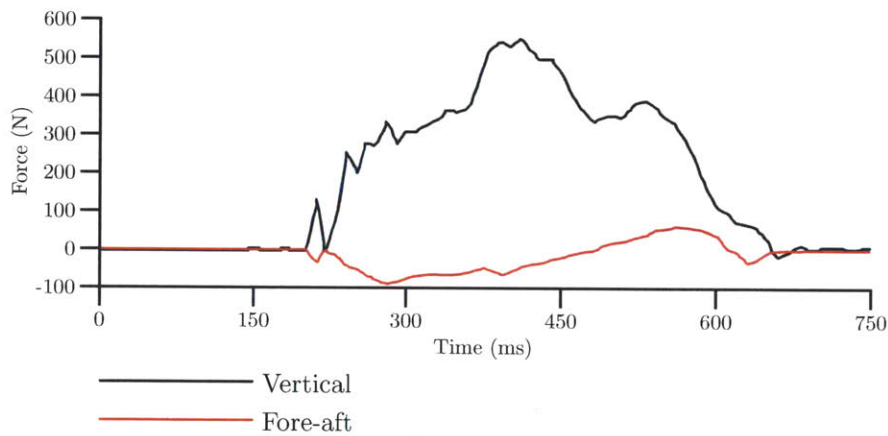


Figure 6-3: Ground reaction forces for single leg test.

6.3 Multi Leg Testing

Multi leg testing is still in its early stages, however the robot, with a third iteration leg, has been commanded to jump vertically (cf. Figure 6-4).



Figure 6-4: Vertical jumping of four legged robot.

Chapter 7

Summary/Conclusions

7.1 Design considerations

In approaching the design of a robotic system for dynamic locomotion, several characteristics are of the utmost importance. First, the body mass must be kept as low as possible. Every effort must be made to avoid a runaway increase in mass, as this will often lead to a severe deterioration in performance. It is difficult or perhaps impossible to break even by increasing the mass in a dynamic system due to the many nonlinearities that are encountered along the way.

As for the leg design in particular four design principles are proposed:

- Minimize passive mechanical impedance
- Minimize mass and inertia
- Maximize actuator strength
- Find a balance between kinematics and leg use

These considerations are based on analysis of biological systems, dynamic simulation and experimental testing. The transfer of information from biology to robotics must occur at the lowest level, the level of fundamental principles.

7.2 Unique Features

Many of the features developed to enhance the performance of this particular robot may be extended to other robotic platforms. The concentric motor topology and redistribution of mass to the proximal extents of limbs provides a substantial increase in performance versus an actuator at the joint topology, particularly when speeds are increased. Careful attention must be paid to all mass placed distally in the limbs and there must be a very good reason for placing it there and nowhere else.

Utilization of motors at the limit of their performance is something that has been largely overlooked by many roboticists. Strict adherence to a constant voltage specification is a suitable way to use electromotive actuators in industrial settings but under loading conditions of legged robots this strategy massively and unnecessarily reduces the performance envelope of the system. This often leads to the introduction of additional performance limiting compromises such as an increase in gear ratio. A one or two time constant motor thermal model is within the reach of even the simplest embedded controllers and the potential increase in performance is enormous.

Tendons and the redistribution of bending loads, greatly enhances the overall strength to weight ratio of the leg and avoids the need for expensive and time consuming machining of the rather large leg links. The tendons can be either active, as the tricep of the front leg, providing locomotive forces to the elbow, or passive as in the lower limb tendon of the front leg.

The use of tendons enables the introduction of alternative materials and manufacturing techniques for use in the leg links. The ideal material is highly durable, with a high yield strength, but not necessary a very high stiffness. Polymers are a good fit for this application and are readily available with a range of stiffness and strength characteristics. The advantage of using thermoset polymers is that they can easily be molded into the desired leg shape, eliminating the need to machine the numerous copies required for a complete robot. The moulds can be made from a wide range of materials, such as wax, Delrin or aluminum. The total mass of a plastic limb can be reduced by the in-molding of a low density polymer foam core or by creating a link with a thin central web.

7.3 Design tools

The design tools proposed here are intended to guide the designer in developing an intuitive understanding of the legged system being developed. Very few of these tools are available to the roboticist and even simple changes, such as increasing the length of a leg link by 1 cm, may have a substantial, yet completely non-intuitive effect on the performance of the leg during locomotion tasks. This sensitivity and complexity provides an enormous and intimidating challenge to the designer who, without these tools, must often arbitrarily select a geometry, typically one that is based on biological data, and forego exploration and optimization of the leg system.

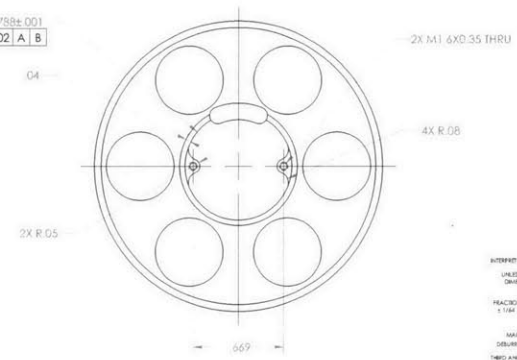
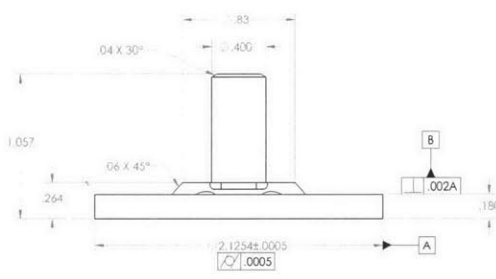
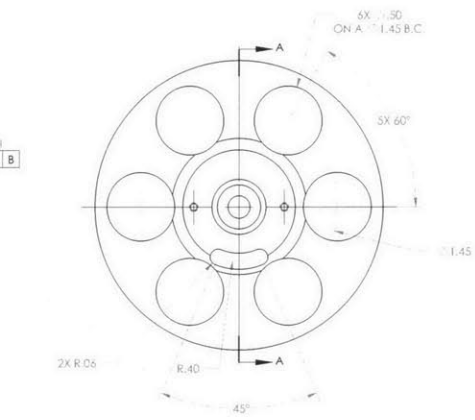
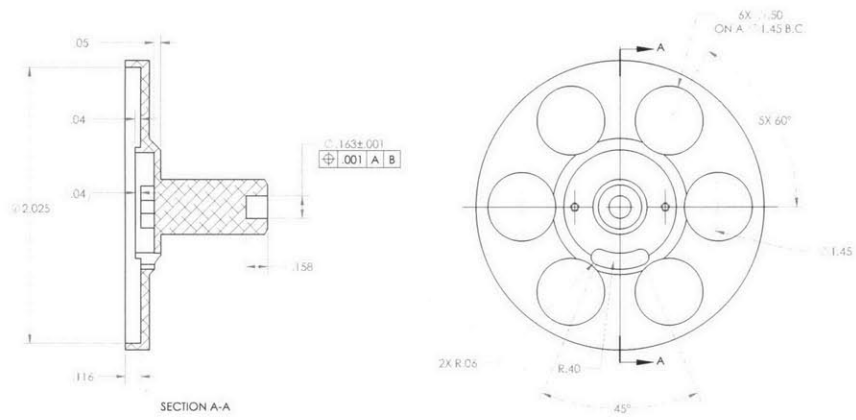
The force map is a simple graphical method of viewing the potential locomotive characteristics of a leg design. Because this view is velocity dependent it can be used compare the effects of leg geometries, masses or actuators on limit dynamic performance. Enlarging the area of the force map, in particular the area to the right of $F_{bx} = 0$, is paramount to designing a more capable leg. The effect of increasing distal leg mass for example can be easily connected to the abrupt decrease in dynamic capability at higher speeds.

Stride planning is perhaps one of the most difficult control tasks that need to be addressed. Many aspects of the leg performance such as actuator, friction and speed limits must be considered in making a decision about foot placement. To further complicate matters this decision must often be made quickly, with input data of questionable quality. The method proposed in this document is an extensible yet simple approach to generating touch-down configurations for arbitrary shoulder position and forces profiles.

Appendix A

Engineering Drawings

This appendix contains the engineering drawings for 26 parts that were custom machined for the front and rear legs. The naming convention utilized prefixes files with either a1_ for anterior lateral components (parts used in front legs on either side), p1_ for posterior lateral components (parts used in rear legs on either side) or oc_ for omnes crura (parts used in all legs). The exception to this convention is the three gears which have no prefix.



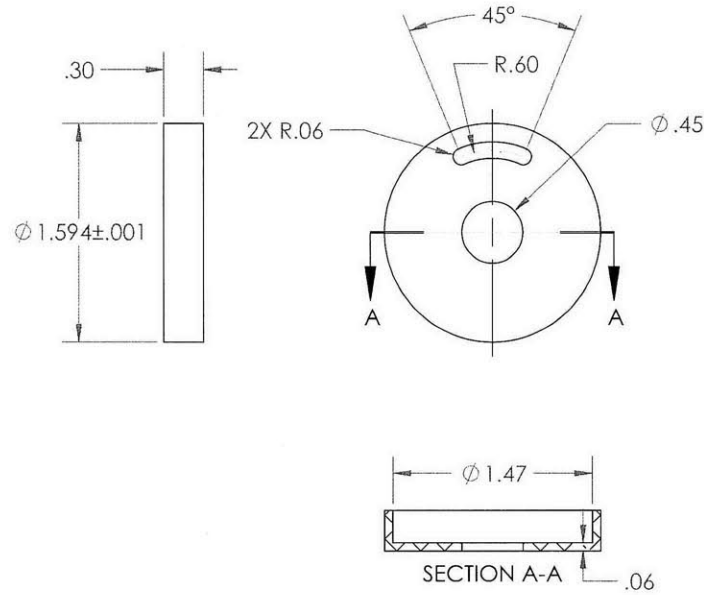
PROPRIETARY AND CONFIDENTIAL
 THIS DOCUMENT AND THE INFORMATION CONTAINED HEREIN IS THE SOLE PROPERTY OF THE BIOMIMETIC ROBOTICS LAB. NO REPRODUCTION IN PART OR AS A WHOLE WITHOUT THE WRITTEN PERMISSION OF THE LAB IS PERMITTED.

INTERFAC DRAWING PER ASME Y14.5M	DATE	2/28/2011
UNLESS OTHERWISE SPECIFIED:	CHECKED	GARY
DIMENSIONS ARE IN INCHES	DRAWN BY	4/15/2011
TOLERANCES	NOTES	
FRACTIONS DECIMALS ANGLES	1. MATERIAL	ALUMINUM ALLOY
1/16" ±.01 1/32 ±.005 1/2° ±.01	2. FINISH	ACCORDANCE WITH ANS-Q-A-200/11
MACHINED SURFACES OF	3. COATING	DI-ELECTRIC ANODIZE
DRILL AND REAM SHARP EDGES	4. TREATMENT	REFLECT ALL DIMENSIONS ARE AFTER COATING
90° AND 45° PRODUCTION		

BIOMIMETIC ROBOTICS LAB
 MASSACHUSETTS INSTITUTE OF TECHNOLOGY
 CAMBRIDGE, MASSACHUSETTS

a_encoderMount

SET PART NO. MEL REV. ENG REV.
C B-05 B-02
 WT. SCALE: 2:1 DO NOT SCALE DIM. SHEET 1 OF 1



PROPRIETARY AND CONFIDENTIAL
 THIS DOCUMENT AND THE INFORMATION CONTAINED HEREIN IS THE SOLE PROPERTY OF THE BIOMIMETIC ROBOTICS LAB OF MIT. ANY REPRODUCTION IN PART OR AS A WHOLE WITHOUT THE WRITTEN PERMISSION OF THE BRL IS PROHIBITED.

INTERPRET DRAWING PER ASME Y14.5M

UNLESS OTHERWISE SPECIFIED:
 DIMENSIONS ARE IN INCHES

FRACTIONS	DECIMALS	ANGLES
$\pm 1/64$.XX $\pm .01$	$\pm .5^\circ$
	.XXX $\pm .005$	

MACHINED SURFACES \checkmark
 DEBURR AND BREAK SHARP EDGES

THIRD ANGLE PROJECTION

DRAWN
 JAKE MCKENZIE
 CHECKED
 SANGBAE KIM
 NOTES

1. MATERIAL: ABS

DATE
 3/28/2011
 DATE
 4/15/2011

BIOMIMETIC ROBOTICS LAB
 MASSACHUSETTS INSTITUTE OF TECHNOLOGY
 CAMBRIDGE, MASSACHUSETTS

TITLE

al_encoderWiringDivider

SIZE PART NO.

A

MDL. REV. DWG. REV.

B-03 B-01

WT

SCALE 1:1

DO NOT SCALE DWG

SHEET 1 OF 1

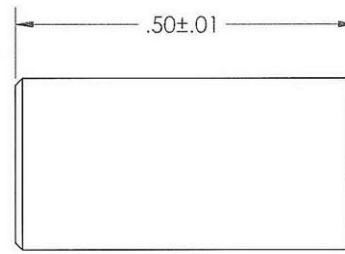
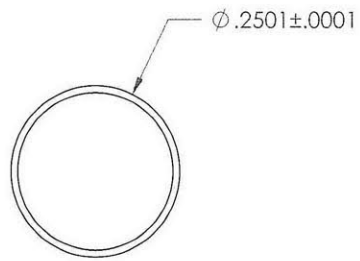
5

4

3

2

1



PROPRIETARY AND CONFIDENTIAL
 THIS DOCUMENT AND THE INFORMATION CONTAINED HERIN IS THE SOLE PROPERTY OF THE BIOMIMETIC ROBOTICS LAB OF MIT. ANY REPRODUCTION IN PART OR AS A WHOLE WITHOUT THE WRITTEN PERMISSION OF THE BRL IS PROHIBITED.

INTERPRET DRAWING PER ASME Y14.5M

UNLESS OTHERWISE SPECIFIED:
 DIMENSIONS ARE IN INCHES

TOLERANCES		
FRACTIONS	DECIMALS	ANGLES
$\pm 1/64$	$.XX \pm .01$	$\pm .5^\circ$
	$.XXX \pm .005$	

MACHINED SURFACES
 DEBURR AND BREAK SHARP EDGES

THIRD ANGLE PROJECTION

DRAWN	DATE
JAKE MCKENZIE	3/12/2011
CHECKED	DATE
SANGBAE KIM	4/15/2011

- NOTES
- MATERIAL:
HARDENED STEEL
 - MCMaster PN:
97395A475

BIOMIMETIC ROBOTICS LAB
 MASSACHUSETTS INSTITUTE OF TECHNOLOGY
 CAMBRIDGE, MASSACHUSETTS

TITLE			
al_outputPin			
SIZE	PART NO.	MDL. REV.	DWG. REV.
A		B-02	B-01
WT	SCALE: 5:1	DO NOT SCALE DWG	SHEET 1 OF 1

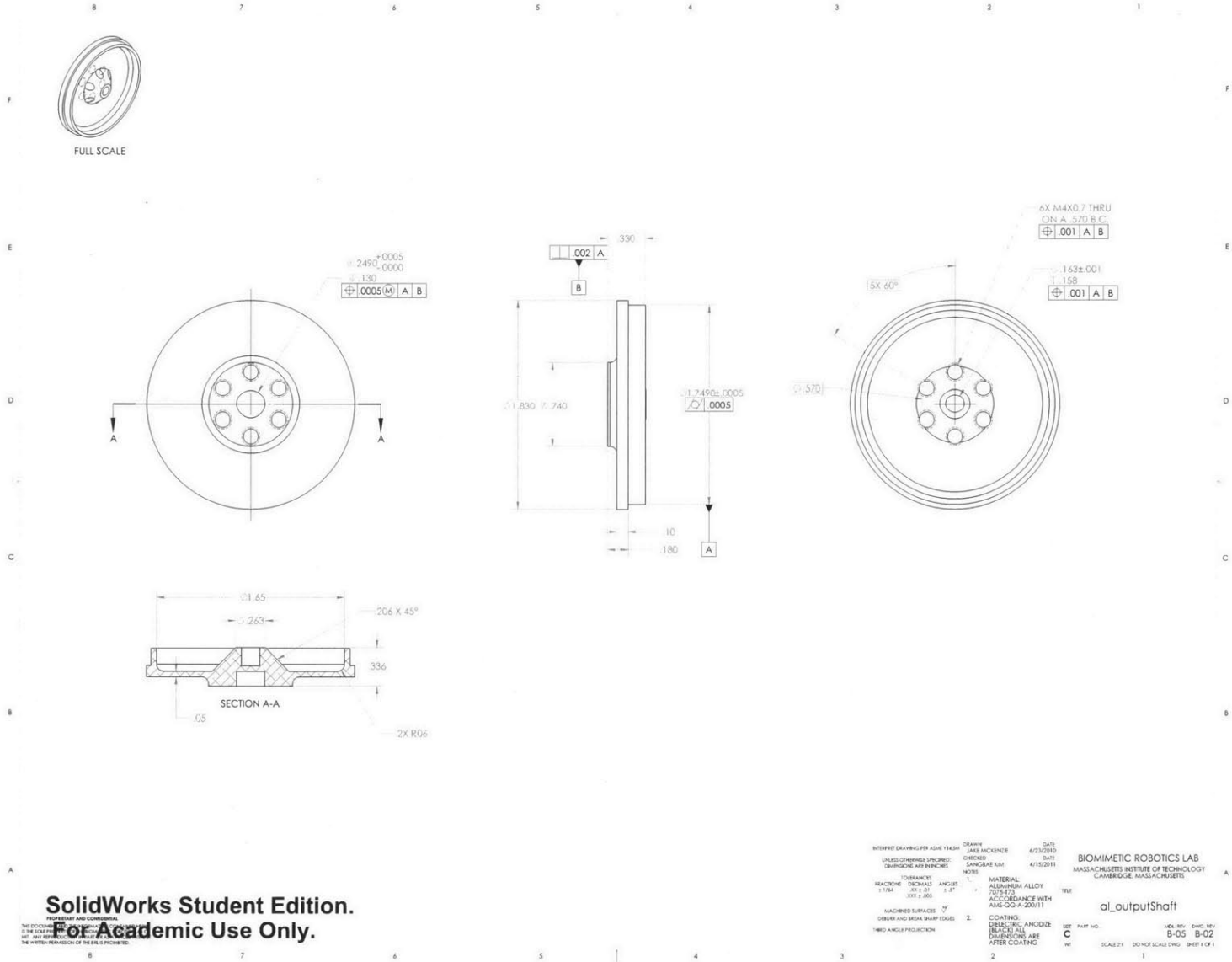
5

4

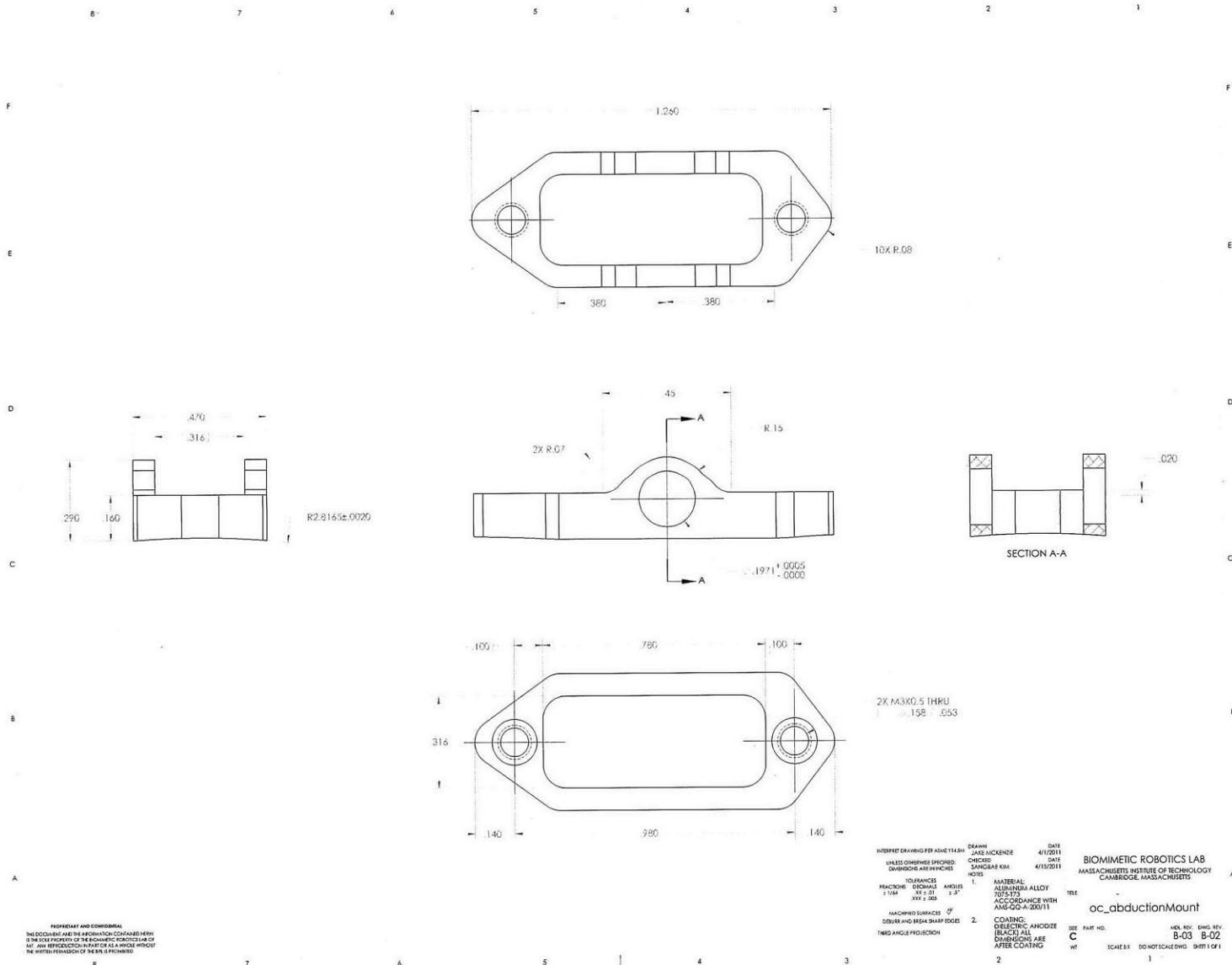
3

2

1

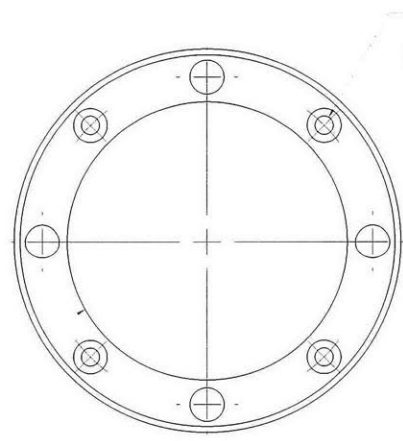
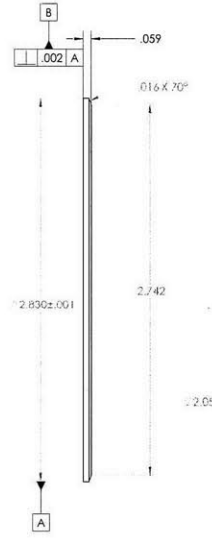
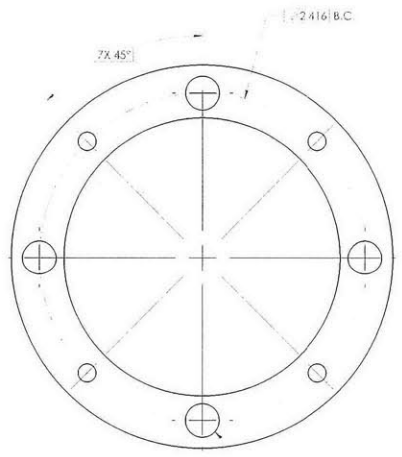


SolidWorks Student Edition.
For Academic Use Only.





FULL SCALE



INTERFER DRAWING PER ASHET 14.5a DRAWN DATE
 UNLESS OTHERWISE SPECIFIED SANGHEE 6/29/2010
 DIMENSIONS ARE IN INCHES SANGHEE KIM DATE 4/19/2011

TOLERANCES UNLESS OTHERWISE SPECIFIED
 FRACTIONS DECIMALS ANGLES
 1/16 .001 .001 1.5°
 .XX ± .005

1. MATERIAL: 300/304 SS
 2. FINISH: CLEAR PASSIVATE

MAXIMUM SURFACES OF
 DEBUR AND BREAK SHARP EDGES
 HIDE ANGLE PRODUCTION

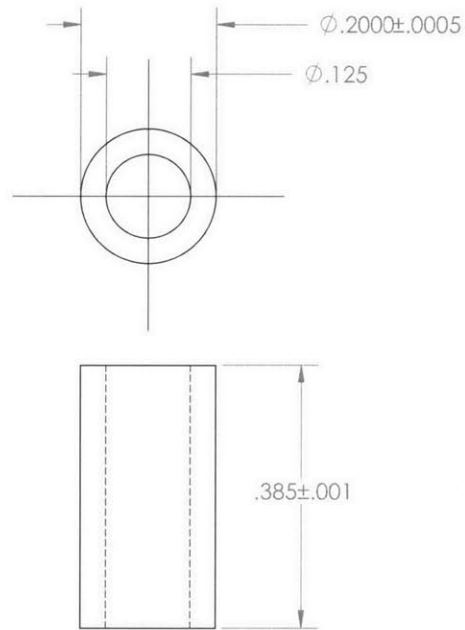
BIOMIMETIC ROBOTICS LAB
 MASSACHUSETTS INSTITUTE OF TECHNOLOGY
 CAMBRIDGE, MASSACHUSETTS

oc_carrierCap

REV PART NO. ASEL REV DWG REV
 C B-01 B-02

WT SCALE 3:1 DO NOT SCALE DWG SHEET 1 OF 1

SolidWorks Student Edition.
 For Academic Use Only.



INTERPRET DRAWING PER ASME Y14.5M

UNLESS OTHERWISE SPECIFIED:
DIMENSIONS ARE IN INCHES

FRACTIONS	TOLERANCES DECIMALS	ANGLES
$\pm 1/64$	$-.XX \pm .01$	$\pm .5^\circ$
	$.XXX \pm .005$	

MACHINED SURFACES $\sqrt{\text{V}}$
DEBURR AND BREAK SHARP EDGES

THIRD ANGLE PROJECTION



DRAWN	DATE
JAKE MCKENZIE	6/27/2010
CHECKED	DATE
SANGBAE KIM	4/15/2011

NOTES

- MATERIAL: 303/304 SS
- FINISH: CLEAR PASSIVATE

BIOMIMETIC ROBOTICS LAB
MASSACHUSETTS INSTITUTE OF TECHNOLOGY
CAMBRIDGE, MASSACHUSETTS

TITLE

oc_carrierSpacer

SIZE	PART NO.	MDL. REV.	DWG. REV.
A		B-01	B-01
WT	SCALE 5:1	DO NOT SCALE DWG	SHEET 1 OF 1

PROPRIETARY AND CONFIDENTIAL

THIS DOCUMENT AND THE INFORMATION CONTAINED HERIN IS THE SOLE PROPERTY OF THE BIOMIMETIC ROBOTICS LAB OF MIT. ANY REPRODUCTION IN PART OR AS A WHOLE WITHOUT THE WRITTEN PERMISSION OF THE BRL IS PROHIBITED.

5

4

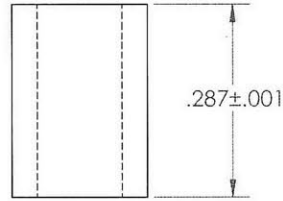
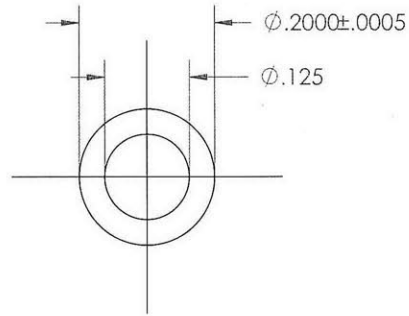
3

2

1




FULL SCALE



INTERPRET DRAWING PER ASME Y14.5M

UNLESS OTHERWISE SPECIFIED:
DIMENSIONS ARE IN INCHES

TOLERANCES	ANGLES
FRACTIONS $\pm 1/64$	$\pm .5^\circ$
DECIMALS XX $\pm .01$.XXX $\pm .005$	

MACHINED SURFACES 
DEBURR AND BREAK SHARP EDGES

THIRD ANGLE PROJECTION

DRAWN	DATE
JAKE MCKENZIE	6/27/2010
CHECKED	DATE
SANGBAE KIM	4/15/2011

NOTES

- MATERIAL: 303/304 SS
- FINISH: CLEAR PASSIVATE

BIOMIMETIC ROBOTICS LAB
MASSACHUSETTS INSTITUTE OF TECHNOLOGY
CAMBRIDGE, MASSACHUSETTS

TITLE
oc_carrierSpacerClearance

SIZE	PART NO.	MDL. REV.	DWG. REV.
A		B-01	B-01
WT	SCALE 5:1	DO NOT SCALE DWG	SHEET 1 OF 1

5

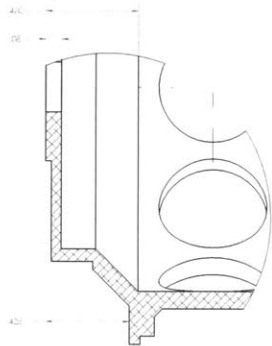
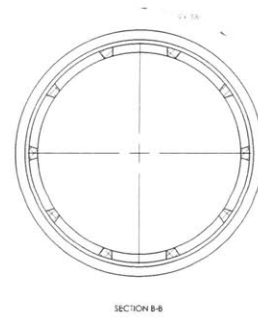
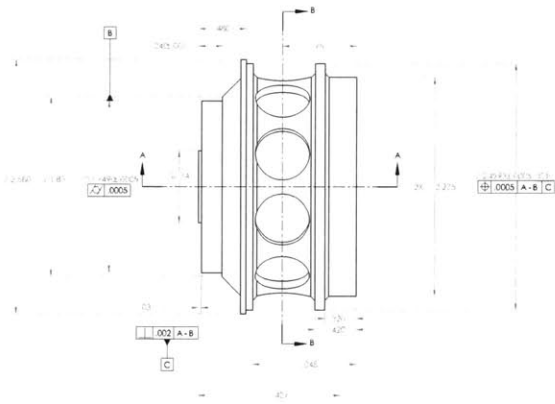
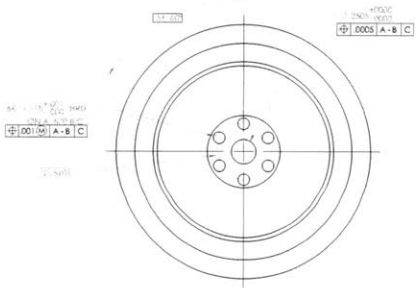
4

3

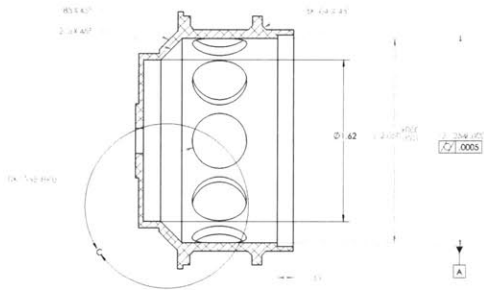
2

1

PROPRIETARY AND CONFIDENTIAL
THIS DOCUMENT AND THE INFORMATION CONTAINED HEREIN IS THE SOLE PROPERTY OF THE BIOMIMETIC ROBOTICS LAB OF MIT. ANY REPRODUCTION IN PART OR AS A WHOLE WITHOUT THE WRITTEN PERMISSION OF THE BRL IS PROHIBITED.



DETAIL C
SCALE 4:1



SECTION A-A

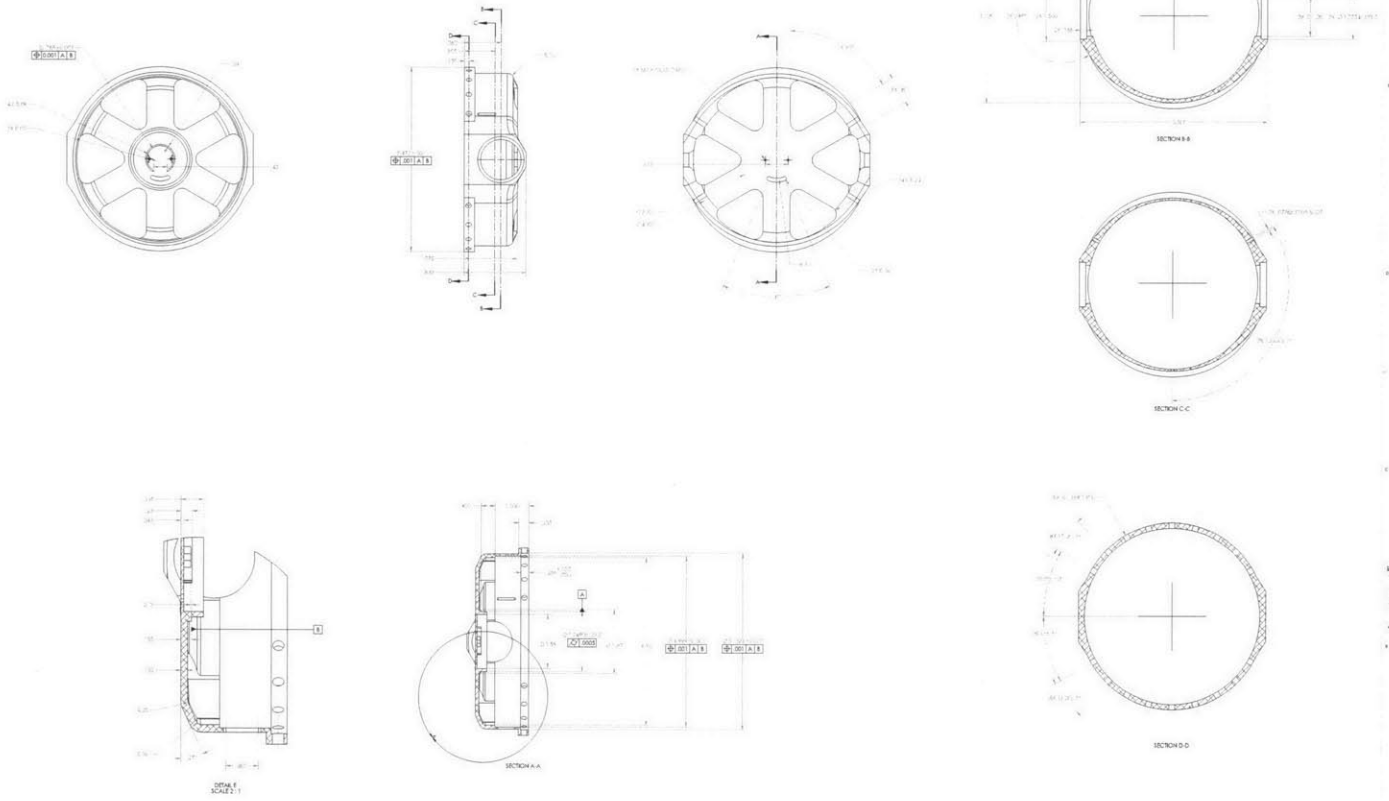
PROPRIETARY AND CONFIDENTIAL
The information contained on this drawing is the property of the University of Massachusetts Lowell and is not to be distributed, copied, or used in any way without the written permission of the University of Massachusetts Lowell.

REVISIONS
1. REVISED DRAWING PER QUOTE 11-10-10
2. REVISED DRAWING PER QUOTE 11-10-10
3. REVISED DRAWING PER QUOTE 11-10-10
4. REVISED DRAWING PER QUOTE 11-10-10
5. REVISED DRAWING PER QUOTE 11-10-10
6. REVISED DRAWING PER QUOTE 11-10-10
7. REVISED DRAWING PER QUOTE 11-10-10
8. REVISED DRAWING PER QUOTE 11-10-10
9. REVISED DRAWING PER QUOTE 11-10-10
10. REVISED DRAWING PER QUOTE 11-10-10

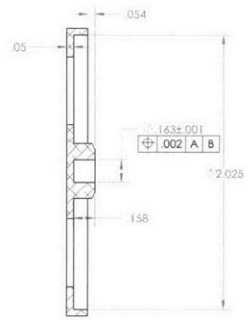
DATE: 11/10/10
DRAWN BY: J. H. HARRIS
CHECKED BY: J. H. HARRIS
APPROVED BY: J. H. HARRIS

UNIVERSITY OF MASSACHUSETTS
LOWELL
BIOAMMETIC ROBOTICS LAB
MANASSAQUETTS INSTITUTE OF TECHNOLOGY
CAMBRIDGE, MASSACHUSETTS

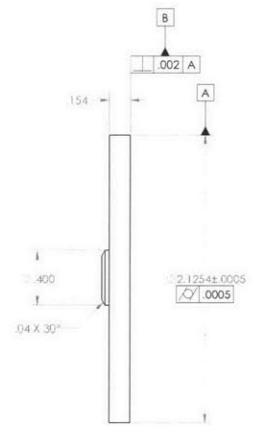
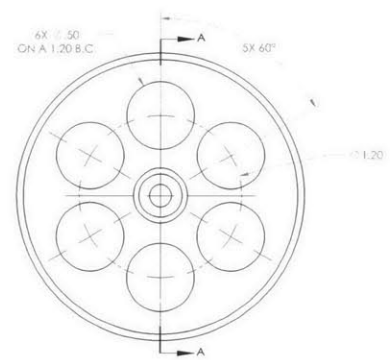
oc_output
B-06 B-02
SCALE: 1:1
DATE: 11/10/10



PROJ. NO.	1000	REV.	01
PROJ. NAME	WHEEL ASSEMBLY	DATE	10/10/2020
PROJ. CODE	1000	DESIGNER	J. J. J.
PROJ. TITLE	WHEEL ASSEMBLY	CHECKER	J. J. J.
PROJ. NO.	1000	DATE	10/10/2020
PROJ. NAME	WHEEL ASSEMBLY	DESIGNER	J. J. J.
PROJ. CODE	1000	CHECKER	J. J. J.
PROJ. TITLE	WHEEL ASSEMBLY	DATE	10/10/2020



SECTION A-A



PROPERTY AND CONFIDENTIAL
 THE SCHEMATIC AND THE INFORMATION CONTAINED HEREIN
 IS THE SOLE PROPERTY OF THE BIOMIMETIC ROBOTICS LAB OF
 MIT. ANY REPRODUCTION IN PART OR AS A WHOLE WITHOUT THE
 WRITTEN PERMISSION OF THE MIT IS PROHIBITED.

INTERPRET DRAWINGS PER ASME Y14.5M DRAWN DATE
 UNLESS OTHERWISE SPECIFIED: MAKE IN CONCORD 3/28/2011
 DIMENSIONS ARE IN INCHES DECIMALS SANICRAF 034 DATE
 REVISIONS: 1. MATERIAL: ALUMINUM ALLOY
 REACTION: 7053 T76 ACCORDANCE WITH
 TOLERANCES: 1. 0.01 2. 0.005
 2. 0.01 3. 0.005
 MACHINED SURFACES: 0.005
 DEBUR AND BREAK SHARP EDGES
 THIRD ANGLE PROJECTION

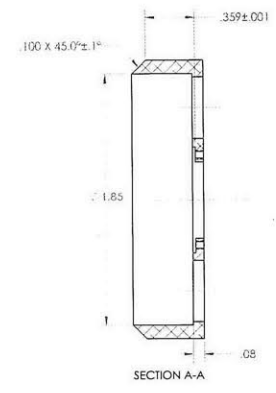
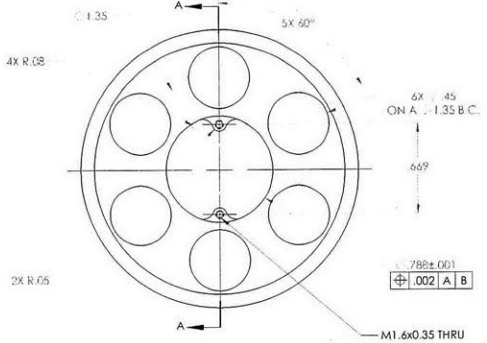
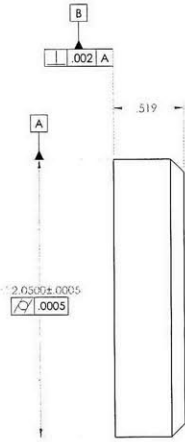
BIOMIMETIC ROBOTICS LAB
 MASSACHUSETTS INSTITUTE OF TECHNOLOGY
 CAMBRIDGE, MASSACHUSETTS
 TEL: 617-253-5911
 FAX: 617-253-5911
 WWW: www.mit.edu
 PART NO. B-05 B-02
 SCALE: 1:1 DO NOT SCALE DWG. SHEET 1 OF 1

pl_encoderMount

8 7 6 5 4 3 2 1

F
E
D
C
B
A

F
E
D
C
B
A



PROPRIETARY AND CONFIDENTIAL
THIS DOCUMENT AND THE INFORMATION CONTAINED HEREIN
IS THE SOLE PROPERTY OF THE BIOMIMETIC ROBOTICS LAB
NO REPRODUCTION IN ANY FORM OR BY ANY MEANS
WITHOUT THE WRITTEN PERMISSION OF THE LAB IS PERMITTED

8 7 6 5 4 3 2 1

INTERPLOT DRAWING FOR ASME Y14.3M	DRAWN	DATE	
UNLESS OTHERWISE SPECIFIED:	CHECKED	DATE	
TOLERANCES ARE IN INCHES	DESIGNED BY	DATE	
	NOTES		
TOLERANCES	1.	MATERIAL	
FRACTIONS	DECIMALS	ALUMINUM ALLOY	
±.154	.XX ± .01	7075-T6	
	.XXX ± .003	ACCORDANCE WITH	
		ASME Y14.3M-2007	
MACHINED SURFACES OF	2.	COATING	
SEMI-AND BEVEL SHARP EDGES		ELECTRIC ANODIZE	
THIRD ANGLE PROJECTION		(BLACK) ALL	
		DIMENSIONS ARE	
		AFTER COATING	

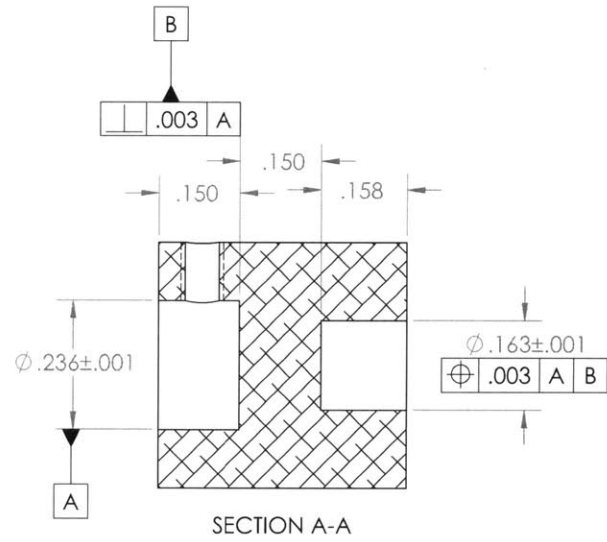
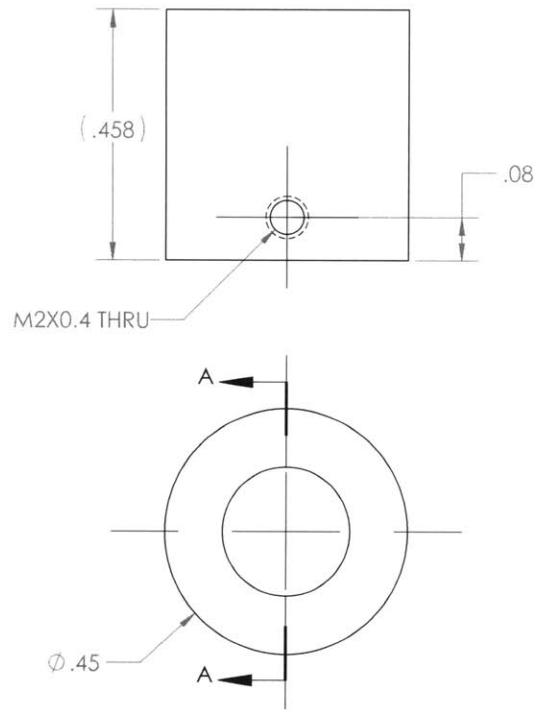
BIOMIMETIC ROBOTICS LAB
MASSACHUSETTS INSTITUTE OF TECHNOLOGY
CAMBRIDGE, MASSACHUSETTS

pI_encoderMountOut

SEE PART NO. C
MATERIAL: ALUMINUM ALLOY 7075-T6
FINISH: ACCORDANCE WITH ASME Y14.3M-2007

REL. REV. ENG. REV.
B-05 B-02

SCALE: 2:1 DO NOT SCALE DIMS. SHEET 1 OF 1



INTERPRET DRAWING PER ASME Y14.5M

UNLESS OTHERWISE SPECIFIED:
DIMENSIONS ARE IN INCHES

FRACTIONS	TOLERANCES DECIMALS	ANGLES
± 1/64	.XX ± .01	± 5°
	XXX ± .005	

MACHINED SURFACES ✓
DEBURR AND BREAK SHARP EDGES

THIRD ANGLE PROJECTION

DRAWN
JAKE MCKENZIE

CHECKED
SANGBAE KIM

NOTES

1.

MATERIAL:
ALUMINUM ALLOY
7075-T73
ACCORDANCE WITH
AMS-QQ-A-200/11

2. COATING:
DIELECTRIC ANODIZE
(BLACK) ALL
DIMENSIONS ARE
AFTER COATING

DATE
3/28/2011

DATE
4/15/2011

BIOMIMETIC ROBOTICS LAB
MASSACHUSETTS INSTITUTE OF TECHNOLOGY
CAMBRIDGE, MASSACHUSETTS

TITLE

pl_encoderShaftEnd

SIZE PART NO.

A

MDL REV DWG. REV.

B-03 B-01

SCALE 4:1 DO NOT SCALE DWG SHEET 1 OF 1

PROPRIETARY AND CONFIDENTIAL
THIS DOCUMENT AND THE INFORMATION CONTAINED HEREIN IS THE SOLE PROPERTY OF THE BIOMIMETIC ROBOTICS LAB OF MIT. ANY REPRODUCTION IN PART OR AS A WHOLE WITHOUT THE WRITTEN PERMISSION OF THE BRL IS PROHIBITED.

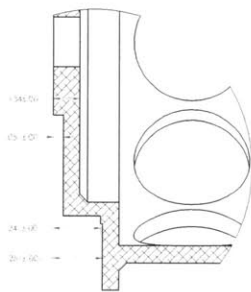
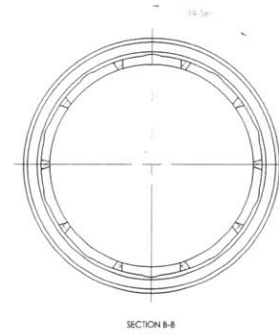
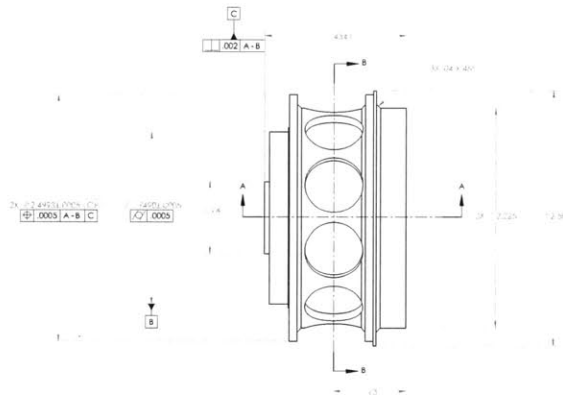
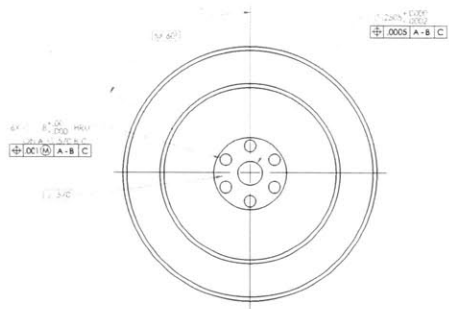
5

4

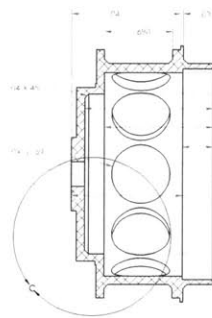
3

2

1



DETAIL C
SCALE 4:1



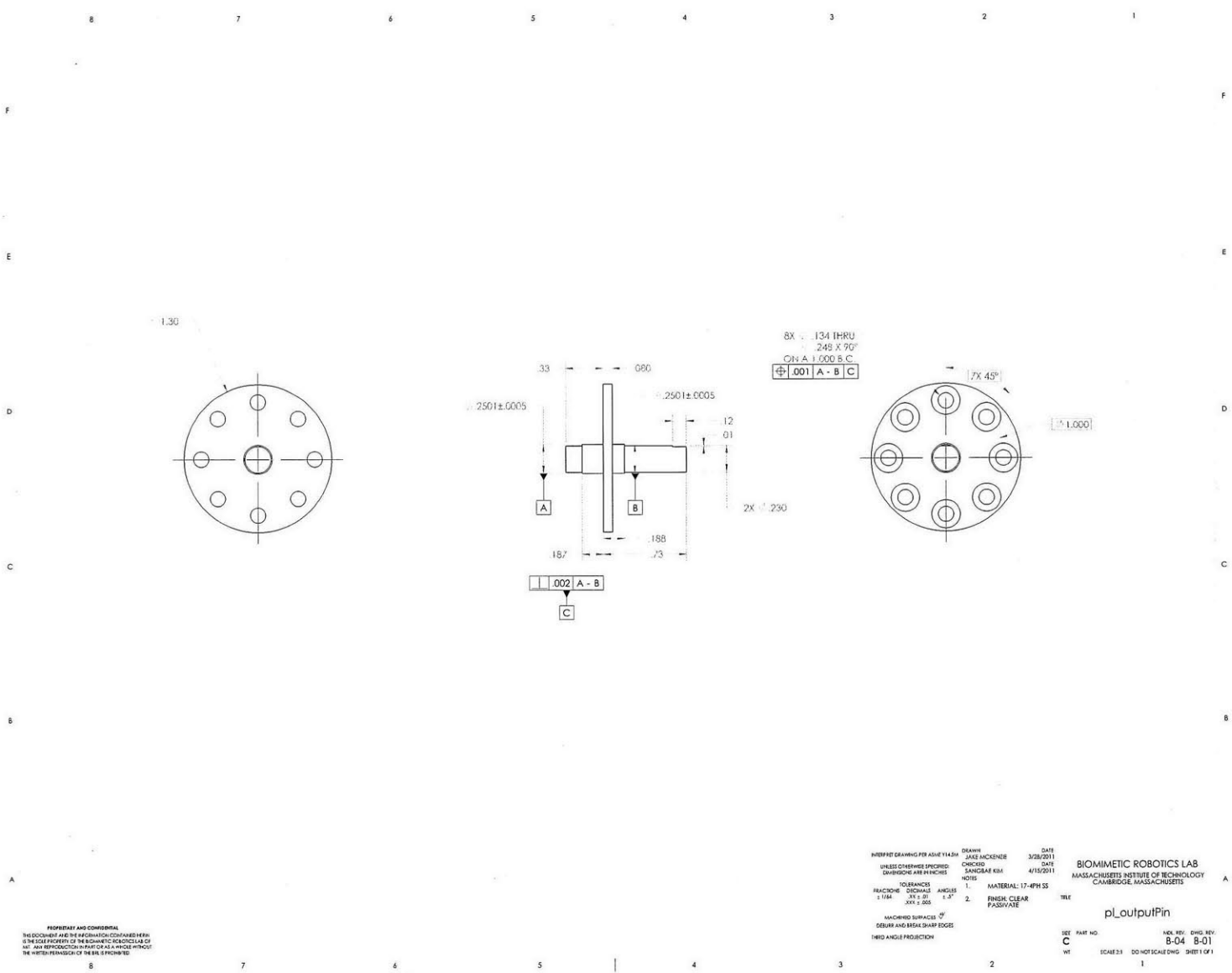
SECTION A-A



PROFITABILITY AND COMPLIANCE:
 THE INFORMATION ON THIS DRAWING IS THE PROPERTY OF BOMANETIC ROBOTICS LAB. IT IS TO BE USED ONLY FOR THE PROJECT AND NOT FOR ANY OTHER PURPOSE. ANY REPRODUCTION OR DISTRIBUTION OF THIS DRAWING WITHOUT THE WRITTEN PERMISSION OF BOMANETIC ROBOTICS LAB IS STRICTLY PROHIBITED.

DESIGNER	DATE	BOMANETIC ROBOTICS LAB MACHINERY SERVICE OF BOSTON COLLEGE CAMBRIDGE, MASSACHUSETTS	
PROJECT ENGINEER	3/2/2016		
DESIGNED BY	DATE	piFemurOutput	
APPROVED BY	4/15/2011		
REVISIONS:	NO.	DATE	DESCRIPTION
1	1	3/2/2016	INITIAL DESIGN
2	1	3/2/2016	ADDED DIMENSIONS
3	1	3/2/2016	ADDED DIMENSIONS

SCALE: 1:1
 SHEET NO.: 8-06
 PART NO.: 8-06 8-01
 DATE: 3/2/2016

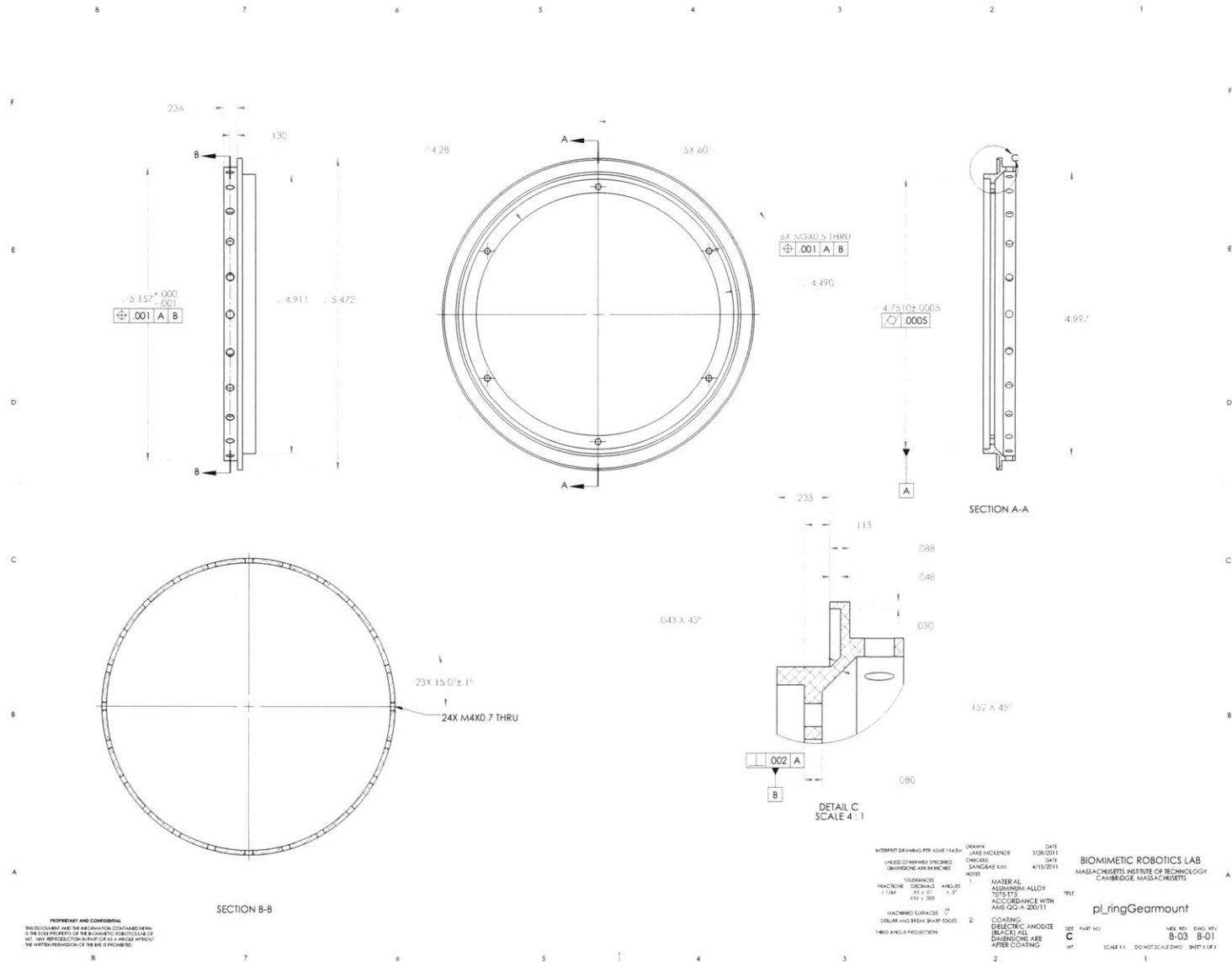


PROPRIETARY AND CONFIDENTIAL
 THIS DOCUMENT AND THE INFORMATION CONTAINED HEREIN
 IS THE SOLE PROPERTY OF THE BIOMIMETIC ROBOTICS LAB OF
 MIT. NO REPRODUCTION IN ANY FORM OR BY ANY MEANS
 WITHOUT THE WRITTEN PERMISSION OF THE MIT IS FORN/NO

INTERPRET DRAWING PER ASME Y14.5m
 UNLESS OTHERWISE SPECIFIED:
 DIMENSIONS ARE IN INCHES
 TOLERANCES DECIMALS ANGLES
 .1254 .001 1.0°
 .001 .005 .5°
 MACHINED SURFACES
 DEBURR AND BREAK SHARP EDGES
 HIDDEN ANGLE PROJECTION

DESIGNER: JAKE ACKENSE
 CHECKED: SANGSUK KIM
 DATE: 3/28/2011
 DATE: 4/15/2011
 MATERIAL: 17-4PH SS
 FINISH: CLEAR
 PASSWAIR

BIOMIMETIC ROBOTICS LAB
 MASSACHUSETTS INSTITUTE OF TECHNOLOGY
 CAMBRIDGE, MASSACHUSETTS
 pLoutpuPin
 SEE PART NO. C
 WT SCALE: 2:1
 DESK REV: DWG REV: B-04 8-01
 SHEET 1 OF 1



Appendix B

Matlab Code Listing

The code that follows is capable of producing the shape dependent force envelopes and force maps used in the body of this document. It is broken up into six files.

- `link.m` — the lowest level code creates link objects for a serial chain
- `chain.m` — arranges link objects into a chain object which is later used to derive the equations of motion
- `profDesign.m` — stride profile designer, outputs force and shoulder trajectories
- `strideInit.m` — stride initialization, calculates equations of motion and solves for the parameters of the SDFE in each configuration
- `strideComp.m` — stride computations, calculates the ideal foot placement locations based on the results of `strideInit.m`
- `envPlot.m` — plots the force production envelopes given the output of `strideInit.m`

```

1  classdef link
2
3
4
5      properties
6          type = 'R';
7          l    = 0;
8          lc   = 0;
9          N    = eye(3);
10         ul   = Inf;
11         ll   = -Inf;
12     end
13
14     methods
15
16
17         function obj = link(type, l, lc, m, I)
18             if(nargin > 0)
19                 obj.type = type;
20                 obj.l    = l;
21                 obj.lc   = lc;
22                 obj.N    = diag([m,m,I]);
23             end
24         end
25
26
27         function obj = limits(obj, ll, ul)
28             if (nargin == 3)
29                 if ll >= ul
30                     temp = ll;
31                     ll = ul;
32                     ul = temp;
33                 end
34
35                 obj.ll = ll;
36                 obj.ul = ul;
37             end
38         end
39
40
41     end
42 end

```

```

1 classdef chain
2
3
4
5     properties
6
7         L     = {};
8
9
10        ic    = [];
11        g     = [0;-9.81;0];
12        qs    = [];
13        k     = [];
14        tau   = [];
15        fx    = [];
16        fy    = [];
17        fecc  = [];
18    end
19
20    methods
21
22        function obj = chain(LN)
23
24            if nargin > 0
25                n = length(LN);
26
27                obj.L = LN;
28
29                obj.ic = zeros(2*n,1);
30                obj.qs = zeros(n,1);
31                obj.k = diag(zeros(1,n));
32                obj.tau = zeros(n,1);
33                obj.fx = zeros(n,1);
34                obj.fy = zeros(n,1);
35                obj.fecc = zeros(n,1);
36
37            end
38
39        end
40    end
41 end

```

```

1  function profDesign
2
3
4
5
6
7
8
9
10
11
12
13  steps = 20;
14  dur   = 0.6;
15
16
17
18
19
20
21
22
23
24
25
26
27
28
29
30  c = sym('c',[7,1]);
31  u = sym('u',[5,1]);
32  syms t u1 u2 u3 u4 u5 real;
33  c([1]) = -6;
34  c([2]) = 6;
35  c([3]) = 0;
36  c([4]) = -12;
37  c([5]) = 18;
38  c([6]) = -6;
39  c([7]) = 0;
40  fly_nom = poly2sym(c(1:3),t);
41  flx_nom = poly2sym(c(4:7),t);
42  flx_asym = flx_nom + 6*u(5)*t^2 - 6*u(5)*t;
43  fly = u(3)*compose(fly_nom, u(2)*(t-u(1)), t, t);
44  flx = u(4)*compose(flx_asym, u(2)*(t-u(1)), t, t);
45

```

```

46
47
48 fx = matlabFunction(subs(flx, {u1,u2,u3,u4,u5}, {0,1/.2,250,75,-.75}));
49 fy = matlabFunction(subs(fly, {u1,u2,u3,u4,u5}, {0,1/.2,250,75,-.75}));
50
51
52 t_steps = linspace(0,dur,steps);
53 fx_steps = fx(t_steps);
54 fy_steps = fy(t_steps);
55
56
57
58
59
60
61
62
63
64
65
66
67
68 method = 1;
69
70 switch method
71 case 0
72
73 m = 19.75;
74
75
76 x_ic = [0
77         0
78         2.4
79         -.45];
80
81 args = {m, fx, fy};
82 [t,x] = ode45(@numint,t_steps,x_ic,[],args);
83
84 xp = x(:,1);
85 yp = x(:,2);
86
87
88
89
90

```

```

91
92 case 1
93
94 v = 1;
95
96 ht = 0.45;
97
98 qvar = sym('qvar','real');
99 qp_i = real(sort(eval(solve(.320*sin(qvar)+.240*sin(-10*pi/180+qvar)-ht))));
100
101 xp_i = .320*cos(qp_i(2))+.240*cos(-10*pi/180+qp_i(2));
102 xp_f = .320*cos(qp_i(1))+.240*cos(-10*pi/180+qp_i(1));
103 xp = linspace(xp_i,xp_f,steps);
104 yp = ones(size(t_steps))*ht;
105
106
107
108
109 end
110
111
112
113
114
115
116 save('case1_xy_data','ix_steps','iy_steps','xp','yp')
117
118 end
119
120
121 function dxdt = numint(t,x,args)
122 m = args{1};
123 g = 9.81;
124 fx = args{2}(t);
125 fy = args{3}(t);
126
127 dxdt = zeros(size(x));
128 dxdt(1:2) = x(3:4);
129 dxdt(3) = fx/m;
130 dxdt(4) = (fy-m*g)/m;
131 end

```

```

1  function strideInit(in_v, in_fname)
2
3
4
5
6
7
8  close all
9  clc
10
11  initxp = 0;
12  inityp = 0;
13  initxv = in_v;
14
15  i_s    = 0.004660;
16  i_k    = 0.000987;
17
18  savefile = in_fname;
19
20
21
22
23
24
25  m1 = 0.180;
26  l1 = 0.320;
27  lc1 = l1/2;
28  Ic1 = 1/12*m1*(l1^2+0.02^2);
29
30  m2 = 0.200;
31  l2 = 0.240;
32  lc2 = l2/2;
33  Ic2 = 1/12*m2*(l2^2+0.02^2);
34
35
36
37  L1 = link('R',l1,lc1,m1,Ic1);
38  L2 = link('R',l2,lc2,m2,Ic2);
39  L1 = L1.limits(45*pi/180, 135*pi/180);
40  L2 = L2.limits(-45*pi/180, -10*pi/180);
41
42  C = chain({L1, L2});
43  savechain(C)
44  load('chain_cache')
45  load('trajectory_cache')

```

```

46
47
48
49
50
51
52
53 res_q = length(xp);
54 res_t = 20;
55
56 args = {M_fun, Q_fun, Gk, Gst, C};
57
58 counter = 1;
59 cmap = colormap(jet(res_q));
60
61 q1s2 = sym('q1s2','positive');
62 q2s2 = sym('q2s2','positive');
63
64 x = xp + initxp;
65 y = yp + inityp;
66
67
68 for i = 1:res_q
69     options = optimset('Display','off');
70     qfunc = matlabFunction([C.L{1}.l*sin(q1s2)+C.L{2}.l*sin(q1s2+q2s2) - ...
71         y(i);C.L{1}.l*cos(q1s2)+C.L{2}.l*cos(q1s2+q2s2) - x(i)],'mat',{'[q1s2;q2s2]});
72     qres = fsolve(qfunc,[pi;-pi],options);
73
74     q1(i) = qres(1);
75     q2(i) = qres(2);
76 end
77
78
79
80 clear q1 q2
81 qn = 20;
82 qr1 = linspace(45*pi/180,135*pi/180,qn);
83 qr2 = linspace(-45*pi/180,-10*pi/180,qn);
84 for i = 1:qn
85     for j = 1:qn
86         q1(qn*(i-1)+j) = qr1(i);
87         q2(qn*(i-1)+j) = qr2(j);
88     end
89 end

```



```

90
91 res_q = length(q1);
92 cmap = colormap(jet(length(q1)));
93
94
95
96
97
98
99
100
101 for j = 1:length(q1)
102     [n1x, n1y] = pol2cart(q1(j),C.L{1}.l);
103     [n2x, n2y] = pol2cart(q1(j)+q2(j),C.L{2}.l);
104     n2x = n2x + n1x;
105     n2y = n2y + n1y;
106
107     figure(1), hold on
108     configplot = plot([0,n1x,n2x],[0,n1y,n2y], 'b'); axis equal
109     set(configplot, 'Color', cmap(j,:))
110 end
111
112
113
114
115
116
117 tau_s = 0;
118 tau_k = 0;
119
120
121 for i = 1:res_q
122     counter = 1;
123     for velo = initxv;
124
125         C.tau(1) = tau_s;
126         C.tau(2) = tau_k;
127         C.ic      = [q1(i);q2(i);0;0];
128
129         args = {M_fun, Q_fun, Gk, Gst, C};
130
131         q = [q1(i); q2(i)];
132         vp = [velo; 0];
133         ap = [0; 0];
134

```

```

135
136     [q,qd,qdd] = remap(q,vp,ap,args);
137
138     C.ic   = [q1(i);q2(i);qd(1);qd(2)];
139     C.tau  = [0;0];
140     args   = {M_fun, Q_fun, Gk, Gst, C};
141     [F_pz] = fcalc(q,qd,qdd,args);
142
143     C.tau  = [1;0];
144     args   = {M_fun, Q_fun, Gk, Gst, C};
145     [F_ps] = fcalc(q,qd,qdd,args);
146
147     C.tau  = [0;1];
148     args   = {M_fun, Q_fun, Gk, Gst, C};
149     [F_pk] = fcalc(q,qd,qdd,args);
150
151     C.tau  = [0;0];
152     args   = {M_fun, Q_fun, Gk, Gst, C};
153     [tau, F_pf] = tcalc(q,qd,qdd,args);
154
155     T = [-F_pk(1)+F_pz(1), -F_ps(1)+F_pz(1), -F_pz(1);
156         -F_pk(2)+F_pz(2), -F_ps(2)+F_pz(2), -F_pz(2);
157         0, 0, 1];
158
159
160     tau_si = sum(qdd)*i_s;
161     tau_ki = qdd(2)*i_k;
162     tau_smax = 30;
163     tau_kmax = 150;
164
165
166     p1 = T*[tau_kmax-tau_ki ;tau_smax-tau_si ;1];
167     p2 = T*[tau_kmax-tau_ki ;-tau_smax-tau_si ;1];
168     p3 = T*[-tau_kmax-tau_ki ;tau_smax-tau_si ;1];
169     p4 = T*[-tau_kmax-tau_ki ;-tau_smax-tau_si ;1];
170
171
172     s1 = -F_pf;
173     s2 = [.9*300;300;1]-F_pf;
174     s3 = [-.9*300;300;1]-F_pf;
175
176
177     D(i).F_f   = -F_pf(1:2);
178     D(i).T     = T;
179     D(i).Ti    = T^-1;

```

```

180         D(i).tau_si = tau_si;
181         D(i).tau_ki = tau_ki;
182
183
184         figure(2), hold on, axis equal
185         plot([p1(1),p2(1),p4(1),p3(1),p1(1)], [p1(2),p2(2),p4(2),p3(2),p1(2)], 'r')
186         plot([s2(1),s1(1),s3(1)], [s2(2),s1(2),s3(2)], 'b')
187
188
189         plot(-F_pf(1),-F_pf(2), 'r')
190
191
192         counter = counter+1;
193     end
194 end
195
196 save(['@-@-@',savefile], 'D')
197
198 end
199
200 function [F_p] = fcalc(q,qd,qdd,args)
201
202
203
204
205
206 n = length(q);
207
208
209
210
211
212 Ms = args{1}([q;qd]);
213 Qs = args{2}([q;qd]);
214 C = args{5};
215
216 for k = 1:n
217     G{k} = args{3}{k}([q;qd]);
218     Gst{k} = args{4}{k}([q;qd]);
219 end
220
221
222
223
224

```

```

225
226
227 qs = C.qs;
228 K = C.k;
229
230 T = [0; ...
      C.tau(2)];
231 FX = [0; ...
      0];
232 FY = [0; ...
      0];
233 TS = C.tau(1);
234
235
236
237
238
239 SF = zeros(n,1);
240 for k = 1:n
241     qsum = sum(q(1:k));
242     FK = C.g*C.L{k}.N(1)+[FX(k);FY(k);C.fecc(k)*(FY(k)*cos(qsum)-FX(k)*sin(qsum))];
243     SF = SF + G{k}'*(FK);
244 end
245 clear FK qsum
246
247
248
249
250
251
252 qsum = sum(q(1:n));
253 r = [(C.L{n}.l-C.L{n}.lc)*cos(qsum); (C.L{n}.l-C.L{n}.lc)*sin(qsum); 0];
254
255
256
257
258
259
260
261 TE = zeros(n,1);
262
263
264
265
266

```

```

267
268 for k = 1:n
269     Gst{k} = mat2cell(Gst{k}, 3*ones(1,n), ones(1,n));
270     BLAH = {zeros(3,1), zeros(3,1)};
271     for i = 1:n
272         for j = 1:n
273             BLAH{1,i} = BLAH{1,i} + qd(j).*Gst{k}{j,i};
274         end
275     end
276
277     Gj{k} = zeros(3,1);
278     for i = 1:n
279         Gj{k} = Gj{k} + BLAH{1,i}.*qd(i);
280     end
281     clear BLAH
282
283 end
284
285
286
287
288 for k = n:-1:1
289     qsum = sum(q(1:k));
290     Fk = C.g*C.L{k}.N(1)+[FX(k);FY(k);TE(k)];
291
292
293     if k == n
294         Ft{k} = C.L{k}.N*(G{k}*qdd+Gj{k}) - Fk - [0;0;T(2)] - [0;0;TS];
295
296
297     else
298
299
300         Ft{k} = C.L{k}.N*(G{k}*qdd+Gj{k}) - Fk + [0;0;T(2)];
301
302
303
304     end
305 end
306
307 Fj1x = sym('Fj1x','real');
308 Fj1y = sym('Fj1y','real');
309 Fj2x = sym('Fj2x','real');
310 Fj2y = sym('Fj2y','real');
311 Fe2x = sym('Fe2x','real');

```

```

312 Fe2y = sym('Fe2y','real');
313
314 r = [(-C.L{2}.lc)*cos(sum(q(1:2))); (-C.L{2}.lc)*sin(sum(q(1:2))); 0];
315 Fj22 = [Fj2x; Fj2y; 0] + cross(r,[Fj2x;Fj2y;0]);
316
317 r = [(C.L{2}.l-C.L{2}.lc)*cos(sum(q(1:2))); (C.L{2}.l-C.L{2}.lc)*sin(sum(q(1:2))); 0];
318 Fe22 = [Fe2x; Fe2y; 0] + cross(r,[Fe2x;Fe2y;0]);
319
320 r = [(C.L{1}.l-C.L{1}.lc)*cos(q(1)); (C.L{1}.l-C.L{1}.lc)*sin(q(1)); 0];
321 Fj21 = [-Fj2x; -Fj2y; 0] + cross(r,[-Fj2x; -Fj2y; 0]);
322
323 r = [(-C.L{1}.lc)*cos(q(1)); (-C.L{1}.lc)*sin(q(1)); 0];
324 Fj11 = [Fj1x; Fj1y; 0] + cross(r,[Fj1x; Fj1y; 0]);
325
326 forces = solve(Fj22+Fe22-Ft{2},Fj11+Fj21-Ft{1});
327
328 Fj{1} = [eval(forces.Fj1x); eval(forces.Fj1y); 0];
329 Fj{2} = [eval(forces.Fj2x); eval(forces.Fj2y); 0];
330 Fe    = [eval(forces.Fe2x); eval(forces.Fe2y); 0];
331
332
333
334
335
336 F_p = Fe;
337 r = [(C.L{n}.l-C.L{n}.lc)*cos(sum(q(1:2))); (C.L{n}.l-C.L{n}.lc)*sin(sum(q(1:2))); 0];
338 r22 = [(C.L{2}.l-C.L{2}.lc)*cos(sum(q(1:2))); (C.L{2}.l-C.L{2}.lc)*sin(sum(q(1:2))); 0];
339 r21 = [(C.L{1}.l-C.L{1}.lc)*cos(q(1)); (C.L{1}.l-C.L{1}.lc)*sin(q(1)); 0];
340 r11 = [(-C.L{1}.lc)*cos(q(1)); (-C.L{1}.lc)*sin(q(1)); 0];
341
342
343
344
345
346
347
348
349
350 GRF = Fj{1};
351
352
353
354
355
356

```

```
357
358
359
360
361
362
363
364
365
366
367
368
369
370 [n1x, n1y] = pol2cart(q(1),C.L{1}.1);
371 [n2x, n2y] = pol2cart(q(1)+q(2),C.L{2}.1);
372 n2x = n2x + n1x;
373 n2y = n2y + n1y;
374
375
376
377
378
379
380
381
382
383
384
385
386
387
388
389
390
391
392
393
394
395
396
397
398 end
399
400 function [tau, F_pf] = tcalc(q,qd,qdd,args)
401
```

```

402
403
404
405
406 n = length(q);
407
408
409
410
411
412 Ms = args{1}([q;qd]);
413 Qs = args{2}([q;qd]);
414 C = args{5};
415
416 for k = 1:n
417     G{k} = args{3}{k}([q;qd]);
418     Gst{k} = args{4}{k}([q;qd]);
419 end
420
421
422
423
424
425
426
427 qs = C.qs;
428 K = C.k;
429
430 T = [0; ...
      C.tau(2)];
431 FX = [0; ...
      0];
432 FY = [0; ...
      0];
433 TS = C.tau(1);
434
435
436
437
438
439 SF = zeros(n,1);
440 for k = 1:n
441     qsum = sum(q(1:k));
442     FK = C.g*C.L{k}.N(1)+[FX(k);FY(k);C.fecc(k)*(FY(k)*cos(qsum)-FX(k)*sin(qsum))];
443     SF = SF + G{k}'*(FK);

```



```

444 end
445 clear FK qsum
446
447
448
449
450
451
452 qsum = sum(q(1:n));
453 r = [(C.L{n}.l-C.L{n}.lc)*cos(qsum); (C.L{n}.l-C.L{n}.lc)*sin(qsum); 0];
454
455
456
457
458
459
460
461 TE = zeros(n,1);
462
463
464
465
466
467
468 for k = 1:n
469     Gst{k} = mat2cell(Gst{k}, 3*ones(1,n), ones(1,n));
470     BLAH = {zeros(3,1), zeros(3,1)};
471     for i = 1:n
472         for j = 1:n
473             BLAH{1,i} = BLAH{1,i} + qd(j).*Gst{k}{j,i};
474         end
475     end
476
477     Gj{k} = zeros(3,1);
478     for i = 1:n
479         Gj{k} = Gj{k} + BLAH{1,i}.*qd(i);
480     end
481     clear BLAH
482
483 end
484
485
486
487
488 t_k = sym('t_k', 'real');

```

```

489 t_s = sym('t_s','real');
490
491 for k = n:-1:1
492     qsum = sum(q(1:k));
493     Fk = C.g*C.L{k}.N(1)+[FX(k);FY(k);TE(k)];
494
495
496     if k == n
497         Ft{k} = C.L{k}.N*(G{k}*qdd+Gj{k}) - Fk - [0;0;t_k] - [0;0;t_s];
498
499
500     else
501
502
503         Ft{k} = C.L{k}.N*(G{k}*qdd+Gj{k}) - Fk + [0;0;t_k];
504
505
506
507     end
508 end
509
510 Fj1x = sym('Fj1x','real');
511 Fj1y = sym('Fj1y','real');
512 Fj2x = sym('Fj2x','real');
513 Fj2y = sym('Fj2y','real');
514 Fe2x = sym('Fe2x','real');
515 Fe2y = sym('Fe2y','real');
516
517 r = [(-C.L{2}.lc)*cos(sum(q(1:2))); (-C.L{2}.lc)*sin(sum(q(1:2))); 0];
518 Fj22 = [Fj2x; Fj2y; 0] + cross(r,[Fj2x;Fj2y;0]);
519
520 r = [(C.L{2}.l-C.L{2}.lc)*cos(sum(q(1:2))); (C.L{2}.l-C.L{2}.lc)*sin(sum(q(1:2))); 0];
521 Fe22 = [Fe2x; Fe2y; 0] + cross(r,[Fe2x;Fe2y;0]);
522
523 r = [(C.L{1}.l-C.L{1}.lc)*cos(q(1)); (C.L{1}.l-C.L{1}.lc)*sin(q(1)); 0];
524 Fj21 = [-Fj2x; -Fj2y; 0] + cross(r,[-Fj2x; -Fj2y; 0]);
525
526 r = [(-C.L{1}.lc)*cos(q(1)); (-C.L{1}.lc)*sin(q(1)); 0];
527
528 Fj11 = [0; 0; 0] + cross(r,[0; 0; 0]);
529
530 forces = solve(Fj22+Fe22-Ft{2},Fj11+Fj21-Ft{1});
531
532
533 Fj{2} = [eval(forces.Fj2x); eval(forces.Fj2y); 0];

```

```

534 Fe      = [eval(forces.Fe2x); eval(forces.Fe2y); 0];
535 tau     = [eval(forces.t_k); eval(forces.t_s)];
536
537
538
539
540
541 F_pf = Fe;
542 r     = [(C.L{n}.l-C.L{n}.lc)*cos(sum(q(1:2))); (C.L{n}.l-C.L{n}.lc)*sin(sum(q(1:2))); 0];
543 r22   = [(C.L{2}.l-C.L{2}.lc)*cos(sum(q(1:2))); (C.L{2}.l-C.L{2}.lc)*sin(sum(q(1:2))); 0];
544 r21   = [(C.L{1}.l-C.L{1}.lc)*cos(q(1)); (C.L{1}.l-C.L{1}.lc)*sin(q(1)); 0];
545 r11   = [(-C.L{1}.lc)*cos(q(1)); (-C.L{1}.lc)*sin(q(1)); 0];
546
547
548
549
550
551
552
553
554
555
556
557
558
559
560
561
562
563
564
565
566
567
568
569
570
571
572
573
574
575 [n1x, n1y] = pol2cart(q(1),C.L{1}.l);
576 [n2x, n2y] = pol2cart(q(1)+q(2),C.L{2}.l);
577 n2x = n2x + n1x;
578 n2y = n2y + n1y;

```

```

579
580
581
582
583
584
585
586
587
588
589
590
591
592
593
594
595
596
597
598
599
600
601
602
603 end
604
605 function [q,qd,qdd] = remap(q, vp, ap, args)
606 n = length(q);
607
608
609
610
611
612
613
614 C = args{5};
615
616 for k = 1:n
617     G{k} = args{3}{k}([q;zeros(size(q))]);
618     Gst{k} = args{4}{k}([q;zeros(size(q))]);
619 end
620
621
622 vqd = sym('vqpd', [n,1]);
623 vqdd = sym('vqpd', [n,1]);

```

```

624
625
626
627 qsum = sum(q(1:n));
628 r = [(C.L{n}.l-C.L{n}.lc)*cos(qsum); (C.L{n}.l-C.L{n}.lc)*sin(qsum); 0];
629 w = [0;0;sum(vqd)];
630
631 vp_sym = G{n}*vqd+cross(w,r);
632 vp_sym = vp_sym(1:2) - vp;
633
634 qd_sym = solve(vp_sym);
635
636 qd = zeros(n,1);
637 qd(1) = eval(qd_sym.vqd1);
638 qd(2) = eval(qd_sym.vqd2);
639
640
641
642
643
644
645 for k = 1:n
646     Gst{k} = mat2cell(Gst{k}, 3*ones(1,n), ones(1,n));
647     BLAH = {zeros(3,1), zeros(3,1)};
648     for i = 1:n
649         for j = 1:n
650             BLAH{1,i} = BLAH{1,i} + qd(j).*Gst{1}{j,i};
651         end
652     end
653
654     Gj{k} = zeros(3,1);
655     for i = 1:n
656         Gj{k} = Gj{k} + BLAH{1,i).*qd(i);
657     end
658     clear BLAH
659
660 end
661
662
663 qsum = sum(q(1:n));
664 An = G{n}*vqdd+Gj{n};
665 w = [0;0;sum(qd)];
666
667
668 ap_sym = An + cross([0;0;An(3)],r) + cross(w,cross(w,r));

```

```

669 ap_sym = ap_sym(1:2) - ap;
670 qdd_sym = solve(ap_sym);
671
672 qdd = zeros(n,1);
673 qdd(1) = eval(qdd_sym.vqdd1);
674 qdd(2) = eval(qdd_sym.vqdd2);
675
676
677
678 end
679
680 function savechain(C)
681
682 n = length([C.L{:}]);
683
684
685 if(true)
686
687
688     cfgvec = [];
689
690     x = sym('x',[1,n]);
691     y = sym('y',[1,n]);
692     p = sym('p',[1,n]);
693     xc = sym('xc',[1,n]);
694     yc = sym('yc',[1,n]);
695
696     for i=1:n
697
698         eval(['synd', num2str(i), ' = ', num2str(i), ' + 31'])
699
700         if C.L{i}.type == 'E'
701             cfgvec = [cfgvec,1];
702         else
703             cfgvec = [cfgvec,0];
704         end
705
706         qstrn = '';
707         qstrm = '';
708         for j = 1:i
709             if C.L{j}.type == 'E'
710                 qstrn = [qstrn, ' + ', num2str(j), ''];
711                 if j < i || i == 1
712                     qstrm = [qstrm, ' + ', num2str(j), ''];
713                 end

```

```

714         end
715     end
716     clear j
717
718
719
720
721     if i == 1
722         p(i) = 0;
723         x(i) = 0;
724         y(i) = 0;
725     else
726         p(i) = qstrm;
727
728         if C.L{i}.type == 'R'
729             if C.L{i-1}.type == 'P'
730                 x(i) = x(i-1)+C.L{i-1}.l*cos(eval(qstrm));
731                 y(i) = y(i-1)+C.L{i-1}.l*sin(eval(qstrm));
732             else
733                 lastR = find(cfgvec(1:end-1),1,'last');
734
735                 dl = '';
736                 dp = 0;
737                 for j = lastR+1:i-1
738                     dl = [dl,' q',num2str(j),' '];
739                     dp = dp + C.L{j}.l;
740                 end
741                 dl = dl(3:end-1);
742
743                 x(i) = x(lastR)+(C.L{lastR}.l+eval(dl)+dp)*cos(eval(qstrm));
744                 y(i) = y(lastR)+(C.L{lastR}.l+eval(dl)+dp)*sin(eval(qstrm));
745             end
746         else
747             if C.L{i-1}.type == 'R'
748                 x(i) = x(i-1)+C.L{i-1}.l*cos(eval(qstrm));
749                 y(i) = y(i-1)+C.L{i-1}.l*sin(eval(qstrm));
750             else
751                 lastR = find(cfgvec(1:end-1),1,'last');
752
753                 dl = '';
754                 dp = 0;
755                 for j = lastR+1:i-1
756                     dl = [dl,' q',num2str(j),' '];
757                     dp = dp + C.L{j}.l;
758                 end

```

```

759         dl = dl(3:end-1);
760
761         x(i) = x(lastR)+(C.L{lastR}.l+eval(dl)+dp)*cos(eval(qstrn));
762
763         y(i) = y(lastR)+(C.L{lastR}.l+eval(dl)+dp)*sin(eval(qstrn));
764
765     end
766
767     end
768
769     if C.L{i}.type == 'R'
770         xc(i) = x(i) + C.L{i}.lc*cos(eval(qstrn));
771         yc(i) = y(i) + C.L{i}.lc*sin(eval(qstrn));
772     else
773         xc(i) = x(i) + (eval(['q',num2str(i)])+C.L{i}.l-C.L{i}.lc)*cos(p(i));
774         yc(i) = y(i) + (eval(['q',num2str(i)])+C.L{i}.l-C.L{i}.lc)*sin(p(i));
775     end
776
777 end
778
779 M = sym('M', [n,n]);
780
781 for k = 1:n
782     G = sym('G', [3,n]);
783     G(3,:) = ones(1,n);
784     if k < n
785         G(:,k+1:n) = zeros(3,n-k);
786     end
787
788     for i = 1:k
789         if C.L{i}.type == 'R'
790             G(1,i) = y(i)-yc(k);
791             G(2,i) = -x(i)+xc(k);
792         else
793             G(1,i) = cos(p(i));
794             G(2,i) = sin(p(i));
795             G(3,i) = 0;
796         end
797     end
798
799 end
800
801 clear i
802
803 Gs = {};
804
805 for i = 1:n

```



```

802         for j = 1:n
803             Gs(i,j) = eval(['G'+num2str(i)+':', ' ', num2str(j), ' ', num2str(i), ' ']);
804         end
805     end
806     clear i j
807
808
809
810     Gst{k} = sym('Gst', [3*n,n]);
811     if k == 1
812         M = eval(['M'+num2str(k), ' ', num2str(k), ' ']);
813         for i = 1:n
814             for j = 1:n
815                 H(i,j) = ...
816                     eval(['H'+num2str(k), ' ', num2str(i), ' ', num2str(j), ' ']);
817                 Gst{k}((i-1)*3+1:(i-1)*3+3, j) = Gs(i, j);
818             end
819         end
820         Gk{k} = G;
821     else
822         M = eval(['M'+num2str(k), ' ', num2str(k), ' ']);
823         for i = 1:n
824             for j = 1:n
825                 H(i,j) = eval(['H'+num2str(i), ' ', num2str(j), ' ']);
826                 Gk{k}((i-1)*3+1:(i-1)*3+3, num2str(k), ' ', num2str(i), ' ', num2str(j), ' ']);
827                 Gst{k}((i-1)*3+1:(i-1)*3+3, j) = Gs(i, j);
828             end
829         end
830         Gk{k} = G;
831     end
832     clear i j
833
834
835
836     qtstr = 'q1d';
837     varlist(1) = q1;
838     varlist(n+1) = q1d;
839     for i = 2:n
840         varlist(i) = eval(['q', num2str(i)]);
841         varlist(n+i) = eval(['q', num2str(i), 'd']);
842         qtstr = [qtstr, 'q', num2str(i), 'd'];
843     end
844

```

```

845     Q = qthq(H,eval(['[',qtstr,']']));
846     M_fun = matlabFunction(M,'vars',{varlist});
847     Q_fun = matlabFunction(Q,'vars',{varlist});
848     for k = 1:n
849
850         eval(['Gk(',num2str(k),')= ...
851             matlabFunction(Gk(',num2str(k),'),'vars',{varlist});'])
852         eval(['Gc(',num2str(k),')= ...
853             matlabFunction(Gc(',num2str(k),'),'vars',{varlist});'])
854
855     end
856
857     save('chain_cache','M_fun','Q_fun','Gk','Gc')
858 else
859     load('chain_cache')
860 end
861
862 function Q = qthq(H,qd)
863
864 n = length(qd);
865 P = cell([1,n]);
866
867 for i = 1:n
868     for j = 1:n
869         if j==1
870             P{i} = zeros(n,1);
871         end
872         P{i} = P{i} + qd(j)*H{i,j};
873     end
874 end
875 clear i j
876
877 Q = 0;
878 for i = 1:n
879     Q = Q + P{i}*qd(i);
880 end
881
882 end

```

```

1  profile clear
2  profile on
3  tic
4
5  close all
6  clear all
7  clc
8
9
10 n    = 20;
11
12 load('zajektoray_cache')
13 fx = fx_steps;
14 fy = fy_steps;
15
16
17 figure
18 plot([0:n-1],fy,[0:n-1],fx)
19
20
21
22 load('wajektoray');
23
24
25 qsteps = length(D);
26 R = zeros(qsteps, n);
27
28 T1m = 150;
29 T2m = 150;
30 mu  = .9;
31
32 for i = 1:qsteps
33
34     for j = 1:n;
35         T = D(i).Ti*[fx(j);fy(j);1];
36
37         if abs(T(1)) <= T1m && abs(T(2)) <= T2m
38
39             if fy(j) > D(i).F_f(2) && abs((fx(j)-D(i).F_f(1))/(fy(j)-D(i).F_f(2))) <= mu
40                 R(i,j) = 1;
41             end
42         end
43     end
44 end
45

```

```

46 figure
47 spy(R)
48
49
50 testSet = find(R(:,1))
51 pmax = 0;
52 psum = 0;
53 for p = 1:length(testSet)
54     if sum(diag(R,-testSet(p)+1)) >= psum
55         pmax = p;
56         psum = sum(diag(R,-testSet(p)+1));
57     end
58 end
59
60
61
62
63 tc = 1
64 Tau = zeros(3,n);
65 for j = 1:n
66     Tau(:,j) = D(j+tc-1).Ti*[fx(j); fy(j); 1];
67
68 end
69
70
71
72 Tau(1,:) = Tau(1,)/(5.8*(1/.87));
73 Tau(2,:) = Tau(2,)/(5.8);
74 xlswrite('tauoflags',Tau(1:2,:))
75
76 figure
77 plot([0:n-1],Tau(1,:),[0:n-1],Tau(2,:))
78 hold on
79 plot([0,n-1],[T1m/5.8,T1m/5.8],'-r')
80 plot([0,n-1],[-T1m/5.8,-T1m/5.8],'-r')
81
82 t = toc
83
84 profile off
85

```

```

1 close all
2 clear all
3 clc
4
5
6 Ds = {'Dvectorworkspace'};
7
8 for n = 1:length(Ds);
9 load(Ds{n});
10
11 qsteps = length(D);
12
13 Tkm = 23.2*5.8;
14 Tsm = 23.2;
15 mu = 0.9;
16
17 fx = linspace(-1250, 1250, 500);
18 fy = linspace(0, 2500, 500);
19 P = zeros(length(fx), length(fy));
20 Q = P;
21
22 for i = 1:qsteps
23     Tk_max = Tkm-abs(D(i).tau_ki);
24     Ts_max = Tsm-abs(D(i).tau_si);
25
26     for j = 1:length(fx)
27         for k = 1:length(fy)
28             T = D(i).Ti*[fx(j);fy(k);1];
29
30             if abs(T(1)) <= Tk_max && abs(T(2)) <= Ts_max
31
32                 if fy(k) > D(i).F_f(2) && abs((fx(j)-D(i).F_f(1))/(fy(k)-D(i).F_f(2))) ...
33                     <= mu
34                     P(j,k) = 1;
35                     Q(j,k) = Q(j,k)+1;
36                 end
37             end
38         end
39     end
40 end
41
42
43
44

```

```

45 figure
46 contourf(fx,fy,Q',1,'-k','LevelListMode','manual','LevelList',1)
47 colormap([1,1,1;.8,.8,.8]);
48 set(gca,'FontSize',10,'FontName','Times')
49 set(gcf,'PaperUnits','inches')
50 set(gcf,'PaperPosition',[0,0,2.6,2.4])
51 set(gcf,'Position',[500,500,2.6*100,2.4*100])
52 grid on
53 xlabel('x direction body force, F_{bx} (N)')
54 ylabel('y direction body force, F_{by} (N)')
55
56 figure
57 contour(fx,fy,Q',10,'LevelListMode','manual','LevelList',linspace(1,400,10));
58 set(gca,'FontSize',10,'FontName','Times')
59 set(gcf,'PaperUnits','inches')
60 set(gcf,'PaperPosition',[0,0,2.6,2.4])
61 set(gcf,'Position',[500,500,2.6*100,2.4*100])
62 grid on
63 xlabel('x direction body force, F_{bx} (N)')
64 ylabel('y direction body force, F_{by} (N)')
65
66
67
68
69
70
71
72 end

```

Bibliography

- [1] R. M. Alexander. The gaits of bipedal and quadrupedal animals. *The International Journal of Robotics Research*, 3(2):49–59, 1984.
- [2] K. Aminian, B. Najafi, C. Büla, P.F. Leyvraz, and P. Robert. Spatio-temporal parameters of gait measured by an ambulatory system using miniature gyroscopes. *Journal of Biomechanics*, 35(5):689–699, 2002.
- [3] K. Autumn, Y. A. Liang, S. T. Hsieh, W. Zesch, W. P. Chan, T. W. Kenny, R. Fearing, and R. J. Full. Adhesive force of a single gecko foot-hair. *Nature*, 405(6787):681–684, 2000.
- [4] J. E. Bertram and A. Gutmann. Motions of the running horse and cheetah revisited: fundamental mechanics of the transverse and rotary gallop. *Journal of The Royal Society Interface*, 6(35):549–559, October 2008.
- [5] A. A. Biewener. Biomechanics of mammalian terrestrial locomotion. *Science*, 250(4984):1097, 1990.
- [6] A. A. Biewener. *Animal Locomotion*. Oxford University Press, New York, January 2003.
- [7] E. L. Brancato. Estimation of lifetime expectancies of motors. *Electrical Insulation Magazine, IEEE*, 8(3):5–13, 1992.
- [8] G. Caurin and N. Tschichold-Gurman. The development of a robot terrain interaction system for walking machines. *Robotics and Automation, 1994. Proceedings., 1994 IEEE International Conference on*, pages 1013–1018 vol. 2, 1994.
- [9] J. Charteris, D. Leach, and C. Taves. Comparative kinematic analysis of bipedal and quadrupedal locomotion: a cyclographic technique. *Journal of Anatomy*, 128(Pt 4):803, 1979.
- [10] K. J. Chi and V. Louise Roth. Scaling and mechanics of carnivoran footpads reveal the principles of footpad design. *Journal of The Royal Society Interface*, 7(49):1145–1155, June 2010.
- [11] Cosworth. Traction Circles. *Racecar Engineering*, 21(2):98, February 2011.
- [12] T. M. Dauphinee and H. Preston-Thomas. A Copper Resistance Temperature Scale. *Review of Scientific Instruments*, 25(9):884, 1954.

- [13] M. Ehsani, Y. Gao, and J. M. Miller. Hybrid electric vehicles: Architecture and motor drives. *Proceedings of the IEEE*, 95(4):719–728, 2007.
- [14] M. S. Erden. Optimal Protraction of a Biologically Inspired Robot Leg. *Journal of Intelligent & Robotic Systems*, 64(3-4):301–322, February 2011.
- [15] E. C. Frederick. Physiological and ergonomics factors in running shoe design. *Applied Ergonomics*, 15(4):281–287, 1984.
- [16] M. Gienger, F. Pfeiffer, and H. Cruse. Entwurf und Realisierung einer zweibeinigen Laufmaschine. In *Autonomes Laufen*, page 295. VDI-Verlag, Düsseldorf, March 2005.
- [17] T. Hemker, M. Stelzer, O. von Stryk, and H. Sakamoto. Efficient Walking Speed Optimization of a Humanoid Robot. *The International Journal of Robotics Research*, 28(2):303–314, February 2009.
- [18] M. Hildebrand. Motions of the running cheetah and horse. *Journal of Mammalogy*, 40(4):481–495, 1959.
- [19] N. Hogan. Impedance Control: An Approach to Manipulation. In *American Control Conference, 1984*, pages 304–313, 1984.
- [20] N. Hogan. Impedance control: an approach to manipulation: part I-theory, Part II-implementation, Part III-Application. *Journal of Dynamic Systems, Measurement and Control*, 107(1):1–24, 1985.
- [21] N. Hogan. Stable execution of contact tasks using impedance control. *Robotics and Automation. Proceedings. 1987 IEEE International Conference on*, 4:1047–1054, 1987.
- [22] P. E. Hudson, S. A. Corr, R. C. Payne-Davis, S. N. Clancy, E. Lane, and A. M. Wilson. Functional anatomy of the cheetah (*Acinonyx jubatus*) forelimb. *Journal of Anatomy*, 218(4):375–385, February 2011.
- [23] I. W. Hunter, J. M. Hollerbach, and J. Ballantyne. A comparative analysis of actuator technologies for robotics. *Robotics Review*, 2, 1991.
- [24] S. H. Hyon. Compliant terrain adaptation for biped humanoids without measuring ground surface and contact forces. *Robotics, IEEE Transactions on*, 25(1):171–178, 2009.
- [25] R. K. Josephson. Contraction dynamics and power output of skeletal muscle. *Annual review of physiology*, 55(1):527–546, 1993.
- [26] K. Kaneko, K. Harada, F. Kanehiro, G. Miyamori, and K. Akachi. Humanoid robot HRP-3. In *Intelligent Robots and Systems, 2008. IROS 2008. IEEE/RSJ International Conference on*, pages 2471–2478, 2008.
- [27] J. G. Karssen, M. Haberland, M. Wisse, and S. Kim. The optimal swing-leg retraction rate for running. *Robotics and Automation (ICRA), 2011 IEEE International Conference on*, pages 4000–4006, 2011.

- [28] K. C. Kim, K. Kim, H. J. Kim, and J. Lee. Demagnetization analysis of permanent magnets according to rotor types of interior permanent magnet synchronous motor. *IEEE Transactions on Magnetics*, 45(6):2799–2802, 2009.
- [29] H. Knuesel, H. Geyer, and A. Seyfarth. Influence of swing leg movement on running stability. *Human Movement Science*, 24(4):532–543, August 2005.
- [30] F. Lacquaniti, M. Le Taillanter, L. Lopiano, and C. Maioli. The control of limb geometry in cat posture. *The Journal of Physiology*, 426(1):177, 1990.
- [31] D. A. Lawrence. Actuator limitations on achievable manipulator impedance. In *Robotics and Automation, 1989. Proceedings., 1989 IEEE International Conference on*, pages 560–565, 1989.
- [32] D. V. Lee and S. G. Meek. Directionally compliant legs influence the intrinsic pitch behaviour of a trotting quadruped. *Proceedings of the Royal Society B: Biological Sciences*, 272(1563):567–572, March 2005.
- [33] W. Lee. *Designing articulated legs for running machines*. PhD thesis, Massachusetts Institute of Technology, 1990.
- [34] W. Letko. Preliminary Wind-Tunnel Investigation at Low Speed of Stability and Control Characteristics of Swept-Back Wings. Technical report, 1946.
- [35] S. Lohmeier, T. Buschmann, H. Ulbrich, and F. Pfeiffer. Modular joint design for performance enhanced humanoid robot LOLA. *Robotics and Automation, 2006. ICRA 2006. Proceedings 2006 IEEE International Conference on*, pages 88–93, 2006.
- [36] B. G. Lovegrove. Locomotor Mode, Maximum Running Speed, and Basal Metabolic Rate in Placental Mammals. *Physiological and Biochemical Zoology*, 77(6):916–928, November 2004.
- [37] R. Lydekker and P. L. Sclater. *The Royal Natural History*, volume 1. F. Warne, London, January 1893.
- [38] W. A. Mair and D. L. Birdsall. *Aircraft Performance*. Cambridge Aerospace Series. Cambridge University Press, March 1996.
- [39] P. E. Martin and R. C. Nelson. The effect of carried loads on the walking patterns of men and women. *Ergonomics*, 29(10):1191–1202, October 1986.
- [40] J. M. R. Martinez and J. Duffy. An application of screw algebra to the acceleration analysis of serial chains. *Mechanism and machine theory*, 31(4):445–457, 1996.
- [41] T. McGeer. Dynamics and control of bipedal locomotion. *J. theor. Biol.*, 163:277–314, 1993.
- [42] T. A. McMahon, G. Valiant, and E. C. Frederick. Groucho running. *Journal of Applied Physiology*, 62(6):2326–2337, 1987.

- [43] W. F. Milliken and D. L. Milliken. *Race Car Vehicle Dynamics*. Society of Automotive Engineers, January 1997.
- [44] T. F. Novacheck. The biomechanics of running. *Gait & posture*, 7(1):77–95, 1998.
- [45] G.J. O’Hara. Mechanical impedance and mobility concepts. *The Journal of the Acoustical Society of America*, 41:1180, 1967.
- [46] E. Papadopoulos and S. Dubowsky. On the nature of control algorithms for free-floating space manipulators. *Robotics and Automation, IEEE Transactions on*, 7(6):750–758, 1991.
- [47] J.J. Perrine and V. R. Edgerton. Muscle force-velocity and power-velocity relationships under isokinetic loading. *Medicine and science in sports*, 10(3):159, 1978.
- [48] S. J. Piazza. The Sprinter’s Foot. *Mechanical Engineering Magazine*, (October), October 2009.
- [49] I. Poulakakis, J. A. Smith, and M. Buehler. On the dynamics of bounding and extensions towards the half-bound and the gallop gaits. *Proc. of the 2nd Int. Symp. on Adaptive Motion of Animals and Machines*, 2003.
- [50] M. H. Raibert, K. Blankespoor, G. Nelson, and R. Playter. BigDog, the Rough-Terrain Quadruped Robot. *Proceedings of the 17th World Congress*, pages 10823–10825, 2008.
- [51] M. H. Raibert, H. B. Brown Jr, M. Chepponis, J. Koechling, J. K. Hodgins, D. Dustman, W. K. Brennan, D. S. Barrett, C. M. Thompson, and J. D. Hebert. Dynamically Stable Legged Locomotion (September 1985-Septembers1989). Technical report, Massachusetts Institute of Technology, 1989.
- [52] R. Rajamani. *Vehicle Dynamics and Control*. Mechanical Engineering Series. Springer, 1 edition, October 2005.
- [53] J. P. Schmie德勒, R. Siston, and K. Waldron. The significance of leg mass in modeling quadrupedal running gaits. *COURSES AND LECTURES-INTERNATIONAL CENTRE FOR MECHANICAL SCIENCES*, pages 481–488, 2002.
- [54] J. P. Schmie德勒 and K. J. Waldron. The mechanics of quadrupedal galloping and the future of legged vehicles. *The International Journal of Robotics Research*, 18(12):1224–1234, 1999.
- [55] N. C. C. Sharp. Timed running speed of a cheetah (*Acinonyx jubatus*). *Journal of Zoology*, 241(3):493–494, 1997.
- [56] R. Siegwart, P. Lamon, T. Estier, M. Lauria, and R. Piguet. Innovative design for wheeled locomotion in rough terrain. *Robotics and Autonomous systems*, 40(2):151–162, 2002.

- [57] J. L. Smith, S. H. Chung, and R. F. Zernicke. Gait-related motor patterns and hindlimb kinetics for the cat trot and gallop. *Experimental brain research*, 94(2):308–322, 1993.
- [58] A. Staniforth. *Competition Car Suspension: A Practical Handbook*. Haynes Publishing, 4 edition, October 2006.
- [59] S. Stramigioli and H. Bruyninckx. Geometry and screw theory for robotics. *Tutorial during ICRA*, 2001, 2001.
- [60] Z. Vafa and S. Dubowsky. On the dynamics of manipulators in space using the virtual manipulator approach. *Robotics and Automation. Proceedings. 1987 IEEE International Conference on*, 4:579–585, 1987.
- [61] B. Venkataraman, B. Godsey, W. Premerlani, E. Shulman, M. Thaku, and R. Midence. Fundamentals of a motor thermal model and its applications in motor protection. *Protective Relay Engineers, 2005 58th Annual Conference for*, pages 127–144, 2005.
- [62] R. M. Walter and D. R. Carrier. Ground forces applied by galloping dogs. *Journal of Experimental Biology*, 210(2):208–216, January 2007.
- [63] G. H. Wentink. Dynamics of the hind limb at walk in horse and dog. *Anatomy and embryology*, 155(2):179–190, 1979.
- [64] B. Wilcox, A. Nasif, and R. Welch. Implications of martian rock distributions on rover scaling. *Planetary Society International Conference on Mobile Planetary Robots and Rover Roundup, Santa Monica CA*, 1997.
- [65] S. B. Williams, A. M. Wilson, L. Rhodes, J. Andrews, and R. C. Payne. Functional anatomy and muscle moment arms of the pelvic limb of an elite sprinting athlete: the racing greyhound (*Canis familiaris*). *Journal of Anatomy*, 213(4):361–372, October 2008.
- [66] T. M. Williams, G. P. Dobson, O. Mathieu-Costello, D. Morsbach, M. B. Worley, and J. A. Phillips. Skeletal muscle histology and biochemistry of an elite sprinter, the African cheetah. *Journal of Comparative Physiology B: Biochemical, Systemic, and Environmental Physiology*, 167(8):527–535, 1997.
- [67] H. Witte, R. Hackert, K. E. Lilje, N. Schilling, D. Voges, G. Klauer, W. Ilg, J. Albiez, A. Seyfarth, and D. Germann. Transfer of biological principles into the construction of quadruped walking machines. *Robot Motion and Control, 2001 Proceedings of the Second International Workshop on*, pages 245–249, 2001.
- [68] T. S. Zhao and J. S. Dai. Dynamics and coupling actuation of elastic underactuated manipulators. *Journal of Robotic Systems*, 20(3):135–146, 2003.